ETH zürich

ETH Library

Multiple Metasomatism beneath the Nógrád–Gömör Volcanic Field (Northern Pannonian Basin) Revealed by Upper Mantle Peridotite Xenoliths

Journal Article

Author(s):
Liptai, Nóra; Patkó, Levente; Kovács, István; Hidas, Károly; Pintér, Zsanett; Jeffries, Teresa; Zajacz, Zoltán; O'Reilly, Suzanne Y.; Griffin, William L.; Pearson, Norman J.; Szabó, Csaba

Publication date:
2017-06

Permanent link:
https://doi.org/10.3929/ethz-b-000220122

Rights / license:
In Copyright - Non-Commercial Use Permitted

Originally published in:
Journal of Petrology 58(6), https://doi.org/10.1093/petrology/egx048

This page was generated automatically upon download from the ETH Zurich Research Collection.
For more information, please consult the Terms of use.

JOURNAL OF PETROLOGY

Journal of Petrology, 2017, Vol. 58, No. 6, 1107–1144
doi: 10.1093/petrology/egx048
Advance Access Publication Date: 21 July 2017
Original Article

OXFORD

Multiple Metasomatism beneath the Nógrád–Gömör Volcanic Field (Northern Pannonian Basin) Revealed by Upper Mantle Peridotite Xenoliths

Nóra Liptai[1,2], Levente Patkó[1], István J. Kovács[3]*, Károly Hidas[4], Zsanett Pintér[1†], Teresa Jeffries[5‡], Zoltán Zajacz[6§], Suzanne Y. O'Reilly[2], William L. Griffin[2], Norman J. Pearson[2] and Csaba Szabó[1¶]

[1]Lithosphere Fluid Research Lab, Institute of Geography and Earth Sciences, Eötvös University, Budapest, H-1117, Hungary; [2]Australian Research Council Centre of Excellence for Core to Crust Fluid Systems (CCFS) and GEMOC, Department of Earth and Planetary Sciences, Macquarie University, North Ryde, NSW 2109, Australia; [3]Hungarian Geological and Geophysical Institute, Budapest, H-1143, Hungary; [4]Instituto Andaluz de Ciencias de la Tierra, CSIC & UGR, Avenida de las Palmeras 4, E-18100 Armilla (Granada), Spain; [5]Department of Earth Science, The Natural History Museum, London SW7 5BD, UK; [6]Department of Earth Sciences, Institute of Isotope Geochemistry and Mineral Resources, ETH Zürich, 8092 Zürich, Switzerland

[¶]Corresponding author. E-mail: cszabo@elte.hu
*Present address: Geodetic and Geophysical Institute, MTA Research Centre for Astronomy and Earth Sciences, Sopron, H-9400, Hungary.
[†]Present address: Australian Research Council Centre of Excellence for Core to Crust Fluid Systems (CCFS) and GEMOC, Department of Earth and Planetary Sciences, Macquarie University, North Ryde, NSW 2109, Australia.
[‡]Deceased.
[§]Present address: Department of Earth Sciences, University of Toronto, Toronto, ON, M5S 3B1, Canada.

Received December 11, 2014; Accepted July 19, 2017

ABSTRACT

Peridotite xenoliths from the Nógrád–Gömör Volcanic Field (NGVF) record the geochemical evolution of the subcontinental lithospheric mantle beneath the northern margin of the Pannonian Basin. This study is focused on spinel lherzolites and presents petrography, and major and trace element geochemistry for 51 xenoliths selected from all xenolith-bearing localities of the NGVF. The xenoliths consist of olivine, orthopyroxene, clinopyroxene and spinel ± amphibole. No correlations between modal composition and textures were recognized; however, major and trace element geochemistry reveals several processes, which allow the distinction of xenolith groups with different geochemical evolution. The xenoliths have undergone varying degrees (~7–25%) of partial melting with overprinting by different metasomatic processes. Based on their Mg#, the xenoliths can be subdivided into two major groups. Group I has olivine Mg# between 89 and 91, whereas Group II has Mg# <89, significant enrichment of Fe and Mn in olivine and pyroxenes, and high Ti in spinel. Trace element contents of the xenoliths vary widely, allowing a further division based on light rare earth element (LREE) enrichment or depletion in pyroxenes. REE patterns of amphiboles match those of clinopyroxenes in each xenolith where they appear, and are inferred to have different origins based on their Nb (and other high field strength element) contents. It is proposed that Nb-poor amphiboles record the oldest metasomatic event, caused by subduction-related volatile-bearing silicate melts or fluids, followed by at least two further metasomatic processes: one that resulted in U–Th–(Nb–Ta)–LREE enrichment and crystallization of Nb-rich amphibole, affecting

© The Author 2017. Published by Oxford University Press. All rights reserved. For Permissions, please e-mail: journals.permissions@oup.com

Downloaded from https://academic.oup.com/petrology/article/58/6/1107/4001466 by ETH Zurich user on 30 June 2022

selective domains under the entire NGVF, and another evidenced by Fe–Mn–Ti–LREE enrichment, which overprinted early geochemical signatures. We suggest that the metasomatic agents in both cases were basaltic silicate melts, compositionally similar to the host basalts. These melts were generated during the Miocene extension of the Pannonian Basin. The effects of heating and subsequent cooling are evident in significantly different equilibration temperatures.

Key words: lithospheric mantle evolution; mantle metasomatism; Pannonian Basin; mantle xenoliths

INTRODUCTION

Mantle xenoliths from the Carpathian–Pannonian region (CPR) have been extensively studied, especially those from the Bakony–Balaton Highland (e.g. Embey-Isztin *et al.*, 1989, 2001, 2014; Downes *et al.*, 1992; Szabó *et al.*, 1995, 2004; Bali *et al.*, 2002, 2007, 2008; Falus *et al.*, 2004; Hidas *et al.*, 2007, 2010; Dobosi *et al.*, 2010; Berkesi *et al.*, 2012; Kovács *et al.*, 2012). These data provide a detailed picture of the petrographic and geochemical features in the mantle beneath the central part of the CPR, which has been used to discuss mantle dynamics and processes in the ALCAPA microplate (Fig. 1a). Data on the geochemical composition, together with partial constraints on the evolution of the lithospheric mantle, are also available for xenoliths from the Styrian Basin (Vaselli *et al.*, 1996; Coltorti *et al.*, 2007*b*), Little Hungarian Plain (Falus *et al.*, 2007) and Perşani Mountains (Vaselli *et al.*, 1995; Falus *et al.*, 2008, 2011).

The Nógrád–Gömör Volcanic Field (NGVF), located on the northern margin of the Pannonian Basin, is the least studied of the five regions in the CPR where mantle xenoliths are hosted by Plio-Pleistocene alkali basalts. The most abundant xenoliths in the NGVF are spinel peridotites with dominantly lherzolitic composition, which have previously been the subject of petrographic and geochemical studies (Embey-Isztin, 1978; Szabó & Taylor, 1994; Konečný *et al.*, 1995, 1999), but these studies do not cover all the xenolith locations. Furthermore, trace element compositions have been published only for bulk-rock analyses (Szabó & Taylor, 1994); this study presents the first comprehensive data on individual mineral phases. Our major goals are to provide a detailed database and a comparison of all NGVF localities, and to characterize the geochemical characteristics and processes in the evolution of the lithospheric mantle under the NGVF.

GEOLOGICAL BACKGROUND

The Pannonian Basin is located in Eastern Central Europe, surrounded by the Alps, the Carpathians and the Dinarides. It consists of two microplates: ALCAPA (NW) and Tisza–Dacia (SE), separated by the Middle Hungarian Zone (Csontos, 1995). The two microplates were juxtaposed during the late Oligocene–early Miocene, following the extrusion of ALCAPA from the Alpine collision zone (Kázmér & Kovács, 1985). From the middle to late Miocene, extension occurred in the basin in two phases. In the active extensional phase (17–14 Ma), rollback of a subducting plate at the eastern margin of the Pannonian Basin caused intense thinning of the lithosphere by thermal erosion (Stegena *et al.*, 1975) and the uplift of the underlying asthenosphere (Horváth, 1993; Csontos, 1995). The phase of passive extension (11·5–8 Ma) was accompanied by gravitational instability of the lithosphere, further thinning it, especially in the middle of the basin (Horváth, 1993; Lenkey, 1999).

Beginning in the Miocene, eruptions of rhyolitic, intermediate calc-alkaline, alkali basaltic and ultrapotassic magmas took place throughout the CPR (Szabó *et al.*, 1992; Harangi & Lenkey, 2007; Kovács & Szabó, 2008; Seghedi & Downes, 2011). The alkali basalts erupted mostly in the Pliocene and Pleistocene (Szabó *et al.*, 1992; Embey-Isztin *et al.*, 1993; Harangi, 2001), with ages ranging from 11 Ma in the western regions of the Pannonian Basin to a few hundred thousand years in the eastern margin and Central Slovakia (Pécskay *et al.*, 1995, 2006). The origin of the basaltic melts can be correlated with a decrease in pressure resulting from asthenospheric uplift (e.g. Embey-Isztin *et al.*, 1993). The five major areas where upper mantle xenoliths occur in alkali basalts are, from west to east: Styrian Basin, Little Hungarian Plain, Bakony–Balaton Highland, Nógrád–Gömör and Perşani Mountains (Fig. 1a).

The alkali basalts in the NGVF are dominantly effusive rocks and pyroclastic deposits, containing upper mantle xenoliths only to the west of Fil'akovo, from Podrečany in the NW to Bárna in the SE (Fig. 1b). The part of the volcanic field where xenoliths occur can be divided into three spatially and temporally distinct domains, namely the northern, central and southern parts. Isolated volcanic cones are characteristic in the northern and southern parts, whereas the central part consists of two basalt plateaux (Babi Hill and Medves Plateau) and one monogenetic volcano (Fil'akovo-Kerčik; Fig. 1b). Eruption ages in these domains decrease from north to south: K–Ar ages of volcanic eruptions are 6·4–4·9 Ma in the northern part, 4·0–2·5 Ma in the central part and ~2·5 Ma in the southern part (Balogh *et al.*, 1981). The monogenetic volcano of Fil'akovo-Kerčik is older (4·0 Ma) than the two basalt plateaux forming the central part (3·0–2·5 Ma; K. Balogh, unpublished data). U/Pb and (U–Th)/He dating yielded similar ages for the northern and central part (7·0–5·9 and 3·0–1·7 Ma, respectively; Hurai *et al.*, 2013).

Downloaded from https://academic.oup.com/petrology/article/58/6/1107/4001466 by ETH Zurich user on 30 June 2022

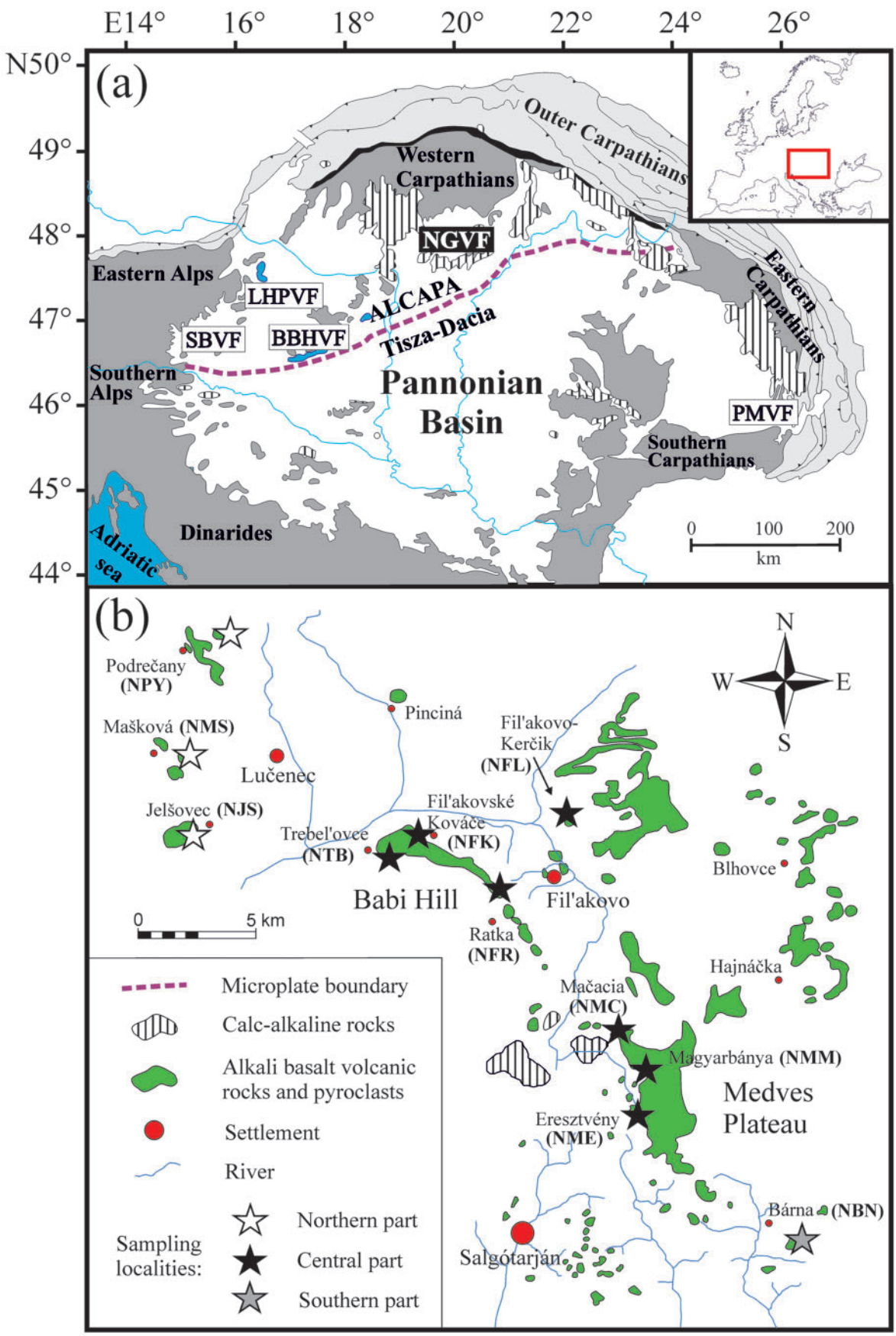

Fig. 1. (a) Localities of xenolith-hosting alkali basalts in the Carpathian–Pannonian region (after Szabó *et al.*, 1992; Harangi, 2001). SBVF, Styrian Basin Volcanic Field; LHPVF, Little Hungarian Plain Volcanic Field; BBHVF, Bakony–Balaton Highland Volcanic Field; NGVF, Nógrád–Gömör Volcanic Field; PMVF, Perşani Mountains Volcanic Field. (b) Alkali basalt occurrences and sampling locations in the Nógrád–Gömör Volcanic Field; quarries or outcrops from NW to SE are Podrečany (NPY), Mašková (NMS), Jelšovec (NJS), Trebel'ovce (NTB), Fil'akovské Kováče (NFK), Ratka (NFR), Mačacia (NMC), Magyarbánya (NMM), Eresztvény (NME) and Bárna-Nagykő (NBN).

Downloaded from https://academic.oup.com/petrology/article/58/6/1107/4001466 by ETH Zurich user on 30 June 2022

Several types of xenoliths have been reported from the NGVF: spinel peridotites rich in olivine and containing Cr-diopside veins (Szabó & Taylor, 1994), which are also the focus of this study; clinopyroxene-rich xenoliths enriched in Al, Na, Ti and Ca interpreted as cumulates formed at the mantle–crust boundary (Kovács *et al.*, 2004; Zajacz *et al.*, 2007) and lower crustal granulite xenoliths (Kovács & Szabó, 2005). Mineral major element data and constraints on P–T–fO_2 conditions, derived from the peridotite xenoliths of several locations in the NGVF, were reported by Konečný *et al.* (1995, 1999) and Szabó & Taylor (1994). The latter study also provided bulk-rock major and trace element data for the NGVF peridotites, concluding that these xenoliths were depleted in 'basaltic' major elements and enriched in light rare earth elements (LREE) to some extent; the metasomatic agent was considered to be a slab-derived melt. Kovács & Szabó (2008) later suggested that the subduction that produced the metasomatizing melt could also have occurred before the ALCAPA microplate was extruded from the Alpine region to the Pannonian Basin during the Miocene.

SAMPLING AND APPLIED TECHNIQUES

From over 200 collected samples, 51 xenoliths with dominantly lherzolitic composition were chosen for studies of their petrography and mineral chemistry. They were collected from 11 quarries and outcrops—three in the northern (Podrečany, Mašková and Jelšovec) seven in the central (Fil'akovo-Kerčik, Trebel'ovce, Fil'akovské Kováče, Ratka, Mačacia, Magyarbánya, Eresztvény), and one in the southern part (Bárna-Nagykő) of the NGVF (Fig. 1b). The xenoliths occur in lavas at all localities, except for Jelšovec where they are hosted in pyroclastic deposits. Given the small size of the NGVF xenoliths (maximum 4 cm in diameter), the most important factors for selection were size and freshness (i.e. the least possible alteration by either surface processes or reaction with the host basalt), so that the xenoliths represent a composition closest to the state of the upper mantle at the time of eruption. At least three xenoliths were selected from each sampling location for adequate representation.

Petrographic examination of ~150–300 μm thick polished sections was carried out with a polarized light microscope in the Lithosphere Fluid Research Lab (Eötvös University, Budapest, Hungary). Thin-section photomicrographs were taken with a Nikon DS-Fi1 digital camera attached to the microscope using NIS Elements AR 2.20 digital imaging software. Modal compositions of the xenoliths were determined by point counting on thin section images digitized at 1200 d.p.i. resolution with an HP Scanjet 2400 scanner, using the open source software JMicroVision developed by Nicolas Roduit.

For measuring major elements in the minerals we used a CAMECA SX-50 microprobe equipped with a wavelength-dispersive spectrometer at the University of Padova (Italy), and a CAMECA SX-100 microprobe equipped with an energy-dispersive spectrometer and five wavelength-dispersive spectrometers at Macquarie University (Sydney, Australia). The accelerating voltage was 20 keV and the beam current was 20 nA for all analyses.

Trace element contents of ortho- and clinopyroxene in xenoliths from the northern and central part of the NGVF were determined at the Natural History Museum (London, UK) and at Macquarie University (Sydney, Australia). At the Natural History Museum an Agilent 7500 s quadrupole inductively coupled plasma mass spectrometry (ICP-MS) system equipped with an ESI New Wave Research UP193FX laser ablation system was used. The laser beam had a wavelength of 193 nm, 3 J cm^{-2} energy density at a frequency of 10 Hz and a spot size of 45 μm. The NIST-612 synthetic glass was used as an external standard with the average composition determined by Pearce *et al.* (1997); for the internal standard we used ^{43}Ca. Evaluation of the resulting data was carried out with LAMTRACE software. At Macquarie University, an Agilent 7700 x quadrupole ICP-MS system was used, and the laser ablation was carried out with a Photon Machines 193 nm Excimer laser system, with a frequency of 5 Hz, energy density of 9·28 J cm^{-2}, and 50 μm spot size. We used the NIST 610 synthetic glass as external standard and CaO previously determined by electron microprobe as the internal standard. The resulting data were evaluated using the GLITTER software package (Griffin *et al.*, 2008). Xenoliths from the southern part were analyzed at the Institute of Isotope Geochemistry and Mineral Resources, ETH-Zürich (Zürich, Switzerland), using a coupled ELAN 6100 DRC quadrupole mass spectrometer equipped with an ArF excimer UV laser source. The wavelength of the laser beam was 193 nm, energy density was 52 mJ cm^{-2} at a frequency of 10 Hz, and the spot size was between 40 and 60 μm. For the external standard the NIST SRM 610 synthetic glass was used; data processing was carried out with the use of SILLS software (Guillong *et al.*, 2008).

PETROGRAPHY

The selected spinel peridotites have modal composition ranging from harzburgite to wehrlite based on the classification of Streckeisen (1976) (Table 1; Fig. 2). Some of the samples correspond to the modal composition of the average European subcontinental lithospheric mantle (SCLM) published by Downes (1997). However, many xenoliths are characterized by higher modal abundances of clinopyroxene (and olivine), representing a modally modified upper mantle domain.

Classification of xenolith textures follows Mercier & Nicolas (1975). The samples show three textural types: protogranular (Fig. 3a), which more accurately corresponds to the coarse granular type described by Lenoir *et al.* (2000), porphyroclastic (Fig. 3b), and equigranular (Fig. 3c). There is a distinct geographical clustering of

Downloaded from https://academic.oup.com/petrology/article/58/6/1107/4001466 by ETH Zurich user on 30 June 2022

Table 1: Petrographic properties and calculated equilibration temperatures of the studied xenoliths

Sample	Rock	Texture	Modal composition (%)					opx/cpx	Melt	Group	Equilibration temperature (°C)			
	name		ol	opx	cpx	sp	amp		pockets* (%)		TT98	TBK90	TNG10	TREE
Northern part														
NMS1302A	lhz	prot	89	5	5	1		1·0	—	Group IB	851	863	928	1021 ± 41
NMS1304	lhz	prot	80	12	6	1	1	2·0	—	Group IB	829	845	921	1030 ± 29
NMS1305	lhz	prot	62	25	9	4		2·8	—	Group IB	870	918	942	1044 ± 50
NMS1308	lhz	porph	69	20	9	2	0·1	2·2	—	Group IA	861	926	930	980 ± 9
NMS1310	lhz	porph	43	46	11	0·1		4·2	—	Group IA	884	953	974	1027 ± 1
NJS1302	lhz	porph	73	14	11	2	0·1	1·3	—	Group IIA	864	962	961	1063 ± 38
NJS1304	lhz	prot	80	12	5	3		2·4	—	Group IIA	855	944	961	1052 ± 23
NJS1306	lhz	prot	66	13	17	4		0·8	<5	Group IIA	977	1025	1043	1145 ± 2
NJS1307	lhz	prot	69	17	12	2		1·4	—	Group IA	947	1024	1006	1097 ± 18
NPY1301	lhz	prot	79	13	6	2		2·2	—	Group IA	867	941	952	999 ± 17
NPY1310	lhz	prot	68	11	18	3		0·6	—	Group IIA	893	936	967	1070 ± 15
NPY1311	lhz	porph	60	19	19	2		1·0	—	Group IIA	900	944	970	1052 ± 23
NPY1314	lhz	porph	51	28	18	3		1·6	—	Group IA	861	928	958	1040 ± 15
Central part														
NFL1302	lhz	porph	77	10	8	5	0·1	1·3	—	Group IB	885	926	967	1031 ± 4
NFL1305	lhz	porph	58	29	12	1		2·4	<5	Group IB	904	940	971	1070 ± 56
NFL1315A	hzb	equi	89	8	2	1	0·1	4·0	—	Group IB	862	901	969	991 ± 42
NFL1316	lhz	porph	82	10	5	3		2·0	—	Group IB	860	892	959	965 ± 10
NFL1324	lhz	porph	52	40	5	1·5	1·5	8·0	—	Group IB	896	938	991	1030 ± 39
NFL1326	wht	porph	85		12	1	2	—	—	Group IIB	n.a.	n.a.	n.a.	n.a.
NFL1327	wht	porph	88	1	10	1		0·1	—	Group IIB	925	952	1019	1112 ± 21
NFL1329	lhz	porph	76	11·5	11·5	1	0·1	1·0	—	Group IA	889	932	965	1013 ± 10
NTB0306	lhz	porph	79	12	10	0·1		1·2	—	Group IB	947	994	951	901 ± 1
NTB0307	lhz	porph	79	6	15	0·1		0·4	<5	Group IA	1012	1058	943	991 ± 4
NTB1124	lhz	porph	62	24	12	2		2·0	—	Group IA	938	993	1001	1031 ± 22
NTB1116	lhz	porph	67	21	10	2		2·1	—	Group IA	908	970	980	1015 ± 3
NTB1122	lhz	porph	64	19	15	2		1·3	—	Group IIB	942	999	1044	1154 ± 32
NFK0301	lhz	porph	78	16	6	0·1		2·9	<5	Group IB	949	996	984	1045 ± 21
NFK1123	lhz	porph	61	33	5	1		6·6	—	Group IB	941	985	983	1022 ± 23
NFK1108	lhz	porph	87	6	6	1		1·0	—	Group IIB	950	996	1044	1141 ± 23
NFK1115	lhz	equi	87	8	4	1		2·0	—	Group IIB	874	913	972	1028 ± 26
NFR0306	wht	porph	88	1	9	2		0·1	—	Group IIB	922	966	1031	1080 ± 17
NFR0307	lhz	porph	79	8	10	3		0·8	—	Group IIB	842	869	972	962 ± 17
NFR1109	lhz	porph	77	17	5	0·5		3·4	—	Group IIB	972	1010	1022	1056 ± 26
NFR0309	lhz	porph	67	19	12	2		1·6	—	Group IB	883	955	977	1047 ± 25
NFR1107	lhz	porph	74	18	7	1		2·6	—	Group IB	894	952	985	1021 ± 15
NMC1301	lhz	porph	82	11	5	2		2·2	—	Group IB	912	958	1000	1066 ± 24
NMC1309	lhz	porph	78	6	14	2		0·4	—	Group IIB	910	942	990	1068 ± 15
NMC1322	lhz	porph	77	12	8	3		1·5	5–10	Group IB	895	944	969	988 ± 38
NMC1336A	lhz	porph	68	21	8	3		2·6	<5	Group IA	894	961	980	1037 ± 17
NMM1126	lhz	porph	59	30	10	1		3·0	—	Group IA	933	974	983	990 ± 19
NMM0318	lhz	porph	65	20	13	2		1·5	—	Group IIB	913	951	983	1071 ± 31
NMM1115	lhz	equi	82	10	6	2		1·7	—	Group IB	865	912	957	997 ± 19
NME1122	lhz	porph	78	11	11	0·5		1·0	—	Group IB	916	968	968	958 ± 5
NME0528	lhz	porph	82	11	6	1		1·8	—	Group IB	898	947	984	1059 ± 25
NME1116	lhz	porph	65	21	11	3		1·9	<5	Group IA	892	947	984	1027 ± 41
Southern part														
NBN0302A	lhz	porph	83	11	5	0·5		2·0	<5	Group IA	867	902	932	1011 ± 4
NBN0305	lhz	equi	79	15	6	0		2·4	—	Group IB	893	912	933	1028 ± 59
NBN0311	lhz	porph	81	7	10	1		0·7	<5	Group IA	858	917	922	965 ± 28
NBN0316	lhz	equi	79	11	9	1		1·3	5–10	Group IA	898	912	941	1122 ± 50
NBN0319	lhz	equi	70	16	13	1		1·3	>10	Group IA	886	888	941	1114 ± 51
NBN0321	lhz	porph	76	13	10	1		1·3	<5	Group IA	869	924	946	930 ± 8

Rock type and texture abbreviations: lhz, lherzolite; hzb, harzburgite; wht, wehrlite; prot, protogranular; porph, porphyroclastic; equi, equigranular. Equilibration temperatures were calculated using thermometers as follows: TT98, two-pyroxene method of Taylor (1998); TBK90, two-pyroxene method of Brey & Köhler (1990); TNG10, Ca-in-opx method of Brey & Köhler (1990) modified by Nimis & Grütter (2010); TREE, REE method of Liang *et al.* (2013). n.a., not applicable owing to lack of orthopyroxene analyses.
*Not included in modal compositions.

textural types: xenoliths from the northern part of the NGVF have protogranular and porphyroclastic textures, porphyroclastic textures predominate in samples of the central part, and the southern part is composed of porphyroclastic and equigranular xenoliths in approximately equal proportions (Table 1).

Olivine forms 43–89 vol. % of the studied xenoliths, a slightly wider range than the modal composition data

Downloaded from https://academic.oup.com/petrology/article/58/6/1107/4001466 by ETH Zurich user on 30 June 2022

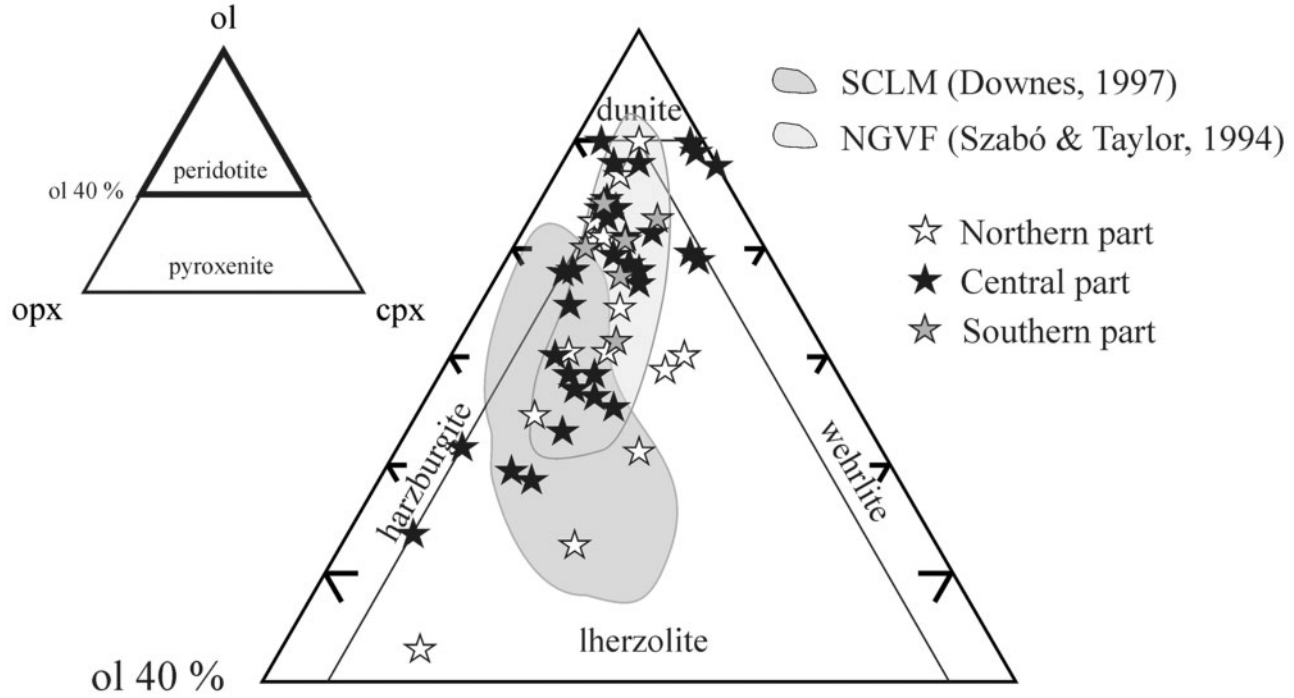

Fig. 2. Modal composition of the studied NGVF xenoliths on a Streckeisen (1976) diagram, along with xenolith data from a previous study of the area (Szabó & Taylor, 1994) and the average composition of the subcontinental lithospheric mantle (SCLM; Downes, 1997). ol, olivine; opx, orthopyroxene; cpx, clinopyroxene.

published by Szabó & Taylor (1994); however, many of the xenoliths have unusually high (~80 vol. % and above) modal proportions of olivine (Fig. 2). Olivine grains are generally isometric and their size ranges from 0·1 to 1·5 mm across; some porphyroclasts reach 2–3 mm in diameter. Rarely, olivine grains are elongated up to aspect ratios of 2:1 and define a lineation, particularly in xenoliths from the southern part. Olivine grain boundaries are dominantly curvilinear (Fig. 3a and b), except in equigranular xenoliths where they are straight (Fig. 3c). Undulose extinction occurs in olivine from all studied xenoliths. In some cases, olivine contains euhedral or anhedral inclusions of spinel, providing evidence of grain growth (Mercier & Nicolas, 1975). However, olivine can also be included in orthopyroxene, which has been described in numerous studies as having a poikilitic character (e.g. Frey & Prinz, 1978; Downes *et al.*, 1992).

Orthopyroxene represents 1–46 vol. % of the studied xenoliths (10–25% for the majority of samples; Table 1), and is completely absent in one xenolith (NFL1326). Orthopyroxene grain sizes are similar to those of olivine, except for the porphyroclasts, which are usually larger (up to 5–6 mm). Orthopyroxene porphyroclasts are commonly surrounded by dynamically recrystallized neoblasts. The porphyroclasts have curvilinear grain boundaries and rarely contain clinopyroxene exsolution lamellae (Fig. 3d) and inclusions of spinel and/or olivine. Orthopyroxene neoblasts are isometric, usually between 0·1 and 0·8 mm, and have straight grain boundaries in contrast to the porphyroclasts.

Clinopyroxene grains are smaller (50 μm to 1 mm) than orthopyroxene grains, form 2–19 vol. %, and only rarely appear as porphyroclasts. In xenolith NBN032A a clinopyroxene porphyroclast contains exsolution lamellae of spinel. The opx/cpx ratio varies between 0·1 and 4·0 (Table 1), with two exceptional values of 6·6 (NFK1123) and 8·0 (NFL1324) owing to the presence of large orthopyroxene porphyroclasts in the sample. Some of the opx/cpx ratios fall below 1·5, which is unusual for 'normal' lherzolitic mantle composition (Downes, 1997). Xenoliths with lower ratios (i.e. clinopyroxene enrichment compared with orthopyroxene; Fig. 3e), are within the group that differs from the average SCLM composition, and are generally accompanied by higher proportions of olivine (Fig. 2).

Spinels are mostly interstitial and have slightly elongated shapes (Fig. 3f), and can sometimes be enclosed in the silicate phases. They show the lowest abundance, about 0·1–3 vol. %. In some cases a lineation defined by elongated spinels can be observed (Fig. 3f), matching the stretching lineation outlined by olivine where present.

Amphibole is present in xenoliths from two locations in the northern part (Mašková and Jelšovec), and the isolated volcano from the central part (Fil'akovo Kerčik). In Jelšovec, only one xenolith contains amphibole, in the form of two very small (0·1–0·2 mm) grains.

Downloaded from https://academic.oup.com/petrology/article/58/6/1107/4001466 by ETH Zurich user on 30 June 2022

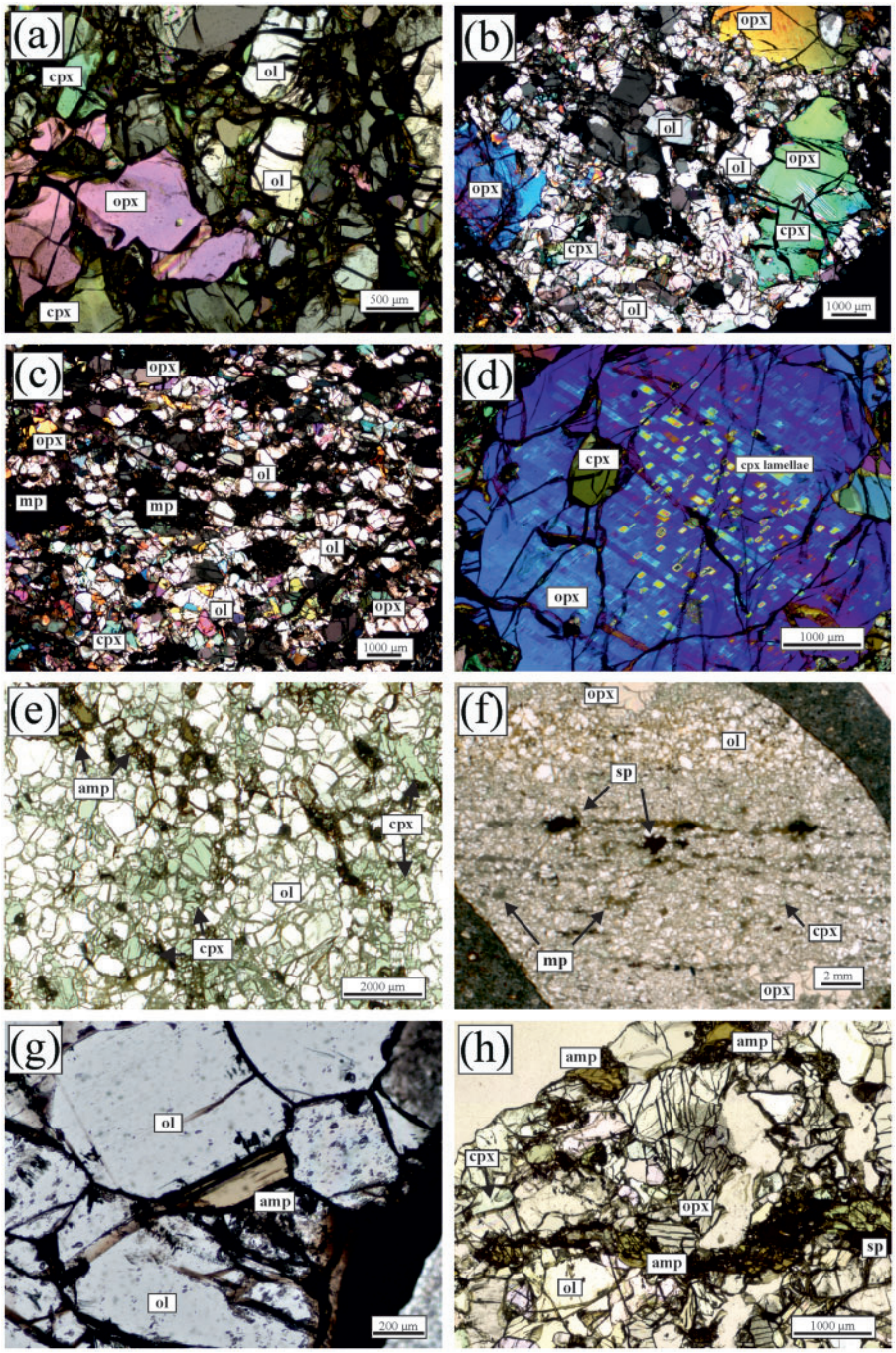

Fig. 3. Photomicrographs of upper mantle xenoliths showing different textural types and characteristics from the Nógrád–Gömör Volcanic Field. (a) Protogranular texture in xenolith NJS1307 (transmitted light, cross-polarized). (b) Porphyroclastic texture in xenolith NFK1123 (transmitted light, cross-polarized); with clinopyroxene exsolution lamellae in the orthopyroxene porphyroclasts. (c) Equigranular texture in xenolith NBN0319 with melt pockets (transmitted light, cross-polarized). (d) Clinopyroxene exsolution lamellae and poikilitic clinopyroxene in an orthopyroxene porphyroclast in xenolith NFL1324 (transmitted light, cross-polarized). (e) Wehrlite xenolith with disseminated amphiboles in sample NFL1326 (transmitted light, plane-polarized). (f) Scanned image of NBN032A lherzolite with visible lineation outlined by spinels and melt pockets. (g) Interstitial amphibole in xenolith NFL1315A (transmitted light, plane-polarized). (h) Amphibole in a vein in xenolith NFL1324 (transmitted light, plane-polarized). N, nicol (prism in the microscope); ol, olivine; opx, orthopyroxene; cpx, clinopyroxene; sp, spinel; amp, amphibole; mp, melt pocket.

Amphibole grains in the rest of the xenoliths are also sparse (maximum 2%; Table 1), interstitial (Fig. 3g) or form veins (Fig. 3h). There is no modal amphibole in the studied xenoliths from the other localities of the central and southern parts; however, Szabó & Taylor (1994) described samples from the southern part with a significant modal amphibole content (2–4%).

Some xenoliths, especially from the southern part, contain melt pockets with an average size of 0·5–1·5 mm (Table 1); they consist of glass and a secondary

Downloaded from https://academic.oup.com/petrology/article/58/6/1107/4001466 by ETH Zurich user on 30 June 2022

Table 2: Major element mineral composition of the studied xenoliths (in wt %)

Sample	Group	Olivine									
		n	SiO_2	Al_2O_3	FeO	MnO	MgO	CaO	NiO	Total	Mg#
NMS1302A	Group IB	22	41·6	n.d.	8·47	0·13	50·1	0·05	0·40	100·70	0·91
NMS1304	Group IB	14	41·2	0·03	9·42	0·13	48·7	0·05	0·40	99·84	0·90
NMS1305	Group IB	19	41·1	0·03	10·4	0·14	48·5	0·06	0·41	100·64	0·89
NMS1308	Group IA	16	41·1	n.d.	9·60	0·14	48·8	0·05	0·41	100·13	0·90
NMS1310	Group IA	11	40·9	0·04	9·83	0·14	49·3	0·06	0·40	100·58	0·90
NJS1302	Group IIA	13	40·7	0·03	11·6	0·15	47·3	0·06	0·38	100·19	0·88
NJS1304	Group IIA	14	40·8	0·03	11·7	0·16	47·7	0·06	0·39	100·84	0·88
NJS1306	Group IIA	14	40·7	0·04	12·0	0·18	47·2	0·10	0·39	100·60	0·88
NJS1307	Group IA	12	41·0	0·03	10·4	0·15	48·5	0·09	0·40	100·62	0·89
NPY1301	Group IA	13	41·1	0·03	10·4	0·15	48·5	0·06	0·39	100·59	0·89
NPY1310	Group IIA	8	40·8	0·03	11·1	0·15	47·1	0·07	0·38	99·66	0·88
NPY1311	Group IIA	9	40·9	0·02	11·0	0·16	47·3	0·06	0·36	99·80	0·88
NPY1314	Group IA	8	40·9	0·01	10·2	0·15	48·1	0·06	0·39	99·84	0·89
NFL1302	Group IB	14	40·9	0·12	9·41	0·14	49·1	0·06	0·41	100·07	0·90
NFL1305	Group IB	7	40·9	0·02	9·28	0·14	49·0	0·07	0·40	99·83	0·90
NFL1315A	Group IB	7	41·0	0·01	10·1	0·15	48·7	0·06	0·36	100·39	0·90
NFL1316	Group IB	8	41·4	0·04	9·13	0·13	49·5	0·07	0·40	100·70	0·91
NFL1324	Group IB	7	41·1	0·01	8·66	0·12	49·8	0·07	0·41	100·22	0·91
NFL1326	Group IIB	7	40·3	0·02	14·3	0·26	45·1	0·11	0·27	100·30	0·85
NFL1327	Group IIB	9	40·1	0·03	14·2	0·25	45·8	0·08	0·33	100·83	0·85
NFL1329	Group IA	7	40·9	0·01	9·89	0·14	48·9	0·07	0·41	100·36	0·90
NTB0306	Group IB	29	40·4	n.d.	9·46	0·16	50·4	0·07	0·39	100·91	0·90
NTB0307	Group IA	10	41·8	0·03	9·11	0·13	49·3	0·11	0·41	100·92	0·91
NTB1124	Group IA	6	40·8	0·00	9·07	0·14	50·5	0·07	0·40	100·94	0·91
NTB1116	Group IA	12	41·2	0·03	9·21	0·13	49·1	0·08	0·39	100·20	0·90
NTB1122	Group IIB	12	40·8	0·04	11·6	0·18	47·1	0·10	0·34	100·25	0·88
NFK0301	Group IB	32	40·6	0·02	9·75	0·16	49·3	0·07	0·40	100·32	0·90
NFK1123	Group IB	5	40·9	0·01	8·73	0·13	50·2	0·08	0·38	100·51	0·91
NFK1108	Group IIB	12	41·2	0·03	10·8	0·17	47·7	0·13	0·34	100·36	0·89
NFK1115	Group IIB	15	40·8	n.d.	10·9	0·20	47·4	0·06	0·39	99·83	0·89
NFR0306	Group IIB	11	39·8	0·02	13·8	0·25	45·8	0·13	0·33	100·15	0·86
NFR0307	Group IIB	9	39·9	0·03	12·1	0·24	47·0	0·14	0·33	99·78	0·87
NFR1109	Group IIB	9	40·2	0·01	14·4	0·25	45·8	0·08	0·32	101·08	0·85
NFR0309	Group IB	11	41·1	0·03	10·0	0·14	48·3	0·07	0·39	100·01	0·90
NFR1107	Group IB	12	41·3	0·03	8·85	0·14	49·3	0·07	0·40	100·08	0·91
NMC1301	Group IB	11	41·2	n.d.	9·63	0·13	49·0	0·06	0·42	100·51	0·90
NMC1309	Group IIB	9	40·9	0·03	11·4	0·18	47·8	0·06	0·40	100·76	0·88
NMC1322	Group IB	12	41·2	0·03	9·49	0·13	49·4	0·07	0·41	100·72	0·90
NMC1336A	Group IA	10	41·2	0·03	9·25	0·13	49·3	0·07	0·42	100·43	0·90
NMM1126	Group IA	6	40·7	0·01	9·41	0·15	50·2	0·08	0·42	100·98	0·90
NMM0318	Group IIB	12	41·2	0·04	11·0	0·17	47·2	0·07	0·37	100·14	0·88
NMM1115	Group IB	14	41·3	0·03	9·07	0·13	49·2	0·08	0·41	100·18	0·91
NME1122	Group IB	7	40·5	0·01	9·47	0·13	50·2	0·07	0·36	100·75	0·90
NME0528	Group IB	13	41·2	0·03	9·50	0·14	48·7	0·06	0·39	100·12	0·90
NME1116	Group IA	12	41·4	0·04	9·17	0·13	49·2	0·07	0·41	100·41	0·91
NBN0302A	Group IA	9	40·1	0·01	9·96	0·14	50·3	0·08	0·38	100·99	0·90
NBN0305	Group IB	11	40·4	n.d.	9·45	0·14	50·1	0·08	0·38	100·60	0·90
NBN0311	Group IA	6	39·8	n.d.	9·78	0·15	50·2	0·12	0·35	100·42	0·90
NBN0316	Group IA	6	40·5	n.d.	10·2	0·15	49·6	0·05	0·42	100·96	0·90
NBN0319	Group IA	13	40·5	n.d.	10·2	0·16	49·5	0·05	0·36	100·79	0·90
NBN0321	Group IA	9	40·2	n.d.	9·83	0·14	49·9	0·10	0·38	100·58	0·90

(continued)

generation of spinel and clinopyroxene; they are aligned subparallel to the lineation (where observable), similar to the spinels (Fig. 3f).

MINERAL MAJOR ELEMENT GEOCHEMISTRY

Mg-numbers of olivine [Mg/(Mg + Fe)] are between 0·85 and 0·91 (Table 2), and the majority of the xenoliths have high Mg# (0·90–0·91). However, several samples from the northern and central part show significantly lower values between 0·85 and 0·88 (Fig. 4a), and six of them plot outside the olivine–spinel mantle array (OSMA; Arai, 1994). Manganese contents in olivine show a negative correlation with Mg# (Fig. 4b), reaching the highest values (0·23–0·26 wt %) in the xenoliths with the lowest Mg# (Table 2). However, the values show little variation within xenoliths with the 'normal' Mg# range (0·89–0·91).

Orthopyroxenes have CaO contents between 0·63 and 0·98 wt % and Al_2O_3 between 1·86 and 5·00 wt %. The lowest orthopyroxene Al_2O_3 contents occur in xenoliths NMS1302A, NFL1315A, NFL1316, NTB0306,

Downloaded from https://academic.oup.com/petrology/article/58/6/1107/4001466 by ETH Zurich user on 30 June 2022

Table 2: Continued

Sample	Group	Orthopyroxene										
		n	SiO_2	TiO_2	Al_2O_3	Cr_2O_3	FeO	MnO	MgO	CaO	Na_2O	Total	Mg#
NMS1302A	Group IB	28	57·1	0·03	2·18	0·48	5·43	0·13	34·7	0·65	0·04	100·78	0·92
NMS1304	Group IB	12	56·1	0·07	2·96	0·42	6·00	0·15	33·5	0·63	0·05	99·99	0·90
NMS1305	Group IB	16	55·5	0·05	4·27	0·33	6·61	0·15	32·9	0·69	0·08	100·67	0·90
NMS1308	Group IA	10	55·8	0·08	3·65	0·49	6·07	0·14	33·2	0·65	0·07	100·24	0·91
NMS1310	Group IA	14	55·4	0·10	4·19	0·45	6·25	0·14	33·3	0·77	0·10	100·82	0·92
NJS1302	Group IIA	14	54·8	0·20	4·41	0·36	7·34	0·15	32·0	0·73	0·11	100·19	0·89
NJS1304	Group IIA	29	55·4	0·18	4·14	0·35	7·36	0·15	32·3	0·73	0·12	100·84	0·89
NJS1306	Group IIA	12	54·5	0·12	4·93	0·35	7·69	0·17	31·5	0·98	0·12	100·43	0·89
NJS1307	Group IA	14	55·0	0·16	5·00	0·36	6·56	0·15	32·4	0·86	0·14	100·64	0·90
NPY1301	Group IA	10	55·3	0·13	4·49	0·36	6·57	0·15	32·7	0·71	0·11	100·59	0·90
NPY1310	Group IIA	11	55·0	0·12	4·85	0·22	6·98	0·16	31·7	0·74	0·09	99·95	0·88
NPY1311	Group IIA	8	54·4	0·13	4·92	0·23	6·93	0·16	31·7	0·75	0·09	99·41	0·89
NPY1314	Group IA	7	54·9	0·09	4·44	0·31	6·63	0·14	32·7	0·72	0·06	100·12	0·91
NFL1302	Group IB	11	55·4	0·07	4·07	0·43	6·03	0·14	33·2	0·75	0·07	100·24	0·91
NFL1305	Group IB	7	55·2	0·03	4·05	0·48	5·99	0·14	33·1	0·76	0·06	99·95	0·91
NFL1315A	Group IB	9	56·3	0·06	1·97	0·50	6·38	0·17	33·8	0·75	0·07	99·99	0·91
NFL1316	Group IB	10	56·7	0·05	2·50	0·55	5·85	0·14	34·1	0·73	0·05	100·72	0·91
NFL1324	Group IB	8	55·6	0·05	3·39	0·67	5·61	0·15	33·6	0·82	0·07	100·07	0·92
NFL1327	Group IIB	11	55·3	0·05	2·94	0·51	8·94	0·25	31·7	0·90	0·07	100·75	0·88
NFL1329	Group IA	12	55·5	0·06	4·23	0·36	6·30	0·15	33·0	0·74	0·07	100·48	0·91
NTB0306	Group IB	10	56·0	0·05	2·07	0·52	6·02	0·18	34·5	0·70	n.d.	100·05	0·91
NTB0307	Group IA	2	56·5	0·04	3·82	0·39	5·93	0·09	33·2	0·69	n.d.	100·67	0·91
NTB1124	Group IA	7	54·8	0·16	4·13	0·53	5·79	0·14	33·7	0·85	0·07	100·20	0·91
NTB1116	Group IA	14	55·5	0·08	4·09	0·53	5·92	0·13	33·0	0·79	0·14	100·34	0·91
NTB1122	Group IIB	11	54·7	0·25	4·69	0·48	7·44	0·18	31·6	0·98	0·08	100·41	0·88
NFK0301	Group IB	28	55·4	0·06	3·72	0·59	6·26	0·14	33·1	0·79	n.d.	100·07	0·90
NFK1123	Group IB	8	55·6	0·08	3·37	0·58	5·70	0·13	34·0	0·80	0·08	100·34	0·91
NFK1108	Group IIB	13	55·6	0·10	3·49	0·50	6·88	0·16	32·4	0·98	0·08	100·27	0·89
NFK1115	Group IIB	15	56·6	0·03	1·86	0·45	6·92	0·20	33·1	0·76	0·06	100·08	0·89
NFR0306	Group IIB	3	54·6	0·08	2·88	0·48	8·80	0·24	31·4	0·92	n.d.	99·40	0·86
NFR0307	Group IIB	2	55·0	0·01	3·01	0·39	7·70	0·21	32·4	0·75	n.d.	99·48	0·88
NFR1109	Group IIB	8	55·9	0·07	1·95	0·51	9·00	0·27	32·0	0·91	0·08	100·72	0·86
NFR0309	Group IB	16	55·1	0·14	4·59	0·32	6·43	0·15	32·5	0·78	0·09	100·22	0·90
NFR1107	Group IB	14	56·1	0·08	3·26	0·54	5·70	0·13	33·5	0·80	0·08	100·27	0·91
NMC1301	Group IB	11	56·4	0·04	2·87	0·62	6·14	0·15	33·6	0·85	0·08	100·87	0·91
NMC1309	Group IIB	8	55·3	0·05	4·01	0·47	7·23	0·18	32·3	0·81	0·08	100·57	0·89
NMC1322	Group IB	11	55·8	0·04	3·91	0·51	6·09	0·14	33·4	0·76	0·09	100·91	0·91
NMC1336A	Group IA	10	55·5	0·11	3·84	0·53	5·94	0·13	33·3	0·79	0·09	100·34	0·91
NMM1126	Group IA	6	55·1	0·06	4·08	0·47	6·02	0·13	33·6	0·79	0·09	100·29	0·91
NMM0318	Group IIB	14	55·2	0·08	4·45	0·35	7·03	0·17	31·9	0·79	0·07	100·22	0·88
NMM1115	Group IB	15	55·9	0·08	3·54	0·49	5·81	0·14	33·4	0·72	0·06	100·24	0·91
NME1122	Group IB	8	55·2	0·09	3·70	0·49	6·08	0·15	33·9	0·75	0·07	100·40	0·91
NME0528	Group IB	11	56·2	0·07	3·02	0·57	6·12	0·15	33·3	0·80	0·07	100·37	0·90
NME1116	Group IA	14	55·7	0·07	3·99	0·48	5·86	0·14	33·2	0·80	0·09	100·44	0·91
NBN0302A	Group IA	10	54·8	0·07	3·44	0·37	6·39	0·15	34·3	0·66	0·04	100·24	0·90
NBN0305	Group IB	13	55·3	0·07	3·16	0·43	6·16	0·14	34·2	0·66	0·03	100·09	0·91
NBN0311	Group IA	2	54·1	0·07	3·90	0·42	6·34	0·14	34·1	0·63	0·08	99·76	0·90
NBN0316	Group IA	7	54·7	0·07	3·92	0·30	6·75	0·14	33·7	0·68	0·01	100·27	0·90
NBN0319	Group IA	13	54·8	0·06	3·88	0·29	6·65	0·16	33·5	0·68	0·01	100·00	0·90
NBN0321	Group IA	9	54·6	0·09	3·52	0·41	6·31	0·13	34·0	0·69	0·04	99·85	0·91

(continued)

NFK1115 and NFR1109, which are the samples with the highest spinel Cr# (Fig. 4a). Mg-numbers of orthopyroxene (0·86–0·91) correlate well with those of olivine, as well as MnO contents, which show elevated values (0·21–0·27) in the three NFR samples mentioned above (Table 2). Concentrations of Al_2O_3 generally correlate well with Mg# (Fig. 4c), except for those xenoliths with low Mg#, which lie off the trend.

Clinopyroxene Al_2O_3 contents range from 2·57 to 7·64 wt %, whereas Na_2O contents range between 0·37 and 2·06 wt %. Xenoliths from the northern part tend to have higher concentrations of Na and Al than those from the central and southern parts (Table 2). These elements show a good positive correlation in most of the samples; however, one group of xenoliths defines a different trend, with decreasing Al content, with Na varying only in a narrow range (Fig. 4d). These xenoliths (NMS1302A, NFL1315A, NFL1316, NTB0306, NFK1115, and NFR1109) overlap with the ones exhibiting the highest spinel Cr# (Fig. 4a, Table 2). Equigranular xenoliths from the southern part characteristically have lower values of both elements compared with the porphyroclastic ones from the southern part (Table 2). Mg-numbers of clinopyroxene vary

Downloaded from https://academic.oup.com/petrology/article/58/6/1107/4001466 by ETH Zurich user on 30 June 2022

Table 2: Continued

Sample	Group	Clinopyroxene										
		n	SiO_2	TiO_2	Al_2O_3	Cr_2O_3	FeO	MnO	MgO	CaO	Na_2O	Total	Mg#
NMS1302A	Group IB	8	54·0	0·05	2·57	0·96	2·13	0·08	17·4	23·2	0·55	100·96	0·94
NMS1304	Group IB	15	52·5	0·24	3·77	0·93	2·43	0·08	16·5	22·8	0·66	99·89	0·92
NMS1305	Group IB	20	52·2	0·27	6·59	0·77	2·80	0·09	15·3	21·2	1·47	100·75	0·91
NMS1308	Group IA	13	51·6	0·41	6·08	1·28	2·52	0·09	15·3	20·9	1·50	99·71	0·91
NMS1310	Group IA	15	51·8	0·49	6·61	1·10	2·74	0·09	15·4	20·5	1·74	100·48	0·91
NJS1302	Group IIA	11	50·8	1·16	7·64	0·93	3·10	0·08	14·3	19·8	1·95	99·84	0·89
NJS1304	Group IIA	9	51·8	0·96	7·15	0·87	3·10	0·09	14·7	20·0	2·06	100·75	0·89
NJS1306	Group IIA	14	51·2	0·51	7·13	0·72	3·86	0·11	15·3	20·0	1·49	100·31	0·88
NJS1307	Group IA	12	51·6	0·71	7·59	0·76	3·09	0·10	15·1	19·7	1·88	100·49	0·90
NPY1301	Group IA	12	52·0	0·58	7·16	0·84	2·83	0·09	14·8	20·3	1·94	100·63	0·90
NPY1310	Group IIA	9	51·7	0·56	6·86	0·43	3·08	0·10	15·1	21·1	1·38	100·23	0·90
NPY1311	Group IIA	14	51·5	0·56	7·02	0·45	3·07	0·10	15·0	21·0	1·38	100·13	0·90
NPY1314	Group IA	6	50·6	0·59	7·25	0·74	2·95	0·09	14·9	20·8	1·47	99·34	0·90
NFL1302	Group IB	13	51·7	0·32	5·74	0·91	2·65	0·08	15·8	21·5	1·19	99·91	0·91
NFL1305	Group IB	9	51·8	0·15	5·63	0·96	2·71	0·08	15·8	21·2	1·23	99·63	0·91
NFL1315A	Group IB	9	52·7	0·15	3·12	1·39	2·71	0·09	16·6	21·5	1·14	99·53	0·92
NFL1316	Group IB	10	53·4	0·14	3·46	1·11	2·47	0·08	16·7	22·1	1·06	100·47	0·92
NFL1324	Group IB	11	52·1	0·20	4·70	1·37	2·55	0·09	16·2	21·3	1·21	99·85	0·92
NFL1326	Group IIB	10	51·4	0·38	4·92	0·93	4·15	0·12	14·9	22·0	1·17	100·02	0·86
NFL1327	Group IIB	12	52·2	0·20	4·49	1·13	4·24	0·14	15·8	21·0	1·20	100·39	0·87
NFL1329	Group IA	7	52·0	0·32	6·16	0·69	2·77	0·09	15·7	21·3	1·32	100·32	0·91
NTB0306	Group IB	9	53·1	0·11	3·32	1·25	2·65	0·09	16·7	20·8	1·18	99·19	0·92
NTB0307	Group IA	5	53·3	0·21	5·53	0·79	2·78	0·06	16·1	20·6	1·12	100·50	0·91
NTB1124	Group IA	7	51·2	0·53	5·74	1·05	2·83	0·08	16·1	21·0	1·13	99·65	0·91
NTB1116	Group IA	11	52·2	0·34	6·02	1·17	2·74	0·08	15·5	20·6	1·59	100·21	0·91
NTB1122	Group IIB	13	50·7	0·97	6·48	0·89	3·61	0·11	15·4	20·9	1·07	100·14	0·88
NFK0301	Group IB	11	52·2	0·25	5·15	1·20	2·83	0·05	15·9	20·6	1·31	99·50	0·91
NFK1123	Group IB	7	52·2	0·29	4·61	1·26	2·59	0·08	16·4	21·2	1·07	99·70	0·92
NFK1108	Group IIB	14	52·1	0·39	5·08	1·12	3·31	0·11	16·0	21·0	1·07	100·23	0·90
NFK1115	Group IIB	9	53·3	0·05	3·01	1·30	3·01	0·11	16·4	21·5	1·14	99·92	0·91
NFR0306	Group IIB	10	51·3	0·30	4·86	1·08	4·11	0·11	15·5	20·4	1·29	99·02	0·87
NFR0307	Group IIB	5	51·2	0·40	3·93	0·94	3·44	0·08	16·0	22·0	0·78	98·88	0·89
NFR1109	Group IIB	11	53·2	0·19	3·39	1·36	4·18	0·15	16·1	20·2	1·31	99·98	0·87
NFR0309	Group IB	15	51·3	0·64	7·11	0·74	2·87	0·09	15·0	20·6	1·57	100·01	0·90
NFR1107	Group IB	12	52·3	0·31	4·86	1·31	2·58	0·08	16·1	21·1	1·29	99·98	0·92
NMC1301	Group IB	12	53·0	0·11	4·14	1·41	2·80	0·08	16·4	21·2	1·26	100·36	0·91
NMC1309	Group IIB	12	52·2	0·21	5·53	0·96	3·27	0·11	15·7	21·3	1·20	100·51	0·89
NMC1322	Group IB	12	52·5	0·20	5·64	1·10	2·69	0·08	15·8	21·1	1·44	100·54	0·91
NMC1336A	Group IA	13	52·1	0·46	5·88	1·17	2·73	0·08	15·6	20·8	1·50	100·33	0·91
NMM1126	Group IA	6	51·7	0·23	5·57	0·94	2·74	0·08	16·0	21·0	1·22	99·50	0·91
NMM0318	Group IIB	12	52·2	0·34	6·19	0·71	3·09	0·11	15·4	21·2	1·27	100·43	0·90
NMM1115	Group IB	12	52·4	0·30	5·03	1·07	2·47	0·08	15·9	21·6	1·23	100·15	0·92
NME1122	Group IB	9	51·6	0·34	5·39	1·12	2·77	0·09	16·0	20·9	1·28	99·50	0·91
NME0528	Group IB	13	52·8	0·24	4·48	1·35	2·69	0·09	16·1	21·3	1·26	100·26	0·91
NME1116	Group IA	13	52·2	0·28	5·75	1·05	2·65	0·08	15·7	21·0	1·45	100·16	0·91
NBN0302A	Group IA	9	51·3	0·34	4·92	0·81	2·72	0·08	16·4	21·8	0·93	99·29	0·91
NBN0305	Group IB	9	52·0	0·20	3·76	0·91	2·62	0·08	16·9	22·2	0·71	99·31	0·92
NBN0311	Group IA	5	50·8	0·42	6·15	0·77	2·67	0·10	15·8	20·7	1·55	98·87	0·91
NBN0316	Group IA	7	51·2	0·33	4·73	0·50	3·04	0·08	16·7	22·4	0·54	99·57	0·91
NBN0319	Group IA	10	51·4	0·24	4·30	0·44	2·99	0·08	16·9	22·8	0·37	99·51	0·91
NBN0321	Group IA	9	50·9	0·49	5·55	0·88	2·78	0·07	16·0	21·2	1·18	99·13	0·91

(continued)

between 0·86 and 0·94 and correlate well with those of olivine and orthopyroxene.

Spinel Cr# [Cr/(Cr + Al)] shows a wide range, from 0·06 to 0·54. Xenoliths with the highest spinel Cr# (above ~0·3) are the same as those that show an unusual Al–Na trend in clinopyroxene mentioned above, and some of them also have low olivine Mg# (Fig. 4a and b). The Mg and Fe contents of spinel also display a broad range (Table 2), with the highest FeO_{tot} values (20·3–24·3 wt %) in those xenoliths that are also characterized by low Mg# (Table 2). The Al–Cr trend in spinels is also observable in the Al–Cr–Ti × 100 diagram (Fig. 4e), which reveals elevated Ti contents in xenoliths with high FeO contents and low Mg#. Variations between grains within the same xenolith are insignificant compared with differences between the average values of samples (see Supplementary Data Table for analyses of individual grains; supplementary data are available for downloading at http://www.petrology.oxfordjournals.org).

Amphibole is mainly magnesio-hastingsite based on the classification of Locock (2014). The only exception is

Downloaded from https://academic.oup.com/petrology/article/58/6/1107/4001466 by ETH Zurich user on 30 June 2022

Table 2: Continued

Sample	Group	Spinel										
		n	TiO_2	Al_2O_3	Cr_2O_3	FeO	MnO	NiO	MgO	Total	Mg#	Cr#
NMS1302A	Group IB	11	0·06	33·8	36·0	13·0	0·12	0·19	17·2	100·72	0·74	0·42
NMS1304	Group IB	7	0·13	43·4	24·5	12·7	0·11	0·25	18·5	99·89	0·76	0·27
NMS1305	Group IB	15	0·03	56·3	11·2	10·9	0·10	0·39	20·9	99·98	0·81	0·12
NMS1308	Group IA	12	0·08	50·4	17·3	11·3	0·10	0·32	19·8	99·59	0·79	0·19
NMS1310	Group IA	7	0·10	52·7	14·4	11·6	0·10	0·36	20·6	100·09	0·81	0·15
NJS1302	Group IIA	6	0·20	53·8	12·5	12·5	0·09	0·37	19·7	99·38	0·78	0·14
NJS1304	Group IIA	7	0·18	55·1	11·9	12·5	0·10	0·36	20·1	100·39	0·78	0·13
NJS1306	Group IIA	6	0·14	56·4	9·14	14·2	0·12	0·41	19·9	100·44	0·78	0·10
NJS1307	Group IA	9	0·15	58·2	8·80	10·8	0·09	0·39	21·2	99·74	0·82	0·09
NPY1301	Group IA	11	0·10	57·3	9·62	11·5	0·11	0·39	20·5	99·72	0·80	0·10
NPY1310	Group IIA	9	0·09	61·0	5·30	11·3	0·09	0·40	21·4	99·83	0·82	0·06
NPY1311	Group IIA	9	0·09	60·9	5·32	11·3	0·09	0·41	21·4	99·69	0·82	0·06
NPY1314	Group IA	6	0·06	58·0	8·8	11·2	0·09	0·43	21·0	99·79	0·82	0·09
NFL1302	Group IB	11	0·07	53·0	14·3	11·0	0·10	0·36	20·6	99·51	0·81	0·15
NFL1305	Group IB	6	0·04	52·5	15·2	11·3	0·10	0·34	20·3	100·12	0·80	0·16
NFL1315A	Group IB	7	0·27	26·9	40·3	17·4	0·17	0·17	14·9	100·46	0·66	0·50
NFL1316	Group IB	6	0·12	33·3	34·2	14·1	0·13	0·22	16·9	99·35	0·73	0·41
NFL1324	Group IB	7	0·11	40·9	27·0	13·1	0·11	0·26	18·6	100·34	0·77	0·31
NFL1326	Group IIB	6	0·49	34·5	25·5	24·3	0·23	0·22	14·4	100·04	0·62	0·33
NFL1327	Group IIB	5	0·41	33·5	29·0	21·8	0·20	0·23	14·9	100·23	0·64	0·37
NFL1329	Group IA	4	0·05	57·6	10·0	10·7	0·10	0·41	21·0	100·09	0·82	0·10
NTB0306	Group IB	6	0·13	28·0	40·2	16·0	0·30	0·19	16·1	100·75	0·71	0·49
NTB0307	Group IA	5	0·12	53·7	14·4	11·6	n.d.	0·39	20·5	100·72	0·80	0·15
NTB1124	Group IA	6	0·19	49·9	17·6	11·7	0·12	0·33	20·5	100·32	0·81	0·19
NTB1116	Group IA	13	0·10	49·5	18·0	11·5	0·09	0·34	20·2	99·86	0·81	0·20
NTB1122	Group IIB	10	0·39	50·0	15·2	14·3	0·11	0·33	19·1	99·75	0·76	0·17
NFK0301	Group IB	12	0·12	44·3	23·8	14·4	0·55	0·28	18·0	101·45	0·74	0·26
NFK1123	Group IB	6	0·16	43·2	24·3	12·9	0·12	0·34	19·4	100·47	0·79	0·27
NFK1108	Group IIB	4	0·49	42·4	23·8	15·7	0·13	0·27	18·2	101·29	0·74	0·27
NFK1115	Group IIB	9	0·09	24·4	39·1	20·3	0·21	0·18	13·8	98·33	0·64	0·52
NFR0306	Group IIB	6	0·95	32·4	29·0	22·6	n.d.	0·24	13·9	99·01	0·60	0·38
NFR0307	Group IIB	6	0·11	46·1	19·7	15·9	n.d.	0·29	17·1	99·18	0·70	0·22
NFR1109	Group IIB	5	0·44	22·9	39·9	24·0	0·31	0·13	12·2	99·90	0·56	0·54
NFR0309	Group IB	12	0·11	57·6	8·74	11·2	0·09	0·40	21·1	99·36	0·82	0·09
NFR1107	Group IB	8	0·17	41·1	25·4	13·3	0·11	0·26	18·7	99·23	0·78	0·29
NMC1301	Group IB	7	0·11	34·9	32·9	15·0	0·13	0·25	17·1	100·58	0·73	0·39
NMC1309	Group IIB	8	0·07	49·7	16·8	13·7	0·12	0·33	18·8	99·74	0·76	0·18
NMC1322	Group IB	8	0·05	50·8	16·8	11·3	0·11	0·35	20·1	99·76	0·80	0·18
NMC1336A	Group IA	12	0·13	48·5	19·0	12·0	0·10	0·34	19·9	100·26	0·80	0·21
NMM1126	Group IA	6	0·08	51·5	16·2	11·4	0·10	0·37	20·6	100·24	0·82	0·17
NMM0318	Group IIB	12	0·07	56·3	10·9	12·5	0·11	0·36	20·0	100·47	0·78	0·12
NMM1115	Group IB	16	0·12	47·3	20·6	11·9	0·10	0·32	19·6	100·14	0·79	0·23
NME1122	Group IB	7	0·14	47·4	20·0	12·4	0·11	0·32	19·8	100·12	0·80	0·22
NME0528	Group IB	11	0·17	37·9	30·1	14·4	0·12	0·25	17·6	100·79	0·74	0·35
NME1116	Group IA	7	0·09	50·3	17·8	11·9	0·10	0·32	20·1	100·69	0·80	0·19
NBN0302A	Group IA	9	0·12	51·7	15·0	11·6	0·11	0·34	20·7	99·52	0·82	0·16
NBN0305	Group IB	8	0·14	41·6	25·4	13·2	0·14	0·27	18·8	99·62	0·78	0·29
NBN0311	Group IA	2	1·08	39·8	26·7	13·3	0·15	0·21	18·2	99·43	0·75	0·31
NBN0316	Group IA	7	0·15	55·5	11·0	11·6	0·12	0·35	20·5	99·16	0·80	0·12
NBN0319	Group IA	12	0·15	54·5	11·6	12·5	0·11	0·37	20·0	99·14	0·79	0·12
NBN0321	Group IA	10	0·28	51·4	15·4	11·4	0·12	0·36	20·5	99·48	0·81	0·17

Sample	Group	Amphibole														
		n	SiO_2	TiO_2	Al_2O_3	Cr_2O_3	FeO	MnO	MgO	CaO	Na_2O	K_2O	F	Cl	NiO	Total
NMS1304	Group IB	10	41·4	1·38	13·5	1·76	3·54	0·06	17·8	12·1	3·11	1·13	0·06	n.d.	0·13	96·01
NMS1308	Group IA	4	41·2	2·44	14·0	1·68	3·75	0·07	17·7	11·0	3·80	0·37	n.d.	n.d.	0·11	96·08
NJS1302_1	Group IIA	2	39·0	8·09	13·8	0·13	5·20	0·07	16·1	11·1	3·33	n.d.	n.d.	n.d.	n.d.	96·73
NJS1302_2	Group IIA	2	41·3	4·24	13·5	1·21	4·69	0·08	16·7	10·5	3·86	n.d.	n.d.	n.d.	0·12	96·20
NFL1302	Group IB	2	41·6	1·68	14·4	1·38	3·79	0·07	18·0	11·3	3·82	0·48	0·06	0·03	0·16	96·66
NFL1315A	Group IB	7	42·2	2·01	12·2	2·18	4·01	0·06	18·1	11·3	3·19	1·09	0·09	0·04	0·12	96·60
NFL1324	Group IB	9	41·9	1·53	13·5	2·03	3·69	0·05	18·1	11·5	3·16	1·17	0·06	0·05	0·13	96·76
NFL1326	Group IIB	9	40·9	1·74	12·9	1·58	6·13	0·09	16·7	11·5	3·26	0·96	0·20	0·04	0·11	96·22
NFL1329	Group IA	4	41·9	1·69	14·4	1·17	4·04	0·07	17·9	11·2	3·96	0·13	n.d.	n.d.	0·14	96·47

Mg# = Mg/(Mg + Fe); Cr# = Cr/(Cr + Al). *n*, number of analyses; n.d., not detected.

Downloaded from https://academic.oup.com/petrology/article/58/6/1107/4001466 by ETH Zurich user on 30 June 2022

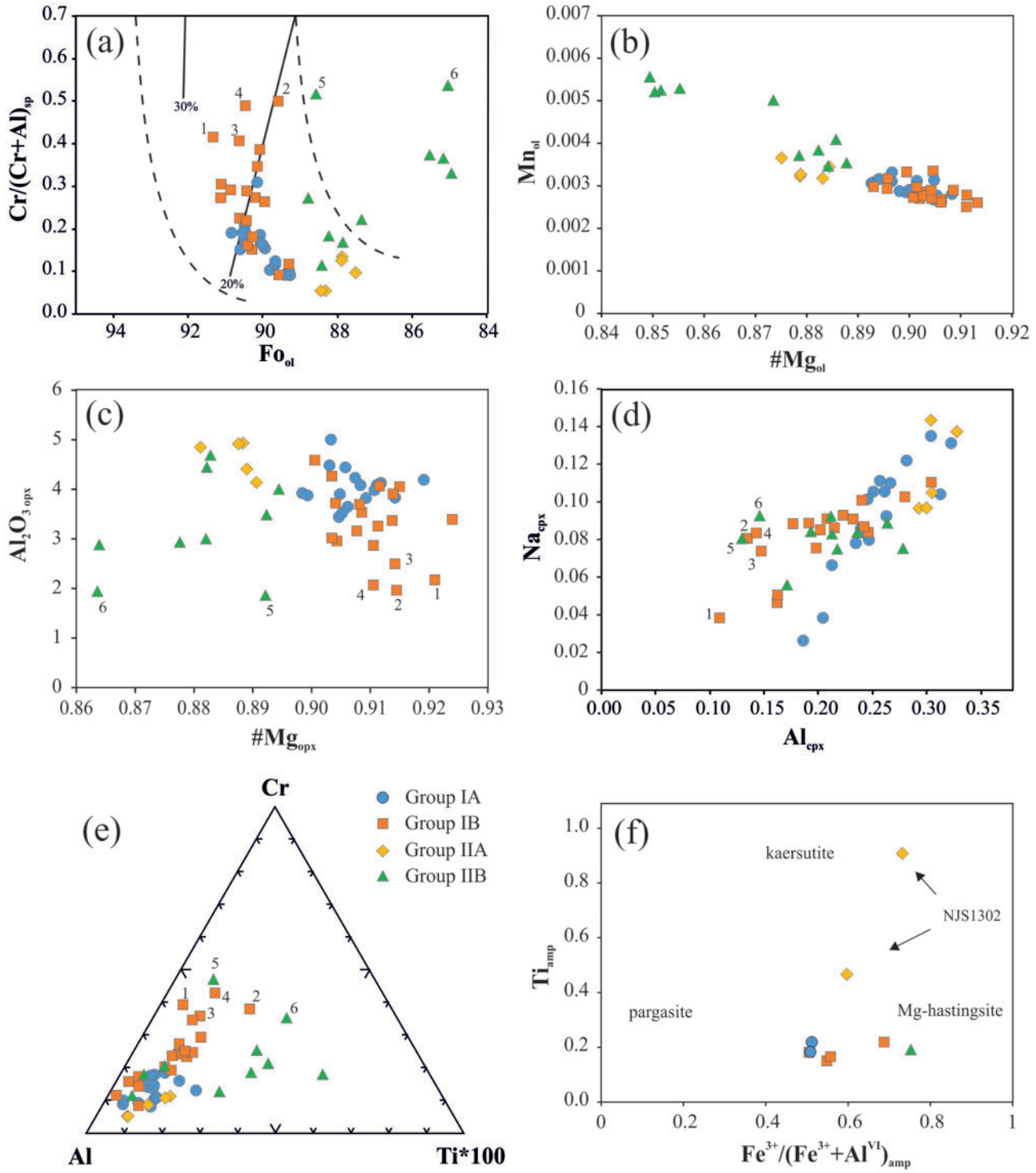

Fig. 4. Major element compositions of minerals in the NGVF xenoliths. (a) OSMA (olivine–spinel mantle array): forsterite contents in olivine vs Cr-number [Cr/(Cr + Al)] of spinel. Average composition of the upper mantle falls between the dashed lines (Arai, 1987); some Group II xenoliths plot outside this field. Continuous lines represent calculated degrees of partial melting (Arai, 1994). (b) Relationship of Mg# vs Mn (cation numbers) in olivine showing a negative correlation. (c) Mg# vs Al_2O_3 in orthopyroxene. (d) Al vs Na cation numbers in clinopyroxene. (e) Al–Cr–Ti × 100 content of spinels; (f) $Fe^{3+}/(Fe^{3+} + Al^{VI})$ vs Ti cation numbers of amphibole for compositional division. Cation numbers were calculated using the spreadsheet of Locock (2014). 'A' and 'B' subgroups of Group I and II have been defined based on clinopyroxene REE contents (for further information, see text section 'Trace element geochemistry of pyroxene and amphibole'). Labelled samples: 1, NMS1302A; 2, NFL1315A; 3, NFL1316; 4, NTB0306; 5, NFK1115; 6, NFR1109

Downloaded from https://academic.oup.com/petrology/article/58/6/1107/4001466 by ETH Zurich user on 30 June 2022

Table 3: Trace element concentrations of pyroxenes and amphibole in the studied xenoliths (in ppm)

Sample	Orthopyroxene															
	n	Rb	Th	U	Ba	Nb	Ta	La	Ce	Pb	Sr	Pr	Nd	Hf	Zr	Sm
Group IA																
NMS1308	6	0·063	n.d.	n.d.	0·235	0·048	0·009	0·009	0·014	0·1	0·21	0·008	0·03	0·039	1·3	n.d
NMS1310	8	0·052	0·007	0·008	n.d.	0·008	0·004	0·006	0·011	n.d.	0·16	0·002	n.d.	0·05	1·47	0·038
NJS1307	8	n.d.	n.d.	0·012	0·007	0·009	0·005	0·01	0·017	0·039	0·28	0·014	0·067	0·08	2·36	0·062
NPY1301	8	0·049	0·006	0·005	0·084	0·009	0·007	0·014	0·018	0·052	0·17	0·007	0·036	0·057	1·54	0·054
NPY1314	7	n.d.	n.d.	0·01	0·012	0·005	0·002	0·007	0·017	n.d.	0·17	0·012	0·042	0·077	1·84	0·051
NFL1329	10	n.d.	0·011	0·007	0·016	0·009	0·001	0·004	0·009	0·035	0·091	0·009	0·037	0·056	1·37	0·011
NTB0307	5	n.d.	0·005	0·003	0·068	0·008	n.d.	n.d.	0·015	n.d.	0·1	0·004	0·045	0·03	0·51	0·031
NTB1124	16	0·085	0·006	0·004	0·039	0·009	0·004	0·003	0·009	0·045	0·1	0·004	0·038	0·043	1·05	0·038
NTB1116	7	0·136	0·006	0·006	0·26	0·011	0·006	0·011	0·015	n.d.	0·32	0·005	0·046	0·042	1·07	0·066
NMC1336A	7	0·063	0·005	0·005	0·336	0·014	0·003	0·006	0·018	0·235	0·13	0·008	0·048	0·055	1·31	0·033
NMM1126	11	0·047	0·005	n.d.	0·05	0·009	0·002	0·005	0·008	n.d.	0·1	0·004	0·02	0·021	0·32	0·027
NME1116	7	n.d.	0·01	0·004	0·158	0·017	0·003	0·013	0·043	0·037	0·27	0·012	0·074	0·044	2·19	0·052
NBN0302A	15	0·024	0·008	n.d.	0·038	0·021	n.d.	0·005	0·018	0·028	0·12	0·01	0·059	0·062	1·44	0·047
NBN0311	15	0·115	0·047	n.d.	0·039	0·027	n.d.	n.d.	0·013	0·022	0·15	0·006	0·041	0·041	1·05	0·053
NBN0316	11	0·316	0·036	n.d.	0·043	0·015	n.d.	0·031	0·019	n.d.	0·12	0·012	0·053	0·075	1·32	0·113
NBN0319	9	0·042	n.d.	n.d.	0·08	0·023	n.d.	n.d.	0·015	n.d.	0·027	0·005	n.d.	0·07	1·39	n.d
NBN0321	14	0·206	0·011	n.d.	0·084	0·019	n.d.	0·006	0·013	0·203	0·087	0·005	0·032	0·052	1·1	0·028
Group IB																
NMS1302A	11	0·087	0·008	0·004	0·082	0·05	0·003	0·007	0·036	0·65	0·18	0·004	0·04	0·021	1·01	0·013
NMS1304	9	n.d.	0·006	0·009	0·007	n.d.	n.d.	0·007	0·023	n.d.	0·14	0·008	0·046	0·046	0·93	0·042
NMS1305	6	0·163	0·011	0·004	0·152	0·045	0·005	0·013	0·033	n.d.	0·44	0·009	0·057	0·091	3·83	0·03
NFL1302	5	n.d.	0·006	0·004	0·214	0·025	0·003	0·008	0·021	n.d.	0·19	0·007	0·06	0·037	1·18	0·019
NFL1305	6	n.d.	0·007	n.d.	0·07	0·016	0·004	0·008	0·024	n.d.	0·15	0·003	0·034	0·069	1·88	0·014
NFL1315A	8	n.d.	0·005	0·006	0·034	0·015	0·001	0·016	0·05	0·028	0·32	0·012	0·092	0·064	2·66	0·038
NFL1316	7	n.d.	0·005	0·005	0·807	0·025	0·004	0·007	0·012	n.d.	0·18	0·003	0·02	0·032	0·86	0·025
NFL1324	4	n.d.	0·01	0·017	0·052	0·027	0·005	0·023	0·108	0·034	0·3	0·028	0·161	0·115	5·8	0·091
NTB0306	11	0·081	0·003	n.d.	0·718	0·008	n.d.	0·007	0·01	0·048	0·09	0·006	n.d.	n.d.	0·06	0·015
NFK0301	18	0·034	0·019	0·004	0·14	0·019	0·004	0·034	0·142	0·03	0·44	0·027	0·146	0·034	1·81	0·052
NFK1123	9	0·059	0·011	0·004	0·034	0·013	0·003	0·058	0·199	0·053	0·48	0·026	0·122	0·032	1·27	0·041
NFR0309	6	n.d.	n.d.	0·004	0·215	0·009	n.d.	0·008	0·02	0·024	0·12	0·007	0·033	0·068	2·06	0·021
NFR1107	7	0·096	0·005	n.d.	0·058	0·041	0·005	0·006	0·016	0·057	0·21	0·008	0·051	0·047	1·3	0·048
NMC1301	7	n.d.	0·003	0·004	0·009	0·03	0·005	0·018	0·08	n.d.	0·37	0·017	0·108	0·058	3·09	0·027
NMC1322	7	0·179	0·04	0·007	0·447	0·011	n.d.	0·02	0·027	0·185	0·4	0·012	0·041	0·026	0·5	0·044
NMM1115	7	n.d.	0·022	0·018	0·002	0·006	0·001	0·005	0·009	n.d.	0·074	0·005	0·037	0·028	1·02	0·03
NME1122	10	0·024	0·003	n.d.	0·057	0·007	n.d.	0·007	0·012	n.d.	0·1	0·003	0·035	0·023	0·58	n.d
NME0528	6	n.d.	0·005	0·008	0·034	0·01	0·002	0·001	0·01	0·02	0·17	0·005	0·029	0·03	0·84	0·027
NBN0305	9	0·11	n.d.	n.d.	0·088	0·023	n.d.	0·011	0·021	0·03	0·13	0·015	n.d.	0·04	0·47	0·057
Group IIA																
NJS1302	9	n.d.	0·002	0·003	0·038	0·031	0·002	0·007	0·025	0·051	0·12	0·01	0·069	0·139	5·34	0·045
NJS1304	10	n.d.	0·004	0·002	0·443	0·037	0·004	0·009	0·023	0·54	0·15	0·01	0·073	0·098	4·1	0·057
NJS1306	7	n.d.	0·009	0·006	0·023	0·008	0·001	0·013	0·035	n.d.	0·25	0·009	0·047	0·086	2·58	0·049
NPY1310	7	n.d.	0·009	n.d.	0·281	0·008	0·003	0·004	0·014	0·47	0·24	0·011	0·055	0·038	1·04	0·018
NPY1311	9	n.d.	0·008	0·004	0·04	0·007	0·004	0·011	0·017	n.d.	0·12	0·006	0·039	0·049	0·99	0·03
Group IIB																
NFL1327	7	n.d.	0·007	0·003	0·013	0·019	0·002	0·012	0·072	0·034	0·28	0·019	0·113	0·047	1·42	0·045
NTB1122	6	n.d.	n.d.	0·006	0·003	0·006	0·004	0·01	0·06	n.d.	0·2	0·015	0·093	0·099	3·21	0·063
NFK1108	6	n.d.	0·005	n.d.	0·007	0·014	0·006	0·009	0·04	0·04	0·29	0·015	0·086	0·044	1·31	n.d
NFK1115	6	0·147	0·004	0·007	0·006	0·045	0·003	0·01	0·043	0·015	0·44	0·017	0·076	0·036	1·67	0·057
NFR0306	8	n.d.	0·004	n.d.	0·022	0·009	n.d.	0·009	0·037	n.d.	0·18	0·007	0·054	0·042	1·07	0·03
NFR0307	13	0·054	0·007	n.d.	n.d.	0·013	n.d.	0·004	0·007	n.d.	0·06	0·003	0·038	0·028	0·47	0·021
NFR1109	12	0·023	0·005	n.d.	n.d.	0·013	0·003	0·015	0·057	0·038	0·35	0·013	0·087	0·024	0·68	0·038
NMC1309	6	n.d.	0·001	0·005	0·005	0·014	0·003	0·005	0·016	n.d.	0·12	0·006	0·041	0·031	0·79	0·021
NMM0318	8	0·114	0·008	0·009	0·008	0·01	0·005	0·012	0·055	n.d.	0·19	0·014	0·075	0·062	2·71	0·047

(continued)

Downloaded from https://academic.oup.com/petrology/article/58/6/1107/4001466 by ETH Zurich user on 30 June 2022

Table 3: Continued

Sample	Orthopyroxene															
	Eu	Gd	Tb	Ti	Dy	Ho	Y	Er	Tm	Yb	Lu	Sc	V	Cr	Co	Ni
Group IA																
NMS1308	n.d.	0·046	0·009	489	0·088	0·024	0·74	0·094	0·018	0·18	0·029	15·7	83·8	2932	60·3	757
NMS1310	0·012	0·066	0·014	678	0·13	0·038	1·05	0·14	0·031	0·26	0·049	18·3	100	3124	64·5	790
NJS1307	0·021	0·081	0·021	1008	0·17	0·051	1·49	0·2	0·038	0·35	0·063	19	109	2295	64·2	789
NPY1301	0·014	0·051	0·011	781	0·13	0·037	1·14	0·15	0·028	0·33	0·057	17	101	2462	63·1	768
NPY1314	0·015	0·057	0·014	676	0·16	0·045	1·16	0·16	0·034	0·3	0·052	18·9	104	2287	66	817
NFL1329	0·015	0·053	0·011	401	0·11	0·032	0·98	0·13	0·031	0·24	0·051	18·8	93	2346	62·6	787
NTB0307	n.d.	n.d.	0·007	318	0·07	0·021	0·65	0·097	0·022	0·19	0·034	16	83·5	2784	59·2	786
NTB1124	0·011	0·049	0·011	858	0·12	0·033	0·93	0·13	0·027	0·23	0·041	18·9	102	3687	58·1	746
NTB1116	0·016	0·061	0·015	516	0·11	0·039	0·92	0·13	0·028	0·22	0·039	19·8	100	3495	62·4	803
NMC1336A	0·016	0·065	0·017	750	0·15	0·05	1·27	0·17	0·032	0·28	0·052	17·7	90·5	3845	63·8	844
NMM1126	0·008	0·029	0·008	379	0·08	0·025	0·72	0·1	0·022	0·2	0·037	17·8	92·4	3475	58·9	769
NME1116	0·019	0·075	0·012	425	0·11	0·035	0·81	0·11	0·025	0·2	0·035	18·8	89·9	3837	62·4	767
NBN0302A	0·019	0·058	0·012	449	0·096	0·032	0·82	0·14	0·026	0·25	0·037	15·8	87·0	2531	61·4	745
NBN0311	0·014	0·048	0·012	455	0·096	0·029	0·81	0·14	0·024	0·25	0·043	15·1	86·7	2538	n.a.	n.a
NBN0316	0·019	0·059	0·012	351	0·11	0·034	0·82	0·16	0·03	0·23	0·042	16·9	84·2	2098	64·5	763
NBN0319	0·013	0·042	0·012	352	0·088	0·029	0·7	0·11	0·029	0·22	0·038	16·8	85·6	2083	n.a.	n.a
NBN0321	0·016	0·063	0·012	537	0·1	0·033	0·75	0·11	0·021	0·19	0·037	17·1	89·6	2587	66·2	901
Group IB																
NMS1302A	0·006	0·021	0·004	139	0·039	0·011	0·23	0·038	0·008	0·066	0·017	21·9	79·6	3201	59	755
NMS1304	0·014	0·044	0·008	448	0·072	0·02	0·51	0·073	0·016	0·12	0·028	21·5	104	2879	60·3	743
NMS1305	0·018	0·07	0·013	343	0·101	0·03	0·95	0·12	0·031	0·3	0·045	16·4	69·4	2318	62·2	774
NFL1302	0·007	0·051	0·016	433	0·11	0·037	1·04	0·16	0·029	0·27	0·049	20·3	99	2774	62·1	775
NFL1305	0·01	0·042	0·013	206	0·097	0·026	0·78	0·11	0·026	0·22	0·041	19·5	92	3106	61·9	792
NFL1315A	0·019	0·076	0·015	370	0·14	0·034	0·94	0·12	0·024	0·19	0·035	14·7	53·3	3955	60·2	689
NFL1316	0·009	0·037	0·003	293	0·037	0·012	0·25	0·039	0·008	0·088	0·018	24·1	93·6	3454	59·3	751
NFL1324	0·024	0·098	0·014	336	0·16	0·041	1·16	0·14	0·032	0·24	0·048	16·2	69·2	4716	62·1	812
NTB0306	0·004	0·026	0·003	248	0·027	0·008	0·23	0·034	0·008	0·07	0·013	15	69	3355	54·6	655
NFK0301	0·023	0·074	0·017	472	0·15	0·041	1·17	0·16	0·032	0·28	0·052	14·9	76·5	4112	57·2	735
NFK1123	0·013	0·048	0·01	528	0·091	0·021	0·62	0·075	0·016	0·14	0·025	18·2	77·6	4111	58·1	782
NFR0309	0·011	0·061	0·016	831	0·17	0·045	1·3	0·19	0·033	0·3	0·055	20·9	102	2237	62·5	749
NFR1107	0·014	0·072	0·013	527	0·11	0·028	0·82	0·1	0·02	0·16	0·029	22·1	101	3750	60·2	774
NMC1301	0·017	0·054	0·011	251	0·083	0·024	0·66	0·091	0·016	0·13	0·026	22·1	96·1	4064	64·8	820
NMC1322	0·018	n.d.	0·012	295	0·089	0·028	0·9	0·12	0·021	0·18	0·044	18·4	85·7	3144	57·7	758
NMM1115	0·011	0·049	0·012	485	0·093	0·028	0·9	0·13	0·023	0·21	0·042	21·4	97·5	3396	63	795
NME1122	0·008	0·029	0·006	457	0·058	0·017	0·45	0·067	0·013	0·11	0·021	14·9	85	3121	53·9	695
NME0528	0·01	0·047	0·014	438	0·095	0·032	0·82	0·12	0·023	0·2	0·039	22·3	102	3386	61·5	779
NBN0305	0·013	0·046	0·014	315	0·084	0·016	0·48	0·11	0·017	0·14	0·023	18·6	95·3	3003	61	764
Group IIA																
NJS1302	0·024	0·082	0·018	1292	0·18	0·051	1·5	0·21	0·038	0·33	0·06	17·3	94·3	2446	65·3	755
NJS1304	0·019	0·089	0·016	1171	0·17	0·047	1·28	0·18	0·033	0·29	0·053	15·9	89·3	2332	68·3	786
NJS1306	0·018	0·104	0·019	727	0·17	0·053	1·52	0·2	0·037	0·31	0·054	20·4	101	2294	65·8	818
NPY1310	0·011	0·057	0·016	776	0·13	0·046	1·25	0·19	0·036	0·31	0·053	19·6	134	1490	65·4	744
NPY1311	0·015	0·057	0·013	731	0·14	0·041	1·2	0·17	0·036	0·3	0·06	19·3	128	1418	62·2	712
Group IIB																
NFL1327	0·027	0·083	0·018	370	0·14	0·041	1·09	0·14	0·028	0·26	0·044	14·2	68·2	3314	60·5	690
NTB1122	0·027	0·107	0·025	1495	0·25	0·063	1·8	0·23	0·047	0·4	0·067	27·4	143	3200	62·8	745
NFK1108	0·017	0·077	0·021	621	0·15	0·049	1·26	0·18	0·035	0·3	0·045	22·2	106	3864	66·2	789
NFK1115	0·02	0·047	0·012	121	0·12	0·026	0·78	0·1	0·025	0·18	0·034	18·7	62·6	3252	60·8	760
NFR0306	0·013	0·051	0·013	539	0·13	0·038	1·02	0·14	0·03	0·25	0·045	15·6	83·6	3518	59·2	636
NFR0307	0·007	0·024	0·005	411	0·051	0·014	0·46	0·068	0·016	0·14	0·028	15·9	90·2	2828	59	757
NFR1109	0·015	0·05	0·012	408	0·093	0·023	0·67	0·086	0·019	0·14	0·028	11·3	60·7	3606	60·9	632
NMC1309	0·01	0·053	0·011	326	0·11	0·033	0·95	0·14	0·03	0·26	0·045	21	100	3042	60·7	765
NMM0318	0·018	0·087	0·018	538	0·15	0·037	1·28	0·18	0·039	0·34	0·057	18·6	90·8	2501	62·6	723

(continued)

Downloaded from https://academic.oup.com/petrology/article/58/6/1107/4001466 by ETH Zurich user on 30 June 2022

Table 3: Continued

Sample	Clinopyroxene																	
	n	Rb	Th	U	Ba	Nb	Ta	La	Ce	Pb	Sr	Pr	Nd	Hf	Zr	Sm	Eu	Gd
Group IA																		
NMS1308	7	0·059	0·046	0·021	0·13	0·068	0·028	1·14	3·67	0·26	61·5	0·69	4·1	1·04	36·5	1·52	0·6	1·98
NMS1310	8	0·049	0·023	0·01	0·038	0·093	0·021	1·03	3·57	n.d.	74·2	0·69	4·08	0·94	30·5	1·65	0·67	2·28
NJS1307	6	0·059	0·017	0·011	0·024	0·1	0·02	1·16	4·26	0·042	79·4	0·83	5·06	1·28	42·3	1·95	0·79	2·83
NPY1301	9	0·96	0·027	0·012	0·1	0·18	0·04	1·17	3·82	0·077	77·6	0·69	4·16	0·99	32·1	1·66	0·71	2·44
NPY1314	6	n.d.	0·29	0·21	0·023	0·036	0·019	1·17	3·64	0·094	47·2	0·68	4·25	1·11	36·8	1·84	0·72	2·69
NFL1329	7	n.d.	0·2	0·08	0·034	0·043	0·014	1·15	3·21	0·1	46·8	0·59	3·38	0·88	25·6	1·31	0·58	1·94
NTB0307	7	0·035	0·066	0·023	0·066	0·071	0·019	0·83	2·64	0·045	37·7	0·43	2·32	0·41	10·1	0·89	0·38	1·36
NTB1124	13	0·038	0·013	0·005	0·062	0·034	0·006	0·75	2·5	0·072	48·1	0·45	2·89	0·72	17·9	1·25	0·51	1·84
NTB1116	6	0·11	0·026	0·026	0·11	0·083	0·016	0·83	3·01	0·067	64·1	0·6	3·53	0·73	22·5	1·37	0·55	1·89
NMC1336A	7	0·05	0·086	0·045	0·032	0·008	0·005	0·46	2·19	0·16	41·8	0·55	3·95	0·94	26·1	1·77	0·74	2·68
NMM1126	9	0·37	0·031	0·016	0·22	0·076	0·01	0·47	1·48	0·096	26·6	0·25	1·55	0·25	5·95	0·66	0·29	1·17
NME1116	6	n.d.	0·011	0·01	0·023	0·058	0·009	0·74	2·77	0·03	63·7	0·53	2·87	0·43	16·6	0·98	0·39	1·43
NBN032A	12	0·47	0·049	0·02	0·33	0·053	0·011	0·98	3·74	0·092	50·4	0·67	4·09	0·94	28·5	1·61	0·64	2·16
NBN0311	18	0·2	0·04	0·013	0·15	0·098	0·017	1·01	3·58	0·031	60·6	0·62	3·73	0·81	25·9	1·5	0·63	2·16
NBN0316	9	0·055	0·07	0·017	0·2	0·062	n.d.	0·65	2·5	0·27	19·7	0·45	2·86	0·63	16·7	1·13	0·48	1·55
NBN0319	13	0·017	0·023	0·01	n.d.	0·031	0·006	0·61	2·58	0·23	22·4	0·48	2·73	0·61	15·2	1·06	0·43	1·41
NBN0321	23	0·21	0·029	0·014	0·37	0·093	0·017	0·85	3·35	0·17	53·6	0·63	3·93	0·92	24·5	1·85	0·75	2·82
Group IB																		
NMS1302A	4	0·11	0·057	0·43	0·29	0·51	0·075	1·14	3·18	0·09	36·4	0·54	2·75	0·18	5·5	0·57	0·2	0·56
NMS1304	11	0·73	0·044	0·014	0·087	0·047	0·012	2·89	7·87	0·3	118	1·18	5·51	0·62	16·3	1·37	0·48	1·48
NMS1305	6	0·23	0·23	0·063	0·24	0·33	0·056	4·73	14·4	0·12	100	2·25	10·2	1·72	85·8	2·47	0·88	2·59
NFL1302	7	0·067	0·11	0·032	0·54	0·19	0·011	2·21	5·07	0·065	50·4	0·71	3·46	0·68	20·5	1·29	0·52	1·91
NFL1305	6	0·11	0·19	0·056	0·045	0·28	0·083	3·35	7·73	0·044	55·7	1·04	4·19	0·81	36·5	1·02	0·39	1·36
NFL1315A	7	n.d.	0·15	0·028	0·24	0·31	0·05	7·57	23·3	0·15	185	3·84	17·9	2·33	78	3·95	1·32	3·47
NFL1316	7	0·094	0·098	0·021	1·3	0·068	0·021	2·35	4·67	0·075	58	0·6	2·82	0·52	19·1	0·76	0·28	0·76
NFL1324	7	0·051	0·41	0·13	0·23	0·52	0·12	13·5	39·2	0·43	169	5·98	26·4	2·4	122	5·16	1·59	4·26
NTB0306	8	0·13	0·3	0·054	0·41	0·04	n.d.	3·6	5·07	0·12	74·7	0·37	1·06	0·09	1·72	0·34	0·15	0·57
NFK0301	16	0·046	0·15	0·036	0·059	0·44	0·078	11·3	34·7	0·075	147	4·68	19·3	0·58	32·9	3·73	1·25	3·16
NFK1123	9	n.d.	0·17	0·077	0·12	0·24	0·045	13·6	37	1·47	113	4·33	15·7	0·56	23	2·24	0·65	1·94
NFR0309	6	n.d.	0·53	0·14	0·049	0·47	0·037	3	6·77	0·064	47·2	0·99	4·99	1·12	39·1	1·88	0·77	2·67
NFR1107	6	n.d.	0·12	0·047	0·035	0·1	0·013	1·5	5·4	0·07	107	1·05	5·78	0·82	27·4	1·61	0·65	2·01
NMC1301	8	n.d.	0·2	0·041	0·15	1·12	0·26	10	27·8	0·08	185	3·81	14·6	1	55·7	2·28	0·77	1·7
NMC1322	8	0·13	0·15	0·037	0·54	0·29	0·068	2·59	6·61	0·14	51·4	1·01	4·81	0·35	10·3	1·21	0·41	1·53
NMM1115	5	n.d.	3·48	1·06	0·063	0·07	0·008	1·31	2·54	0·055	45·4	0·47	2·98	0·58	20·2	1·17	0·49	1·73
NME1122	12	0·17	0·3	0·077	0·069	0·064	0·006	2·15	4·14	0·069	45	0·49	2·51	0·47	13·8	0·94	0·39	1·31
NME0528	7	0·08	0·13	0·025	0·096	0·2	0·063	4·38	12·4	0·1	106	1·88	8·28	0·99	41·7	2·06	0·71	2·04
NBN0305	9	0·26	0·025	0·011	0·51	0·049	n.d.	1·49	4·1	0·16	92·6	0·67	3·47	0·39	8·12	1·12	0·36	1·23
Group IIA																		
NJS1302	9	0·038	0·023	0·013	0·095	0·035	0·023	1·97	9·51	n.d.	47·5	2·06	11·9	3·27	127	3·87	1·36	4·52
NJS1304	4	0·086	0·032	0·01	0·27	0·083	0·036	2·13	9·73	0·062	56·4	2·02	11·3	2·49	100	3·29	1·16	3·72
NJS1306	7	n.d.	0·055	0·017	0·042	0·02	0·007	2·14	5·66	0·065	69·6	0·93	5·14	1·14	37·2	1·85	0·79	2·57
NPY1310	7	0·054	0·009	0·006	0·27	0·035	0·013	1·03	3·53	0·087	40	0·66	3·76	0·78	17·3	1·54	0·62	2·36
NPY1311	10	0·15	0·012	0·008	0·09	0·044	0·012	1·02	3·58	0·043	39·9	0·66	3·81	0·73	16·9	1·52	0·63	2·36
Group IIB																		
NFL1326	7	n.d.	0·1	0·022	0·091	0·24	0·034	4·53	13·1	0·061	96·6	2·1	9·81	1·02	30	2·55	0·92	2·81
NFL1327	7	n.d.	0·069	0·017	0·14	0·29	0·04	6·38	20·1	0·064	118	3·22	15·1	0·33	22·5	3·35	1·14	2·8
NTB1122	6	n.d.	0·12	0·042	0·091	0·14	0·058	3·62	12·6	0·068	68·4	2·28	12·3	1·36	39·7	3·51	1·19	3·82
NFK1108	6	0·078	0·047	0·016	0·25	0·15	0·021	2·96	9·13	0·082	87·2	1·46	6·93	0·59	18·2	1·8	0·74	2·14
NFK1115	5	n.d.	0·066	0·011	0·11	0·16	0·019	6·38	20·7	0·076	170	3·36	15·4	0·85	47·1	3·21	1·03	2·67
NFR0306	13	0·067	0·068	0·014	0·38	0·14	0·019	3·51	11·8	0·045	83·6	1·74	8·02	0·79	22·1	2·08	0·83	2·35
NFR0307	15	0·11	0·16	0·075	0·06	0·082	0·017	1·21	3·75	0·076	42·5	0·54	2·59	0·37	9·79	0·67	0·25	0·88
NFR1109	10	0·033	0·093	0·027	0·039	0·14	0·017	4·87	16·1	0·072	132	2·37	10·8	0·38	17·4	2·43	0·91	2·2
NMC1309	8	n.d.	0·035	0·011	0·15	0·078	0·015	2·05	5·82	0·05	57·1	0·82	3·69	0·41	13·2	1·04	0·46	1·5
NMM0318	6	n.d.	0·5	0·14	0·097	0·19	0·014	6·27	18·4	0·1	87·4	2·8	12·5	1·11	47·9	2·91	1·11	3·06

(continued)

Downloaded from https://academic.oup.com/petrology/article/58/6/1107/4001466 by ETH Zurich user on 30 June 2022

Table 3: Continued

Sample	Clinopyroxene															
	Tb	Ti	Dy	Ho	Y	Er	Tm	Yb	Lu	Sc	V	Cr	Co	Ni	La_N/Lu_N	ΣREE
Group IA																
NMS1308	0·35	2298	2·49	0·52	13·8	1·5	0·2	1·3	0·18	60·8	248	8006	20·1	323	0·64	20·2
NMS1310	0·42	2965	2·99	0·66	17·2	1·93	0·27	1·8	0·27	68·5	272	6932	21·5	333	0·4	22·3
NJS1307	0·5	4265	3·66	0·81	21	2·28	0·32	2·2	0·32	65·5	278	4912	22·7	344	0·38	26·9
NPY1301	0·44	3355	3·24	0·72	18·9	2·08	0·3	2·07	0·29	64·1	270	5547	21	329	0·42	23·8
NPY1314	0·5	3430	3·54	0·79	20·6	2·25	0·33	2·17	0·29	62	263	4956	22·9	369	0·42	24·9
NFL1329	0·36	1815	2·65	0·58	15	1·65	0·23	1·57	0·22	63·7	240	4462	21·4	342	0·54	19·4
NTB0307	0·26	1553	2·01	0·44	11·4	1·31	0·19	1·28	0·18	61·1	255	6129	22	372	0·49	14·5
NTB1124	0·34	3597	2·5	0·54	13·8	1·55	0·22	1·45	0·2	65	287	8177	23·3	374	0·4	17
NTB1116	0·35	2070	2·53	0·57	14·5	1·51	0·22	1·47	0·19	70·5	273	7609	20·6	329	0·45	18·6
NMC1336A	0·49	2954	3·56	0·76	19·9	2·13	0·27	1·8	0·24	65·1	247	7565	21·2	352	0·2	21·6
NMM1126	0·23	1606	1·9	0·44	11·4	1·34	0·2	1·35	0·19	65·9	265	7441	23·7	390	0·26	11·5
NME1116	0·25	1648	1·97	0·44	11·7	1·3	0·19	1·31	0·19	69·9	267	7205	20·7	330	0·4	15·4
NBN032A	0·38	2067	2·55	0·53	13·7	1·52	0·21	1·53	0·2	57·8	241	6083	22·2	353	0·51	20·8
NBN0311	0·41	2381	2·88	0·59	15·5	1·79	0·24	1·65	0·24	60·6	265	5966	n.a.	n.a.	0·44	21
NBN0316	0·29	1290	1·97	0·41	10·1	1·16	0·16	1·03	0·15	44·6	178	3287	23·4	367	0·44	14·8
NBN0319	0·24	1161	1·72	0·31	8·24	1·04	0·13	0·93	0·13	40	164	2971	n.a.	n.a.	0·44	13·8
NBN0321	0·5	3614	3·23	0·64	15·6	1·79	0·23	1·47	0·21	75·4	329	6354	23·1	368	0·42	22·2
Group IB																
NMS1302A	0·091	299	0·57	0·11	2·98	0·31	0·047	0·31	0·056	68·7	182	6246	21·3	350	2·13	10·4
NMS1304	0·23	1419	1·48	0·28	7·18	0·71	0·1	0·7	0·096	70	250	5845	20·9	342	3·14	24·4
NMS1305	0·44	1548	3·16	0·71	18	1·97	0·29	1·93	0·28	61·8	219	4913	21	331	1·75	46·2
NFL1302	0·35	1918	2·65	0·61	15·6	1·76	0·24	1·73	0·24	67·9	257	5692	21·2	341	0·95	22·7
NFL1305	0·25	870	1·91	0·46	11·8	1·38	0·2	1·36	0·19	64·3	236	5873	21·1	335	1·8	24·8
NFL1315A	0·51	860	3·05	0·56	14·4	1·5	0·19	1·23	0·18	68·2	188	8606	20·4	302	4·36	68·6
NFL1316	0·12	813	0·73	0·15	3·89	0·45	0·06	0·51	0·079	90·4	267	6970	20·2	335	3·11	14·3
NFL1324	0·57	1187	3·47	0·66	16·8	1·7	0·23	1·39	0·19	60·5	179	8631	21·1	351	7·49	104
NTB0306	0·11	808	0·82	0·19	4·39	0·56	0·08	0·54	0·081	73·7	262	7253	21·5	338	4·64	13·5
NFK0301	0·46	1743	3·09	0·6	15·9	1·68	0·24	1·63	0·23	59·1	230	8972	21·5	352	5·07	86·2
NFK1123	0·28	2011	1·75	0·35	9·03	0·95	0·13	0·89	0·12	58·3	231	9029	22·9	385	12	79·9
NFR0309	0·5	3825	3·66	0·77	20·6	2·23	0·3	2·06	0·3	62·5	266	5138	21·1	314	1·04	30·9
NFR1107	0·32	1834	2·18	0·47	11·7	1·23	0·17	1·02	0·14	82·7	284	8539	20·8	332	1·13	23·5
NMC1301	0·26	690	1·56	0·31	8·32	0·83	0·12	0·72	0·099	82·8	267	8910	22·2	359	10·5	64·9
NMC1322	0·28	1179	2·2	0·5	13·6	1·5	0·22	1·56	0·22	71·7	242	6893	20·1	338	1·26	24·6
NMM1115	0·31	1778	2·26	0·5	13	1·45	0·21	1·28	0·19	72·6	267	7089	20·5	331	0·71	16·9
NME1122	0·23	2257	1·59	0·32	8·3	0·89	0·13	0·87	0·12	58	291	8366	23·1	382	1·82	16·1
NME0528	0·32	1399	2·15	0·44	10·9	1·15	0·16	1·07	0·14	78·1	267	9184	20·9	324	3·18	37·2
NBN0305	0·2	1166	1·29	0·26	6·53	0·76	0·11	0·71	0·1	65·8	256	6000	22·8	370	1·53	15·9
Group IIA																
NJS1302	0·74	6627	5·04	1·03	26·3	2·79	0·39	2·58	0·35	62·4	272	5784	21·6	320	0·59	48·1
NJS1304	0·6	5965	4·01	0·83	21·6	2·32	0·33	2·25	0·3	66·7	268	5687	22	329	0·74	44
NJS1306	0·46	3051	3·29	0·71	18·6	2·03	0·27	1·91	0·27	59·3	254	4690	23·8	354	0·84	28
NPY1310	0·45	3353	3·22	0·71	18·3	1·96	0·28	1·9	0·28	66·8	327	2838	22·7	343	0·38	22·3
NPY1311	0·44	3261	3·26	0·7	18·5	2·07	0·29	1·96	0·28	62·7	319	2969	22·3	321	0·38	22·6
Group IIB																
NFL1326	0·43	2220	2·94	0·6	15·3	1·62	0·24	1·6	0·22	57·1	244	5889	21·2	259	2·18	43·4
NFL1327	0·42	1209	2·54	0·5	13·4	1·4	0·2	1·37	0·19	49·6	196	6927	21·7	306	3·47	58·7
NTB1122	0·6	5783	3·99	0·8	20·6	2·21	0·3	1·99	0·28	66·7	315	5617	23·1	332	1·35	49·5
NFK1108	0·38	2010	2·58	0·54	14	1·54	0·21	1·49	0·21	65	258	7408	22·2	327	1·46	32·1
NFK1115	0·37	319	2·17	0·44	11	1·13	0·17	1·15	0·15	84·6	238	8804	20·6	334	4·45	58·2
NFR0306	0·39	2040	2·7	0·56	14·2	1·65	0·24	1·6	0·22	63·8	281	7723	23·6	318	1·63	37·6
NFR0307	0·17	1880	1·33	0·31	7·95	0·93	0·14	1	0·14	61·8	274	6516	23·9	400	0·89	13·9
NFR1109	0·32	1184	1·92	0·36	9·2	0·95	0·14	0·95	0·13	61·2	243	10559	24·9	330	3·85	44·4
NMC1309	0·29	1235	2·12	0·48	13·2	1·48	0·21	1·49	0·21	66·7	254	6156	21·1	332	1·02	21·7
NMM0318	0·5	2072	3·43	0·72	18·6	2·05	0·28	1·93	0·27	55·8	226	4815	21·9	318	2·4	56·2

(continued)

Downloaded from https://academic.oup.com/petrology/article/58/6/1107/4001466 by ETH Zurich user on 30 June 2022

Table 3: Continued

Sample	Amphibole															
	n	Rb	Th	U	Ba	Nb	Ta	La	Ce	Pb	Sr	Pr	Nd	Hf	Zr	Sm
Group IA																
NMS1308	3	4·51	0·024	0·017	33·6	6·21	0·41	0·87	3·38	0·12	135	0·72	4·39	0·86	26·7	1·97
NFL1329	3	2·71	0·2	0·091	20·1	2·75	0·19	1·38	3·79	0·3	127	0·69	3·9	0·86	26·9	1·74
Group IB																
NMS1304	7	7·53	0·092	0·016	210	3·55	0·41	5·96	15·2	0·71	354	2·15	9·84	0·87	27·4	2·31
NFL1302	2	6·35	0·11	0·028	83·3	13·2	0·38	3·17	7·48	0·12	137	0·99	4·51	0·66	23·5	1·59
NFL1315A	5	7·44	0·28	0·059	156	72·5	3·46	13·5	39·9	0·45	433	6·24	29·1	3·25	127	6·4
NFL1324	7	12·3	0·58	0·18	322	80·9	4·56	22·1	60·7	1·65	424	8·79	39·1	4·1	174	7·44
Group IIA																
NJS1302_1	1	n.d.	n.d.	0·017	0·94	1·04	0·069	1·26	7·15	n.d.	208	1·72	12	1·74	64·7	4·38
NJS1302_2	1	0·223	n.d.	0·027	1·44	1·85	0·28	2·65	12·1	n.d.	197	2·42	14	2·28	87·6	4·27
Group IIB																
NFL1326	6	7·75	0·11	0·026	132	17·4	0·74	5·55	15·7	0·24	252	2·41	11·6	1·02	33·3	2·94

Sample	Amphibole															
	Eu	Gd	Tb	Ti	Dy	Ho	Y	Er	Tm	Yb	Lu	Sc	V	Cr	Co	Ni
Group IA																
NMS1308	0·81	2·58	0·46	14491	3·24	0·7	18·3	1·89	0·26	1·64	0·24	44·9	363	9605	39·6	812
NFL1329	0·68	2·48	0·44	9885	3·28	0·72	19·1	2·1	0·31	2	0·27	50·3	406	7344	42·4	929
Group IB																
NMS1304	0·84	2·57	0·38	8139	2·52	0·49	12·7	1·27	0·17	1·07	0·17	82	543	11501	39·2	885
NFL1302	0·71	2·23	0·44	9205	3·22	0·73	19·4	2·21	0·29	1·94	0·27	53·3	414	8831	38·6	836
NFL1315A	2·1	5·49	0·76	11278	4·49	0·83	20·9	2·1	0·26	1·64	0·22	51·8	310	13109	36·8	748
NFL1324	2·27	6	0·8	8683	4·68	0·87	22·4	2·11	0·28	1·71	0·23	53·9	327	13314	39·6	914
Group IIA																
NJS1302_1	1·58	5·96	1·03	37920	6·85	1·36	34·7	3·41	0·43	2·48	0·39	54·1	539	4201	46·4	799
NJS1302_2	1·46	4·59	0·78	25602	4·95	1·06	27·7	2·82	0·34	2·58	0·3	45·3	372	7806	48·2	928
Group IIB																
NFL1326	1·03	3·12	0·49	10243	3·27	0·67	17·3	1·81	0·25	1·62	0·23	45·9	402	10995	40·1	625

n, number of analyses; n.d., not detected; n.a., not analyzed.

Downloaded from https://academic.oup.com/petrology/article/58/6/1107/4001466 by ETH Zurich user on 30 June 2022

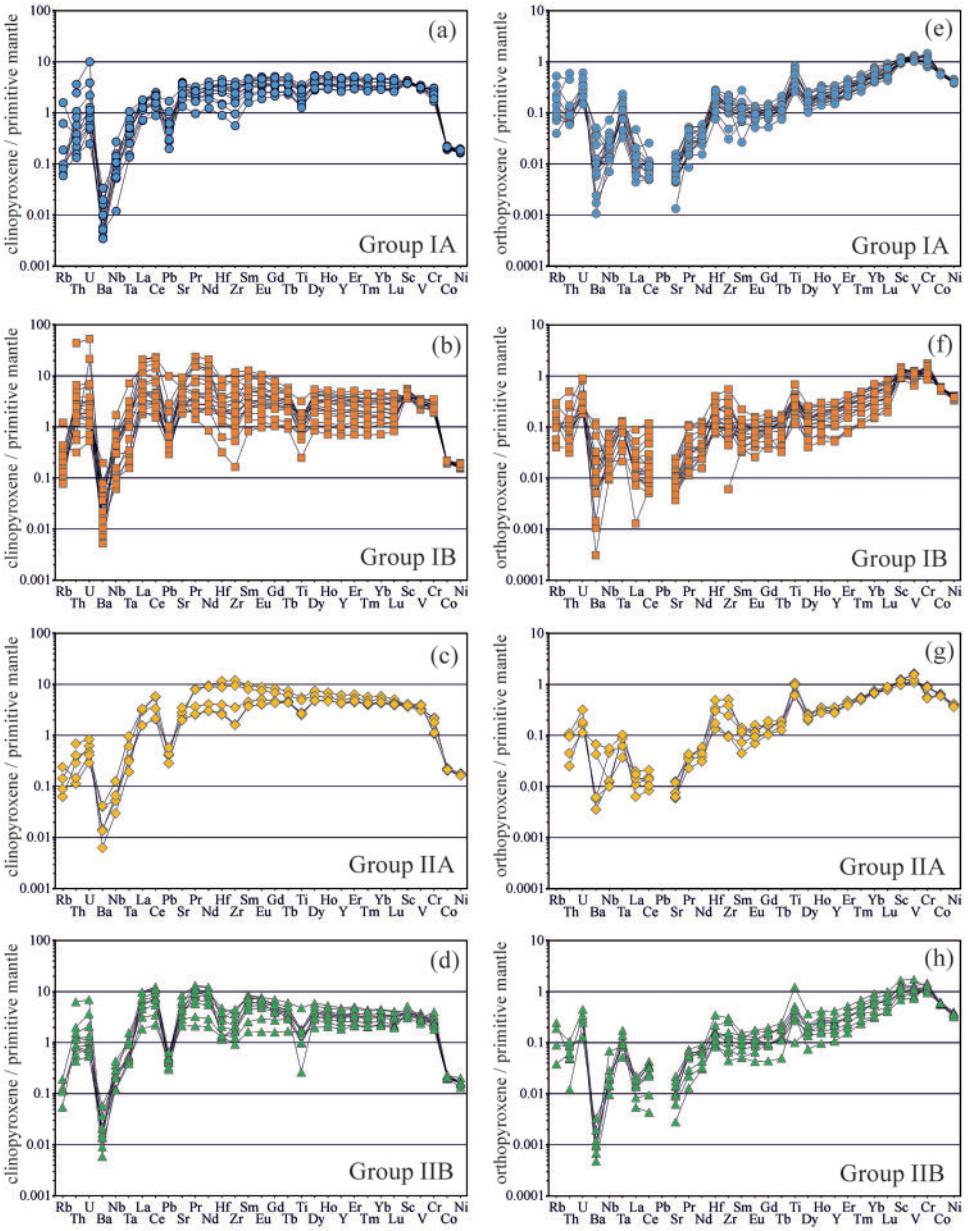

Fig. 5. Primitive mantle (McDonough & Sun, 1995) normalized multi-element diagrams for clinopyroxenes (a–d) and orthopyroxenes (e–h) of Group IA, IB, IIA and IIB xenoliths.

in sample NJS1302, where the two amphibole grains are different in composition and are ferri-kaersutite and Ti-rich magnesio-hastingsite, owing to their high TiO_2 content (8·09 and 4·24 wt %, respectively; Table 2) compared with the other samples, which have TiO_2 concentrations between 1·38 and 2·01 wt % (Table 2). K_2O is higher in the more Cr_2O_3-rich samples: the highest values (1·13, 1·09 and 1·17 wt %) occur in the same xenoliths as the highest Cr_2O_3 concentrations (1·76, 2·18 and 2·03 wt %, respectively) (Table 2). Amphibole in NJS1302 also shows lower Cr_2O_3 and higher FeO than the other xenoliths (Table 2).

As modal compositions and textural types show no visible link with geochemical characteristics, a division has been made based on major element geochemistry. Two major groups can be distinguished using the Mg# of olivine and pyroxenes. Group I is characterized by olivine Mg# = 0·89–0·91 (usual lherzolitic mantle composition; Arai, 1994) and depicts a normal mantle-depletion trend in terms of spinel Cr# and the relationship of Na and Al in clinopyroxene. Group II xenoliths have Mg# lower than 0·89, enrichment in Fe and Mn in olivine and orthopyroxene, and in some cases, elevated Ti contents in spinel. These xenoliths occur only in the northern and central parts of the NGVF.

TRACE ELEMENT GEOCHEMISTRY OF PYROXENE AND AMPHIBOLE

Trace element contents of clino- and orthopyroxenes (Table 3) were measured to provide further insights into

Downloaded from https://academic.oup.com/petrology/article/58/6/1107/4001466 by ETH Zurich user on 30 June 2022

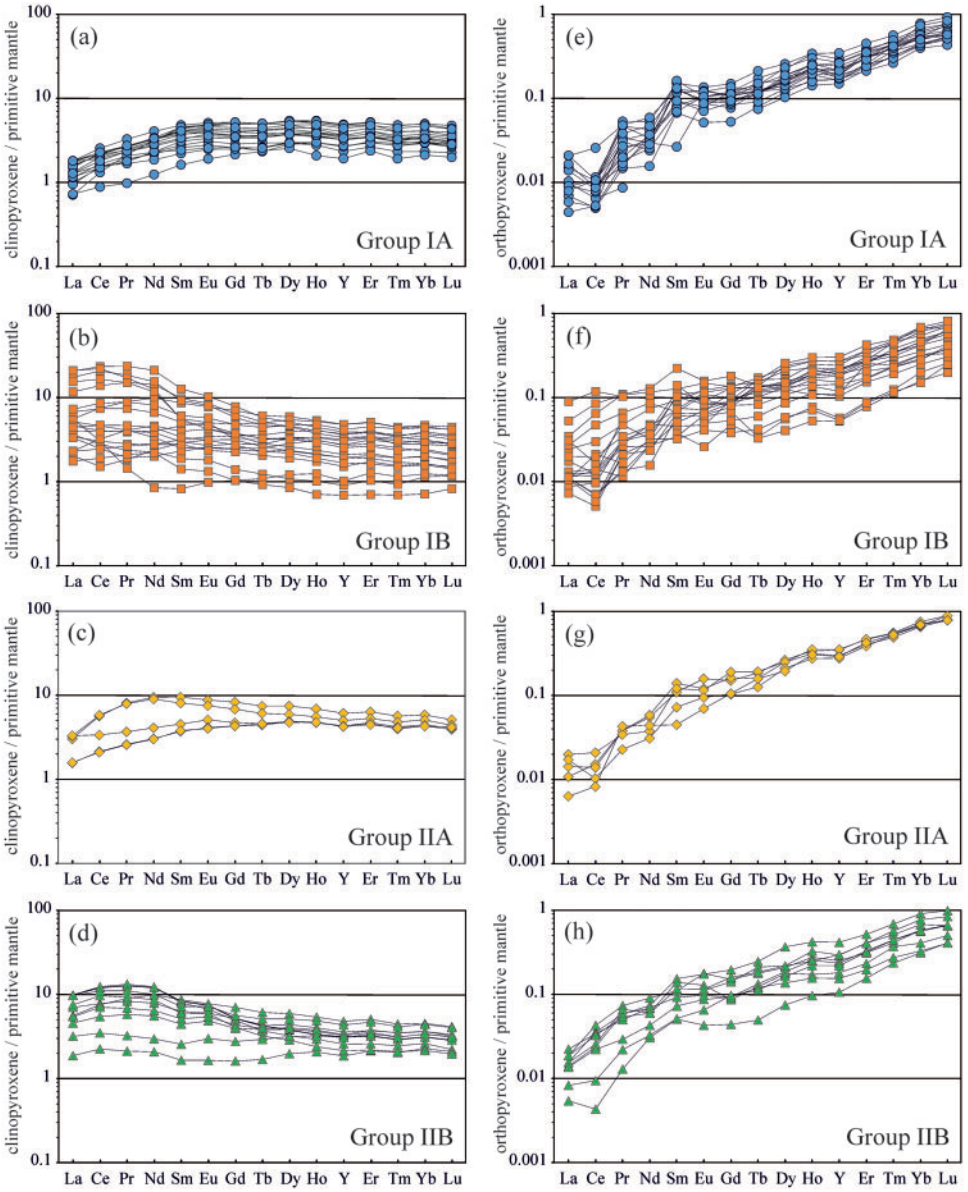

Fig. 6. Primitive mantle (McDonough & Sun, 1995) normalized REE–Y patterns of clinopyroxenes (a–d) and orthopyroxenes (e–h) of Group IA, IB, IIA, and IIB xenoliths.

the geochemical evolution of the SCLM beneath the area. Trace element contents are highly variable in the xenoliths and show no obvious relationship to major element concentrations, allowing further subdivision of Group I and II xenoliths based on trace element compositions and REE patterns.

In general, highly incompatible trace elements, such as Ba and Pb, as well as the compatible elements Co and Ni, show low values compared with the primitive mantle (PM) (McDonough & Sun, 1995) in both pyroxenes. The less incompatible high field strength elements (HFSE), such as Zr, Hf and Ti, form troughs in clinopyroxenes and positive peaks in orthopyroxenes, whereas Nb and Ta are depleted in both pyroxenes compared with LREE on PM-normalized multi-element diagrams (Fig. 5a–h). In contrast, Th and U are more enriched compared with large ion lithophile elements (LILE) in pyroxenes from almost all xenoliths. The compatible elements, particularly Sc and V, show a very narrow range in all samples.

Rare earth elements, especially LREE, are highly variable in both Group I and Group II xenoliths. Clinopyroxene La_n/Lu_n ratios range from 0·20 to 12·0 (Table 3). Because LREE enrichment commonly is considered to indicate the effects of cryptic metasomatism, both groups have been divided into an LREE-depleted ('A') and an LREE-enriched, flat or convex-upward ('B') subgroup. REE + Y patterns for clinopyroxene and orthopyroxene in these subgroups are illustrated in Fig. 6a–d and e–h, respectively. Group IA, which comprises most of the xenoliths from the southern part, has very similar clinopyroxene REE patterns within the group

Downloaded from https://academic.oup.com/petrology/article/58/6/1107/4001466 by ETH Zurich user on 30 June 2022

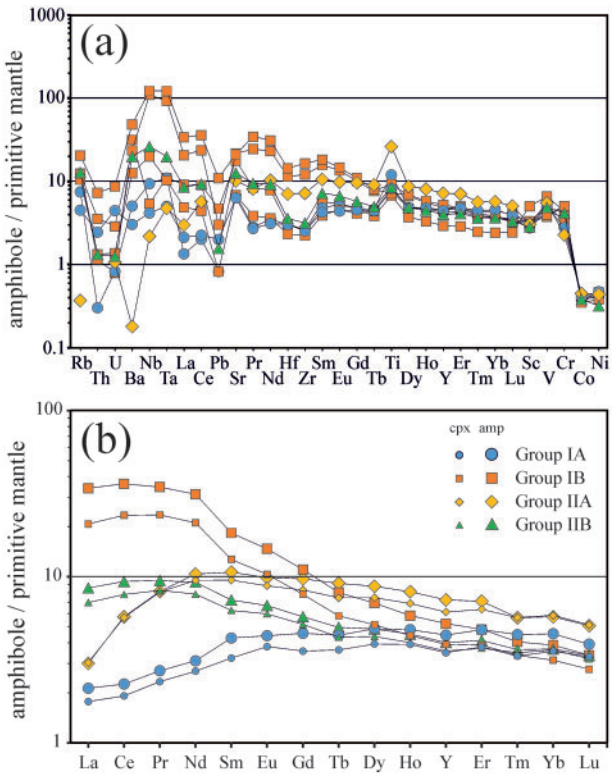

Fig. 7. (a) Multielement patterns of amphiboles in the studied xenoliths. (b) REE–Y patterns of representative amphiboles compared with clinopyroxenes within the same xenoliths from Group IA, IB, IIA and IIB; normalizing values for primitive mantle are from McDonough & Sun (1995).

(Fig. 6a). Group IB, on the other hand, displays an extremely wide range of LREE concentrations (La = 0·83–13·6), as well as heavy REE (HREE) values (Lu = 0·056–0·301) (Table 3).

The Fe–Mn–Ti-enriched Group II has an LREE-depleted subgroup (Group IIA, Fig. 6c) and an enriched one (Group IIB, Fig. 6d). Group IIA contains only samples from the northern part, from localities Podrečany and Jelšovec. It shows wide variation in the concentrations of the highly incompatible LREE, except La; two xenoliths (NJS1302, NJS1304) show considerably higher values in these elements (Table 3). Group IIB consists of xenoliths from the central part, showing very similar REE patterns with different degrees of LREE enrichment. The most incompatible elements, such as Th, U, Nb and Ta, also display a wider range of values in the LREE-rich subgroups (Group IB and IIB, Fig. 5b and d) than in the LREE-poor ones (Group IA and IIA, Fig. 5a and c), where they are consequently less abundant. Furthermore, the troughs at Zr and Hf in clinopyroxene are more emphasized in Group IB and IIB than in IA and IIA, respectively (Fig. 5a–d).

In contrast to the variability of trace element contents in the xenoliths from the northern and central part, samples from the southern part display generally low LREE contents in both pyroxenes; NBN0305 has the highest values and thus has been classified as Group IB (Table 3). Furthermore, there is a difference in the HREE concentrations of the clinopyroxenes between porphyroclastic and equigranular xenoliths from the southern part; the latter have lower values (ΣREE = 13·8–15·9 ppm) than the former (ΣREE = 20·8–22·2 ppm; Table 3). This correlation is not observed in xenoliths from the northern or central parts.

Amphibole shows wide variability in the most incompatible elements, and less in the more compatible ones (Fig. 7a). Peaks are seen in Nb, Ta and Ti, whereas Zr and Hf display slight depletion in the primitive-mantle-normalized multi-element patterns (Fig. 7a). The amphiboles are uniformly depleted in U, Th and Pb, but most of them show high Sr and Ba, except for NJS1302, which has very low Ba (1·19 ppm, Table 3). Rare earth element patterns of amphibole indicate equilibrium with coexisting clinopyroxene in each sample (Fig. 7b); therefore, LREE-depleted and -enriched characters are both present in amphibole as well.

WHOLE-ROCK GEOCHEMICAL COMPOSITIONS

Major elements

Whole-rock major element compositions (Table 4) were calculated from analyses of the mineral constituents using a mass-balance approach. The modal analyses may not be representative, owing to the small size of the xenoliths, and this uncertainty will be propagated in the calculated bulk-rock compositions; however, several conclusions can still be drawn. Contents of MgO are compared with those of the less refractory major elements in Fig. 8. The studied xenoliths show negative correlations between MgO and Al_2O_3, TiO_2, CaO and Na_2O (Fig. 8a–d, respectively), in accordance with the general pattern observed in mantle peridotites. The highest contents of basalt-related elements and the lowest MgO contents are observed in a group of xenoliths from the northern part, whereas samples from the southern part tend to remain on the other end of the trend, and those from the central part cover a wider range. The scattering of the data is due to the Group II xenoliths, which plot to the left of the main trend, reflecting a decrease in MgO content. This is clearly linked to the lower Mg# of olivine (Fig. 4a and b) and orthopyroxene (Fig. 4c). Interestingly, whole-rock FeO contents do not seem to correlate with MgO, as Group I xenoliths often show higher FeO concentrations without a decrease in MgO (Table 4).

Rare earth elements

Whole-rock trace element contents (Table 4) have been determined by mass-balance calculation. Olivine and spinel compositions have been calculated with the use of the mineral/melt distribution coefficients of Hart & Dunn (1993), Ionov *et al.* (2002) and references therein. Trace element contents of orthopyroxene have also been recalculated because of analytical uncertainties in the case of the most incompatible elements, which are present in very low concentrations (e.g. LREE). The

Downloaded from https://academic.oup.com/petrology/article/58/6/1107/4001466 by ETH Zurich user on 30 June 2022

Table 4: Whole-rock major element (wt %) and trace element (ppm) compositions of the studied xenoliths, calculated by mass balance

Sample	SiO_2	TiO_2	Al_2O_3	Cr_2O_3	FeO	MnO	MgO	CaO	Na_2O	NiO	Th	U	Nb	Ta	La	Ce	Pb
Group IA																	
NMS1308	44·2	0·06	2·3	0·59	8·29	0·13	42·1	2·06	0·15	0·31	0·004	0·002	0·015	0·003	0·11	0·34	0·025
NMS1310	48·8	0·1	2·73	0·34	7·42	0·13	38·2	2·63	0·24	0·23	0·003	0·001	0·014	0·002	0·12	0·4	
NJS1307	43·8	0·11	2·95	0·33	8·88	0·14	41·2	2·56	0·25	0·31	0·002	0·001	0·016	0·002	0·14	0·52	0·005
NPY1301	42·8	0·05	2·18	0·29	9·44	0·14	43·9	1·36	0·13	0·33	0·002	0·001	0·016	0·002	0·072	0·24	0·005
NPY1314	45·4	0·13	4·29	0·49	7·91	0·14	37	3·97	0·28	0·25	0·052	0·037	0·008	0·003	0·21	0·67	0·017
NFL1329	43·5	0·05	1·8	0·23	8·67	0·13	43	2·59	0·16	0·33	0·023	0·009	0·009	0·002	0·14	0·38	0·013
NTB0307	44·4	0·03	1·15	0·19	7·97	0·12	43·3	3·28	0·17	0·33	0·01	0·004	0·013	0·003	0·13	0·41	0·007
NTB1124	44·6	0·11	2·68	0·62	7·59	0·13	41·7	2·76	0·15	0·28	0·002	0·001	0·005	0·001	0·092	0·31	0·009
NTB1116	44·5	0·05	2·47	0·59	7·92	0·13	41·8	2·28	0·19	0·3	0·003	0·003	0·011	0·002	0·085	0·31	0·007
NMC1336A	43·8	0·06	2·75	0·8	8·11	0·12	42·4	1·87	0·14	0·32	0·007	0·004	0·001	0	0·038	0·18	0·014
NMM1126	45·7	0·05	2·3	0·41	7·75	0·14	41·5	2·38	0·15	0·28	0·003	0·002	0·01	0·001	0·048	0·15	0·01
NME1116	44·4	0·05	3	0	7·84	0·13	41·3	2·52	0·18	0·29	0·001	0·001	0·008	0·001	0·083	0·31	0·003
NBN0302A	42·1	0·03	0·91	0·18	9·18	0·14	46·5	1·32	0·05	0·33	0·003	0·001	0·004	0·001	0·055	0·21	0·005
NBN0311	41·5	0·06	1·32	0·39	8·81	0·14	45	2·27	0·17	0·29	0·004	0·001	0·013	0·002	0·11	0·38	0·003
NBN0316	42·3	0·05	1·34	0·2	9·14	0·14	44·4	2·06	0·05	0·34	0·006	0·001	0·007	0	0·058	0·22	0·025
NBN0319	43·6	0·05	1·55	0·19	8·65	0·15	42·2	3·02	0·05	0·27	0·003	0·001	0·005	0·001	0·079	0·33	0·031
NBN0321	42·7	0·07	1·53	0·31	8·68	0·13	44·2	2·29	0·12	0·31	0·003	0·001	0·012	0·002	0·087	0·34	0·018
Group IB																	
NMS1302A	42·5	0	0·58	0·43	8·05	0·12	47·3	1·24	0·03	0·37	0·003	0·022	0·039	0·004	0·059	0·17	0·005
NMS1304	43·2	0·04	1·17	0·37	8·57	0·13	44·3	1·61	0·08	0·34	0·004	0·001	0·04	0·005	0·24	0·64	0·026
NMS1305	44·1	0·04	3·93	0·6	8·77	0·14	40·5	2·12	0·15	0·3	0·021	0·006	0·042	0·005	0·44	1·33	0·012
NFL1302	41·2	0·04	3·62	0·83	8·61	0·13	43·4	1·85	0·11	0·35	0·009	0·003	0·035	0·001	0·18	0·43	0·006
NFL1305	45·9	0·03	2·39	0·42	7·56	0·13	40·2	2·8	0·17	0·27	0·023	0·007	0·043	0·01	0·41	0·95	0·006
NFL1315A	41·2	0·03	0·5	0·49	9·88	0·15	47·1	0·61	0·06	0·34	0·003	0·001	0·088	0·005	0·18	0·56	0·004
NFL1316	42·3	0·02	1·45	1·14	8·62	0·13	45·4	1·23	0·06	0·34	0·005	0·001	0·006	0·001	0·12	0·25	0·004
NFL1324	46·8	0·05	2·41	0·78	7·13	0·13	40·7	1·6	0·14	0·27	0·03	0·009	1·26	0·075	1·04	3	0·05
NTB0306	43·5	0·03	0·6	0·24	8·41	0·16	45·3	2·22	0·12	0·32	0·03	0·005	0·005	0	0·37	0·52	0·013
NFK0301	43·7	0·02	0·96	0·2	8·8	0·15	44·8	1·36	0·07	0·31	0·009	0·002	0·038	0·005	0·67	2·07	0·005
NFK1123	45·9	0·04	1·69	0·47	7·44	0·13	42·8	1·37	0·08	0·27	0·009	0·004	0·021	0·002	0·71	1·96	0·084
NFR0309	44·2	0·1	2·9	0·32	8·51	0·14	40·7	2·67	0·21	0·29	0·063	0·017	0·071	0·004	0·37	0·83	0·008
NFR1107	44·3	0·04	1·36	0·44	7·88	0·13	43·8	1·68	0·11	0·32	0·008	0·003	0·011	0·001	0·11	0·39	0·005
NMC1301	42·7	0·01	1·22	0·8	9·01	0·13	45·1	1·2	0·07	0·36	0·01	0·002	0·09	0·014	0·52	1·46	0·004
NMC1322	42·6	0·02	2·47	0·65	8·59	0·13	43·9	1·83	0·13	0·35	0·012	0·003	0·032	0·006	0·21	0·55	0·012
NMM1115	42·6	0·03	1·63	0·53	8·41	0·12	45	1·43	0·08	0·35	0·21	0·064	0·006	0·001	0·081	0·16	0·004
NME1122	43·3	0·05	1·25	0·29	8·42	0·13	44·8	2·44	0·15	0·29	0·034	0·009	0·009	0·001	0·24	0·47	0·008
NME0528	43·2	0·02	1	0·48	8·77	0·14	44·8	1·42	0·08	0·34	0·008	0·001	0·018	0·004	0·27	0·77	0·006
NBN0305	43·1	0·03	0·7	0·16	8·52	0·14	45·6	1·49	0·05	0·32	0·002	0·001	0·004	0	0·093	0·26	0·01
Group IIA																	
NJS1302	43	0·17	2·57	0·4	10·12	0·14	41	2·33	0·23	0·31	0·003	0·001	0·006	0·003	0·22	1·08	
NJS1304	41·8	0·07	2·53	0·44	10·8	0·15	43·4	1·14	0·12	0·34	0·002	0	0·007	0·002	0·11	0·51	0·003
NJS1306	42·6	0·11	4·13	0·53	10·15	0·16	38·6	3·59	0·27	0·3	0·009	0·003	0·004	0·001	0·37	0·98	0·011
NPY1310	43·1	0·12	3·62	0·26	9·22	0·14	38·9	3·92	0·26	0·29	0·002	0·001	0·007	0·002	0·19	0·64	0·016
NPY1311	44·7	0·13	3·5	0·24	8·74	0·15	37·7	4·17	0·28	0·26	0·002	0·002	0·01	0·002	0·2	0·69	0·008
Group IIB																	
NFL1326	41·2	0·09	1·21	0·41	12·98	0·24	40·6	2·97	0·21	0·24	0·015	0·003	0·38	0·019	0·66	1·91	0·012
NFL1327	41·1	0·02	0·84	0·41	13·27	0·24	42·4	2·18	0·12	0·3	0·007	0·002	0·036	0·004	0·65	2·05	0·007
NTB1122	44·1	0·2	2·89	0·53	9·68	0·17	38·9	3·38	0·17	0·25	0·019	0·006	0·026	0·009	0·55	1·92	0·011
NFK1108	42·3	0·03	0·96	0·38	10·12	0·17	44·6	1·43	0·07	0·31	0·003	0·001	0·013	0·001	0·18	0·57	0·005
NFK1115	42·2	0·01	0·51	0·48	10·37	0·19	44·7	0·97	0·05	0·35	0·003	0	0·011	0·001	0·27	0·88	0·003
NFR0306	40·2	0·05	1·13	0·7	13·05	0·23	42·3	1·96	0·12	0·29	0·006	0·001	0·016	0·002	0·32	1·08	0·004
NFR0307	41	0·05	2·04	0·75	11	0·21	41·8	2·37	0·08	0·27	0·016	0·008	0·011	0·002	0·12	0·38	0·008
NFR1109	43·1	0·03	0·62	0·38	12·92	0·25	41·6	1·23	0·08	0·26	0·005	0·001	0·011	0·001	0·25	0·85	0·004
NMC1309	42·5	0·03	2·03	0·5	10·03	0·17	41·8	3·09	0·17	0·33	0·005	0·002	0·013	0·002	0·29	0·83	0·007
NMM0318	44·6	0·06	2·84	0·38	9·23	0·16	39·5	2·96	0·18	0·28	0·065	0·018	0·031	0·002	0·83	2·44	0·013

(continued)

Downloaded from https://academic.oup.com/petrology/article/58/6/1107/4001466 by ETH Zurich user on 30 June 2022

Table 4: Continued

Sample	Sr	Pr	Nd	Hf	Zr	Sm	Eu	Gd	Tb	Ti	Dy	Ho	Er	Tm	Yb	Lu	ΣREE
Group IA																	
NMS1308	5·74	0·065	0·38	0·13	4·4	0·14	0·057	0·2	0·036	373	0·26	0·057	0·17	0·025	0·17	0·027	2·05
NMS1310	8·27	0·078	0·46	0·14	4·3	0·19	0·078	0·29	0·055	644	0·41	0·099	0·31	0·049	0·36	0·059	2·96
NJS1307	9·6	0·1	0·62	0·19	6·28	0·24	0·097	0·36	0·064	767	0·48	0·11	0·32	0·048	0·35	0·053	3·51
NPY1301	4·73	0·043	0·26	0·09	2·89	0·1	0·044	0·16	0·03	381	0·23	0·053	0·16	0·025	0·19	0·029	1·64
NPY1314	8·55	0·12	0·78	0·23	7·64	0·34	0·13	0·51	0·096	905	0·7	0·16	0·48	0·073	0·51	0·073	4·86
NFL1329	5·55	0·07	0·4	0·13	3·69	0·16	0·069	0·24	0·044	300	0·33	0·075	0·22	0·031	0·23	0·034	2·41
NTB0307	5·8	0·066	0·36	0·074	1·81	0·14	0·059	0·21	0·041	283	0·32	0·072	0·21	0·031	0·22	0·031	2·30
NTB1124	5·82	0·056	0·35	0·11	2·67	0·15	0·064	0·24	0·044	695	0·34	0·077	0·23	0·035	0·24	0·035	2·27
NTB1116	6·47	0·061	0·36	0·097	2·91	0·14	0·057	0·2	0·039	347	0·29	0·069	0·19	0·03	0·21	0·03	2·08
NMC1336A	3·38	0·045	0·33	0·11	2·87	0·15	0·062	0·24	0·045	451	0·34	0·076	0·23	0·031	0·22	0·033	2·01
NMM1126	2·69	0·025	0·16	0·034	0·77	0·068	0·031	0·13	0·026	290	0·23	0·056	0·18	0·029	0·22	0·033	1·38
NME1116	7·07	0·059	0·32	0·061	2·31	0·11	0·045	0·17	0·031	300	0·25	0·058	0·18	0·027	0·2	0·032	1·87
NBN0302A	2·77	0·038	0·23	0·08	2·4	0·091	0·036	0·13	0·023	201	0·16	0·035	0·11	0·016	0·12	0·018	1·27
NBN0311	6·29	0·065	0·39	0·11	3·4	0·16	0·066	0·23	0·044	334	0·32	0·066	0·21	0·029	0·2	0·031	2·29
NBN0316	1·73	0·04	0·26	0·073	1·94	0·1	0·043	0·14	0·027	169	0·19	0·041	0·12	0·017	0·12	0·018	1·39
NBN0319	2·84	0·062	0·35	0·094	2·34	0·14	0·055	0·19	0·032	207	0·24	0·044	0·15	0·02	0·15	0·023	1·86
NBN0321	5·41	0·065	0·4	0·12	3·15	0·19	0·077	0·3	0·053	536	0·36	0·073	0·21	0·028	0·19	0·029	2·40
Group IB																	
NMS1302A	1·85	0·028	0·14	0·014	0·44	0·03	0·011	0·03	0·005	25·1	0·032	0·006	0·019	0·003	0·021	0·004	0·56
NMS1304	10·7	0·095	0·44	0·065	1·73	0·11	0·038	0·12	0·019	233	0·13	0·026	0·068	0·01	0·072	0·011	2·02
NMS1305	9·14	0·21	0·94	0·21	10·3	0·23	0·083	0·26	0·045	270	0·34	0·081	0·24	0·037	0·27	0·043	4·55
NFL1302	4·21	0·06	0·29	0·076	2·27	0·11	0·044	0·16	0·031	278	0·24	0·056	0·17	0·024	0·18	0·027	2·00
NFL1305	6·75	0·13	0·51	0·12	5·45	0·13	0·048	0·18	0·033	173	0·27	0·068	0·21	0·032	0·24	0·037	3·24
NFL1315A	4·3	0·092	0·43	0·12	4·09	0·094	0·032	0·09	0·014	63·2	0·088	0·018	0·052	0·007	0·053	0·009	1·72
NFL1316	2·95	0·031	0·15	0·042	1·53	0·04	0·015	0·042	0·007	83·2	0·043	0·009	0·03	0·004	0·038	0·006	0·78
NFL1324	15	0·45	1·99	0·27	12·6	0·39	0·12	0·36	0·051	312	0·33	0·069	0·2	0·029	0·2	0·031	8·26
NTB0306	7·54	0·037	0·11	0·012	0·22	0·034	0·016	0·06	0·011	115	0·09	0·021	0·065	0·01	0·07	0·011	1·42
NFK0301	8·51	0·28	1·15	0·051	2·87	0·22	0·075	0·2	0·03	189	0·21	0·044	0·13	0·021	0·15	0·024	5·28
NFK1123	5·77	0·23	0·83	0·048	1·88	0·12	0·035	0·12	0·018	275	0·13	0·028	0·085	0·013	0·1	0·016	4·40
NFR0309	5·71	0·12	0·61	0·17	5·81	0·23	0·095	0·34	0·064	702	0·49	0·11	0·32	0·046	0·33	0·051	4·00
NFR1107	7·59	0·076	0·42	0·083	2·74	0·12	0·048	0·15	0·026	236	0·18	0·041	0·11	0·017	0·11	0·016	1·82
NMC1301	9·44	0·2	0·77	0·081	4·47	0·12	0·041	0·093	0·015	68·9	0·093	0·02	0·055	0·008	0·056	0·008	3·45
NMC1322	4·16	0·083	0·4	0·038	1·13	0·1	0·034	0·13	0·024	160	0·2	0·047	0·15	0·023	0·17	0·025	2·13
NMM1115	2·76	0·029	0·19	0·053	1·81	0·073	0·03	0·11	0·021	191	0·15	0·036	0·11	0·017	0·11	0·018	1·13
NME1122	4·99	0·055	0·28	0·065	1·91	0·11	0·044	0·15	0·026	343	0·19	0·039	0·11	0·017	0·12	0·018	1·86
NME0528	6·44	0·12	0·52	0·09	3·75	0·13	0·045	0·13	0·022	147	0·15	0·032	0·088	0·013	0·093	0·013	2·39
NBN0305	5·65	0·042	0·22	0·036	0·73	0·07	0·023	0·081	0·014	126	0·091	0·019	0·061	0·009	0·067	0·01	1·05
Group IIA																	
NJS1302	5·47	0·23	1·35	0·46	17·7	0·44	0·15	0·53	0·088	1120	0·61	0·13	0·36	0·052	0·37	0·052	5·67
NJS1304	2·87	0·11	0·59	0·2	8·06	0·17	0·061	0·21	0·034	633	0·24	0·052	0·16	0·024	0·18	0·026	2·47
NJS1306	11·9	0·16	0·89	0·23	7·32	0·32	0·14	0·45	0·081	701	0·59	0·13	0·38	0·052	0·38	0·055	4·97
NPY1310	7·24	0·12	0·69	0·16	3·58	0·28	0·11	0·44	0·084	776	0·61	0·14	0·38	0·056	0·39	0·06	4·18
NPY1311	7·62	0·13	0·73	0·16	3·67	0·29	0·12	0·47	0·088	822	0·66	0·15	0·44	0·063	0·45	0·066	4·54
Group IIB																	
NFL1326	16·7	0·3	1·43	0·17	5·07	0·37	0·13	0·4	0·062	521	0·43	0·087	0·24	0·035	0·24	0·032	6·32
NFL1327	11·9	0·33	1·54	0·042	2·88	0·34	0·12	0·29	0·043	152	0·26	0·052	0·15	0·021	0·15	0·021	6·01
NTB1122	10·3	0·35	1·88	0·24	7·06	0·54	0·18	0·6	0·096	1232	0·65	0·13	0·39	0·055	0·38	0·056	7·78
NFK1108	5·3	0·091	0·43	0·053	1·63	0·11	0·046	0·14	0·025	192	0·17	0·037	0·11	0·016	0·12	0·017	2·06
NFK1115	6·93	0·14	0·65	0·06	3·31	0·14	0·043	0·12	0·017	25·5	0·1	0·022	0·061	0·01	0·071	0·01	2·53
NFR0306	7·58	0·16	0·74	0·093	2·61	0·19	0·076	0·22	0·036	245	0·25	0·053	0·16	0·023	0·16	0·023	3·49
NFR0307	4·29	0·055	0·26	0·047	1·26	0·068	0·026	0·091	0·018	277	0·14	0·034	0·11	0·016	0·12	0·018	1·47
NFR1109	6·71	0·12	0·57	0·031	1·4	0·13	0·049	0·13	0·019	124	0·12	0·024	0·069	0·011	0·083	0·013	2·43
NMC1309	8·04	0·12	0·52	0·068	2·21	0·15	0·065	0·21	0·042	220	0·31	0·071	0·22	0·033	0·23	0·034	3·13
NMM0318	11·4	0·37	1·65	0·18	7·58	0·39	0·15	0·42	0·071	405	0·49	0·11	0·32	0·046	0·33	0·05	7·66

Trace element concentrations for orthopyroxene, olivine and spinel were calculated using the analyzed clinopyroxene compositions and partition coefficients taken from Hart & Dunn (1993) and Ionov *et al.* (2002) and references therein.

Downloaded from https://academic.oup.com/petrology/article/58/6/1107/4001466 by ETH Zurich user on 30 June 2022

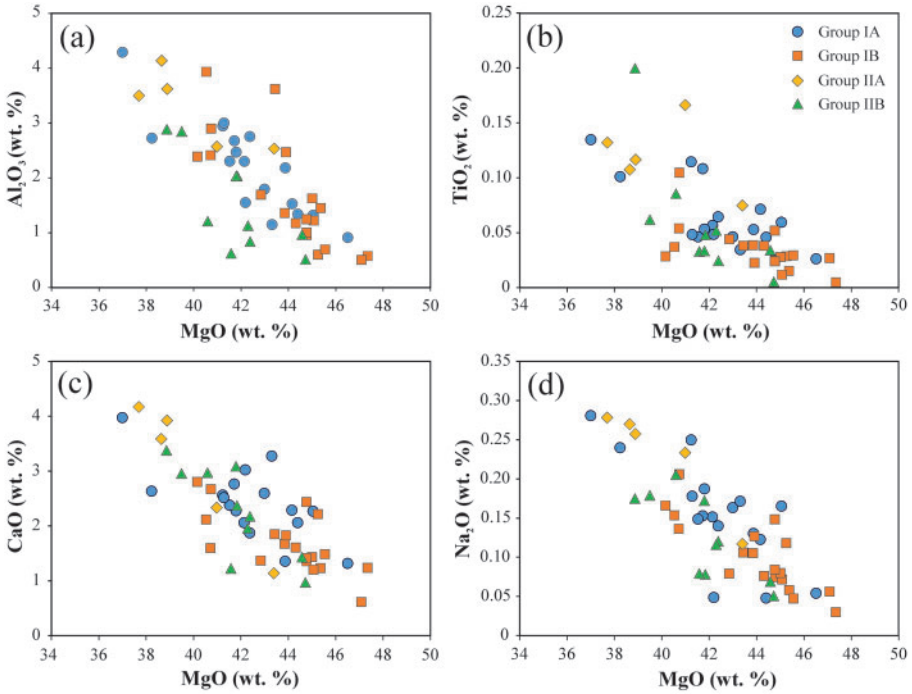

Fig. 8. Whole-rock MgO compositions of the studied NGVF xenoliths compared with (a) Al_2O_3, (b) TiO_2, (c) CaO and (d) Na_2O. Symbols are as in Fig. 4. Whole-rock compositions were calculated via mass balance from modal and analyzed major element compositions of mineral constituents (Table 4).

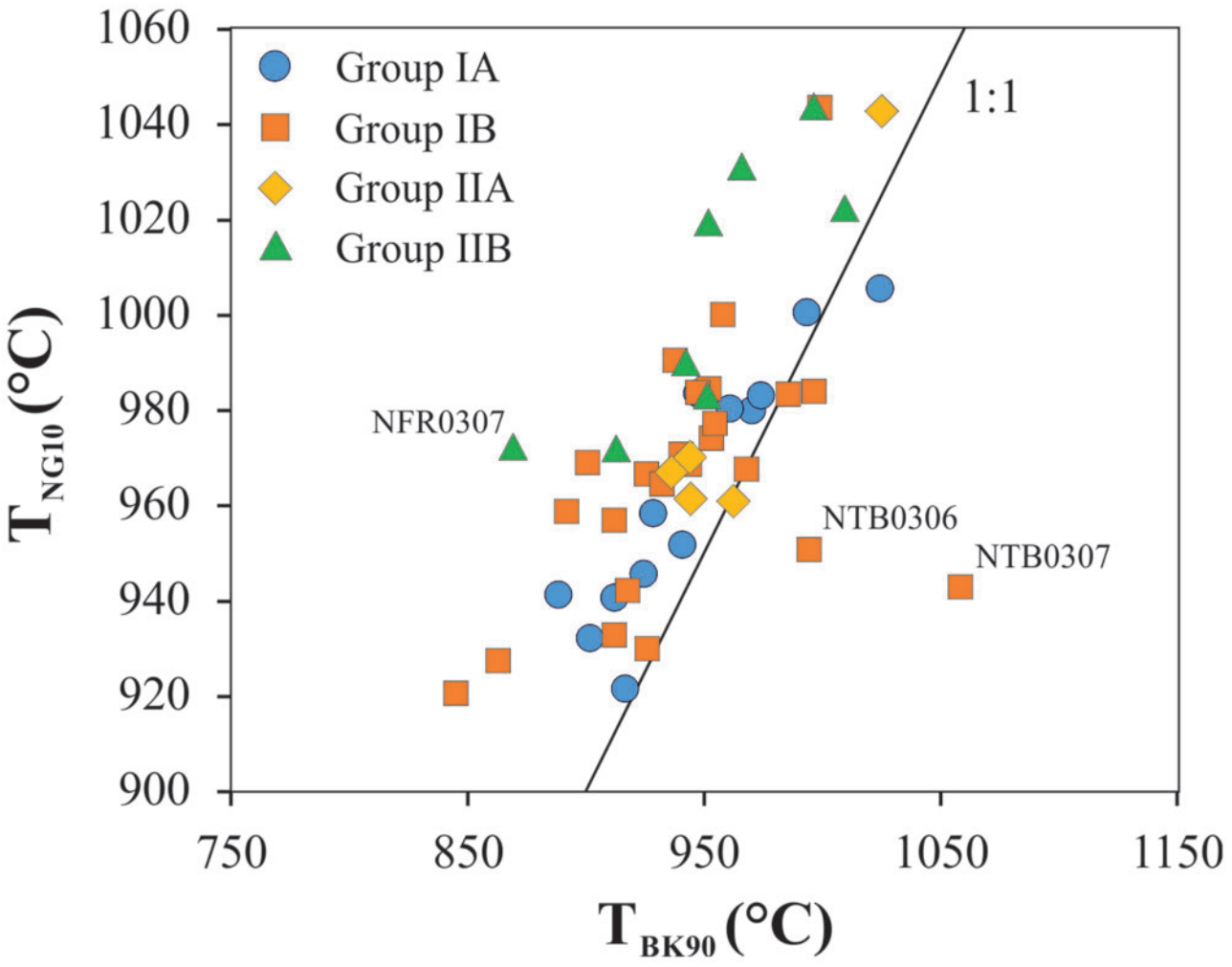

Fig. 9. Comparison of equilibration temperatures of the studied NGVF xenoliths, calculated using two major element-based thermometers: TBK90, two-pyroxene method of Brey & Köhler (1990); NG10, Ca-in-opx method of Brey & Köhler (1990) modified by Nimis & Grütter (2010).

Downloaded from https://academic.oup.com/petrology/article/58/6/1107/4001466 by ETH Zurich user on 30 June 2022

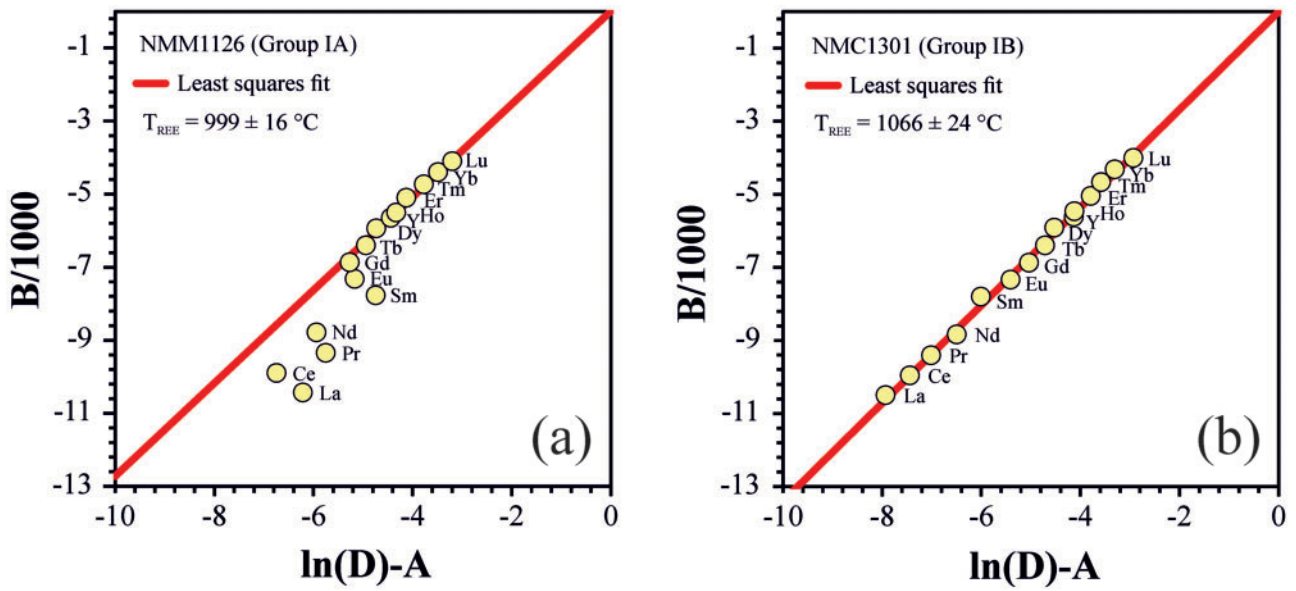

Fig. 10. Inversion diagram for calculation of equilibrium *T* using the thermometer of Liang *et al.* (2013), based on the temperature dependence of REE partitioning between ortho- and clinopyroxene. The calculation is based on the equation $\ln D_i^{opx/cpx} = A_i + B_i/T$, where A_i and B_i are coefficients determined by pyroxene compositions and ionic radii for elements *i*. In the inversion diagram, the slope of the linear regression is correlated with the temperature; in the case of ideal pyroxene equilibrium, LREE and HREE fall on the same line. (a) Representative inversion diagram for a sample with apparent pyroxene disequilibrium in LREE owing to low concentrations in opx (NMM1126, Group IA). (b) Representative inversion diagram of a sample with LREE-equilibrated pyroxenes (NMC1301, Group IB).

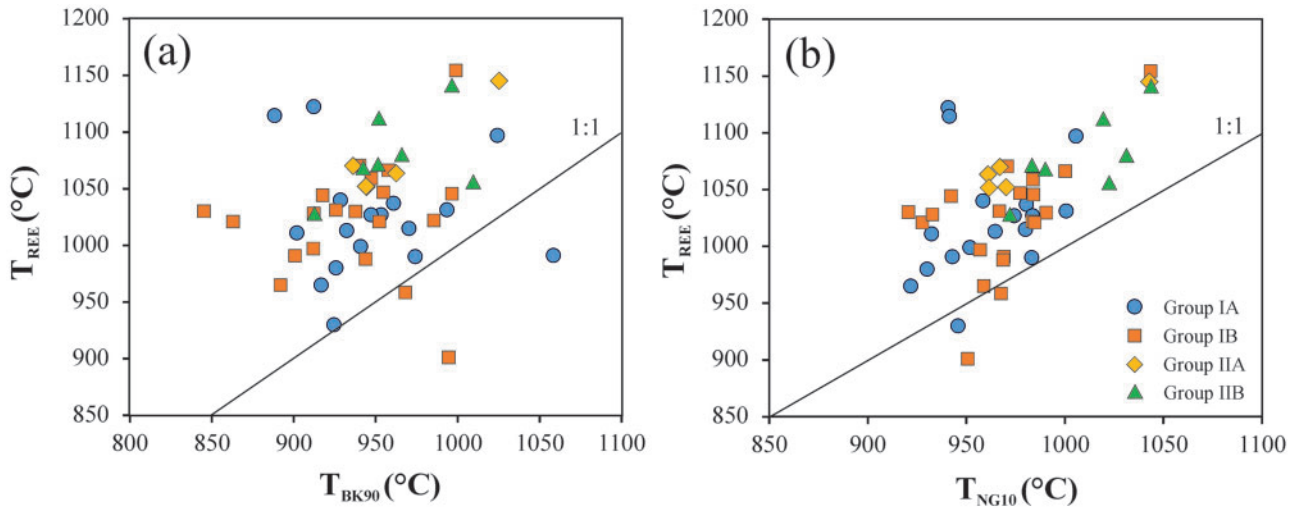

Fig. 11. Comparison of equilibration temperatures calculated with the REE thermometer (Liang *et al.*, 2013) and major element-based thermometers: (a) two-pyroxene method of Brey & Köhler (1990); (b) Ca-in-opx method as revisited by Nimis & Grütter (2010).

reliability of the calculated concentrations is verified by good correlations between analyzed and calculated HREE contents of orthopyroxene ($R^2 = 0{\cdot}85$ for Lu; not shown).

Whole-rock REE contents correlate well with clinopyroxene analyses (Table 3). Total REE contents vary between 0·557 and 8·26 ppm in Group IB. Xenoliths of Group IA show a narrow range (1·27–3·51 ppm) in total REE, whereas Groups IIA and B (2·47–5·67 and 1·47–7·78 ppm) both have significantly higher REE contents. The xenoliths with the most depleted HREE (Yb < 0·1 ppm, Lu < 0·015; Table 4) mostly are those with the most depleted major element characteristics (highest spinel Cr#; Fig. 4a, Table 2).

GEOTHERMOMETRY

The fact that there is no major geochemical variation within grains (see Supplementary Data for individual analyses), or between grains in the same sample, allows us to assume that the coexisting minerals are in equilibrium. We therefore calculated equilibration

Downloaded from https://academic.oup.com/petrology/article/58/6/1107/4001466 by ETH Zurich user on 30 June 2022

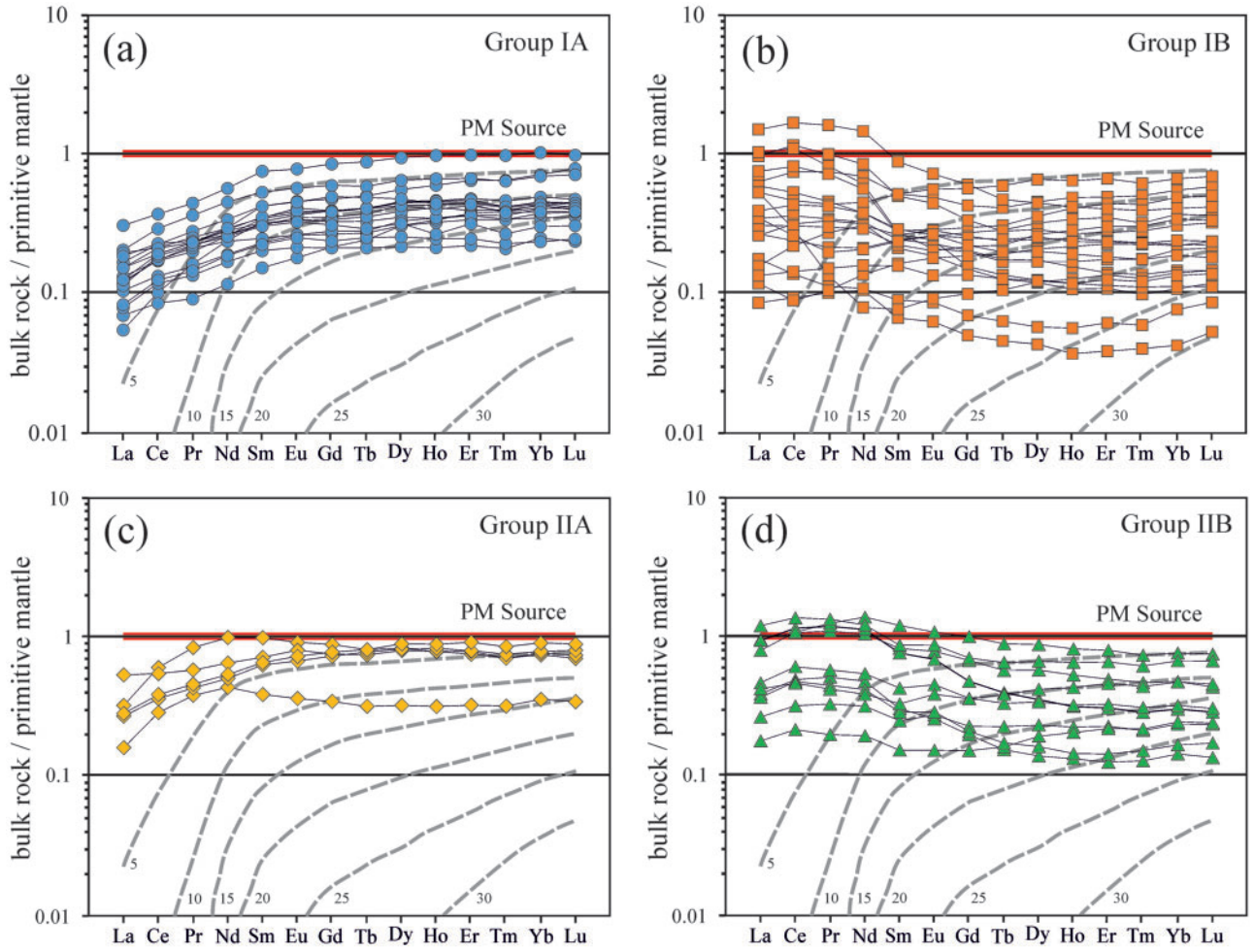

Fig. 12. Fractional melting model for xenoliths of Group IA, IB, IIA, IIB (a–d, respectively). Fractional melting curves and PM source are taken from Niu (2004) and references therein. Whole-rock REE have been calculated by mass balance, using analyzed data for pyroxenes and concentrations for olivine and spinel calculated with the use of mineral/melt partition coefficients taken from Hart & Dunn (1993) and Ionov *et al.* (2002) (Table 4).

temperatures using several methods: the two-pyroxene methods of Brey & Köhler (1990) ($\sigma = 15°C$) and Taylor (1998) ($\sigma = 31°C$), as well as the Ca-in-opx thermometer of Brey & Köhler (1990) as modified by Nimis & Grütter (2010) ($\sigma = 36°C$ for temperatures between 900 and 1200°C). The resulting temperatures are in the range of 845–1058, 829–1012, and 921–1044°C, respectively (Table 1), consistent with the estimates of Szabó & Taylor (1994). Xenoliths from the southern part, regardless of their texture, have lower equilibration temperatures than those from the central part (Table 1). Temperatures obtained with the two-pyroxene method of Brey & Köhler (1990) are plotted against the Ca-in-opx method modified by Nimis & Grütter (2010) in Fig. 9. The linear correlation generally supports equilibrium, with a few exceptions (NTB0306, NTB0307, and NFR0307; Table 1), where significant differences between the temperatures suggest a lack of chemical equilibrium between ortho- and clinopyroxene (Table 1).

To further evaluate the temperatures obtained from major element thermometers, the trace element thermometer developed by Liang *et al.* (2013) was also applied. This is based on the temperature dependence of REE and Y exchange between ortho- and clinopyroxene, provided they are in equilibrium. In samples in which orthopyroxene has low LREE contents, linear regressions of only HREE were considered because of analytical uncertainties on LREE (an example is shown in Fig. 10a). In the case of xenoliths with high LREE concentrations (i.e. the most enriched samples of Group IB and IIB), these elements could be taken into account and the good correlation verifies that the pyroxenes of the metasomatized xenoliths are in equilibrium (Fig. 10b). Thus the standard deviation could be reduced for the individual xenoliths (1–59°C; see Table 1 for each sample).

REE temperatures of the studied NGVF xenoliths (Table 1) range from 930 to 1154°C, except for NTB0306, which yields 901°C, but this xenolith already indicated pyroxene disequilibrium in calculations with major element based thermometers (Fig. 9). For the rest of the samples, REE temperatures are higher by an average of 100°C compared with the temperatures from

Downloaded from https://academic.oup.com/petrology/article/58/6/1107/4001466 by ETH Zurich user on 30 June 2022

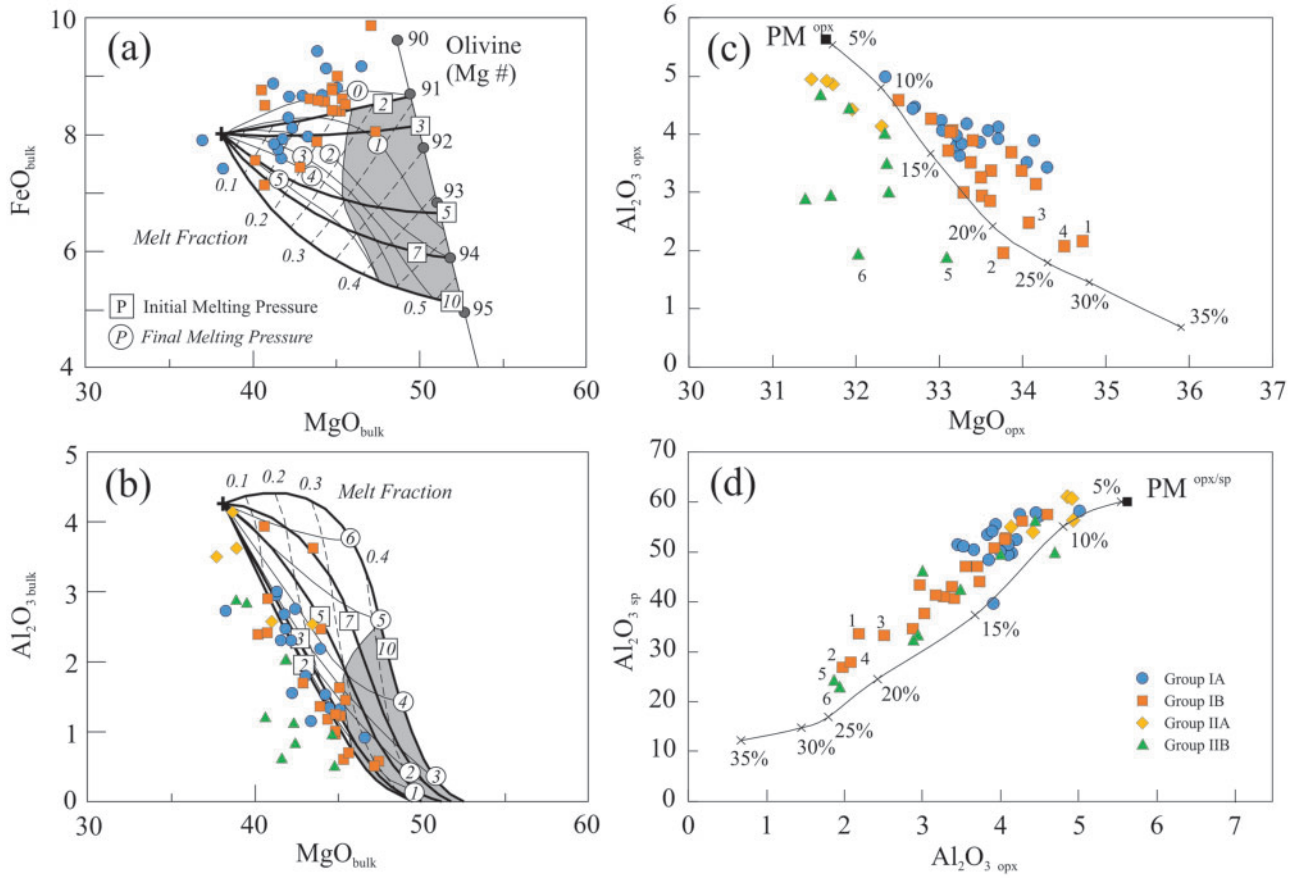

Fig. 13. (a, b) Fractional-melting model for the studied xenoliths in diagrams of MgO vs FeO and Al_2O_3, using the melt fraction and initial and final pressure curves (in GPa) of Herzberg (2004). Melting source is a fertile peridotite taken from Walter (1998). Light gray field represents the composition of a residual harzburgite. Lines with numbers 90–95 (a) stand for Mg# of olivine. In (a), only Group IA and IB are plotted owing to the high Fe contents of Group IIA and IIB. (c, d) Melting curves for MgO vs Al_2O_3 in opx and Al_2O_3 in opx vs spinel (Upton *et al.*, 2011; Faccini *et al.*, 2013). Primitive mantle opx and spinel compositions (black squares) were calculated by mass balance using the major element and modal compositions of McDonough & Sun (1995) for the spinel stability field. Labelled xenoliths: 1, NMS1302A; 2, NFL1315A; 3, NFL1316; 4, NTB0306; 5, NFK1115; 6, NFR1109.

the method of Brey & Köhler (1990) (Fig. 11a), and by an average of 50°C compared with the Ca-in-opx method of Nimis & Grütter (2010) (Fig. 11b). This discrepancy was observed previously in abyssal peridotites and mafic cumulates (Liang *et al.*, 2013) and is thought to be the result of different cooling rates, as discussed below. Furthermore, it is noteworthy that Group IIB xenoliths show higher temperatures with both the Ca-in-opx and the REE thermometer compared with the other groups (Fig. 11b).

DISCUSSION

Thermal history and equilibration

The presence of melts in the mantle, indicated by melt pockets in some xenoliths (Table 1), can have an effect on the calculated temperatures. Formation of melt pockets may be explained by several processes: reaction of peridotite xenolith and host basalt during ascent, melting of anhydrous phases (e.g. Huebner & Turnock, 1980), breakdown of hydrous phases as a result of increasing temperature prior to ascent (e.g. Stosch & Seck, 1980), or reaction with a migrating silicate melt in the mantle (Bali *et al.*, 2002, 2008). In the NGVF xenoliths, the large size of the melt pockets and the lack of definite connection between them (Fig. 3c and f) suggests *in situ* melting at depth, because ascent of the host magma was relatively rapid (i.e. ~36 h to the Moho and an additional ~1·5 h to the surface; Szabó & Bodnar, 1996). The fact that the pyroxenes of xenoliths from the southern part, which contain the most melt pockets (Table 1), are depleted in incompatible elements (Table 3) and the lack of any visible sign of melt percolation also argue against melt–wall-rock reaction. On the other hand, the presence of melt pockets can bring into question the validity of the equilibration temperatures calculated with major element-based thermometers, as the two-pyroxene and Ca-in-opx methods rely on the Ca contents of pyroxenes, and part of the Ca most probably went into the melt pockets as it became incompatible at elevated temperatures (e.g. Witt & Seck, 1987). Furthermore, temperature values below

Downloaded from https://academic.oup.com/petrology/article/58/6/1107/4001466 by ETH Zurich user on 30 June 2022

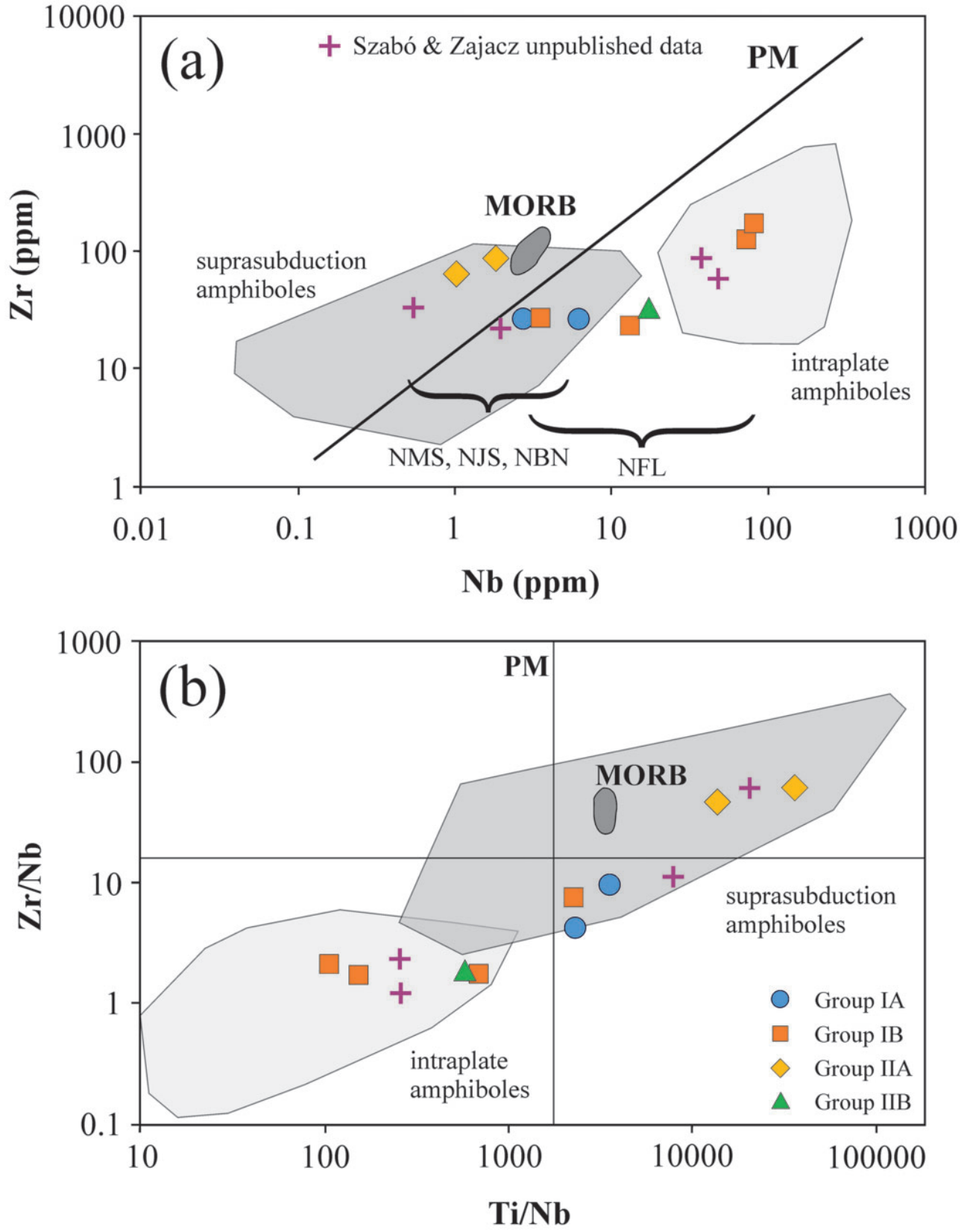

Fig. 14. Nb vs Zr (a) and Ti/Nb vs Zr/Nb (b) for amphiboles in the studied xenoliths and several previously unpublished analyses from the NGVF (+ signs). Fields for suprasubduction and intraplate origins are from Coltorti *et al.* (2007*a*). PM values are from McDonough & Sun (1995). Abbreviations of sampling sites in (a) are as in Fig. 1b.

Downloaded from https://academic.oup.com/petrology/article/58/6/1107/4001466 by ETH Zurich user on 30 June 2022

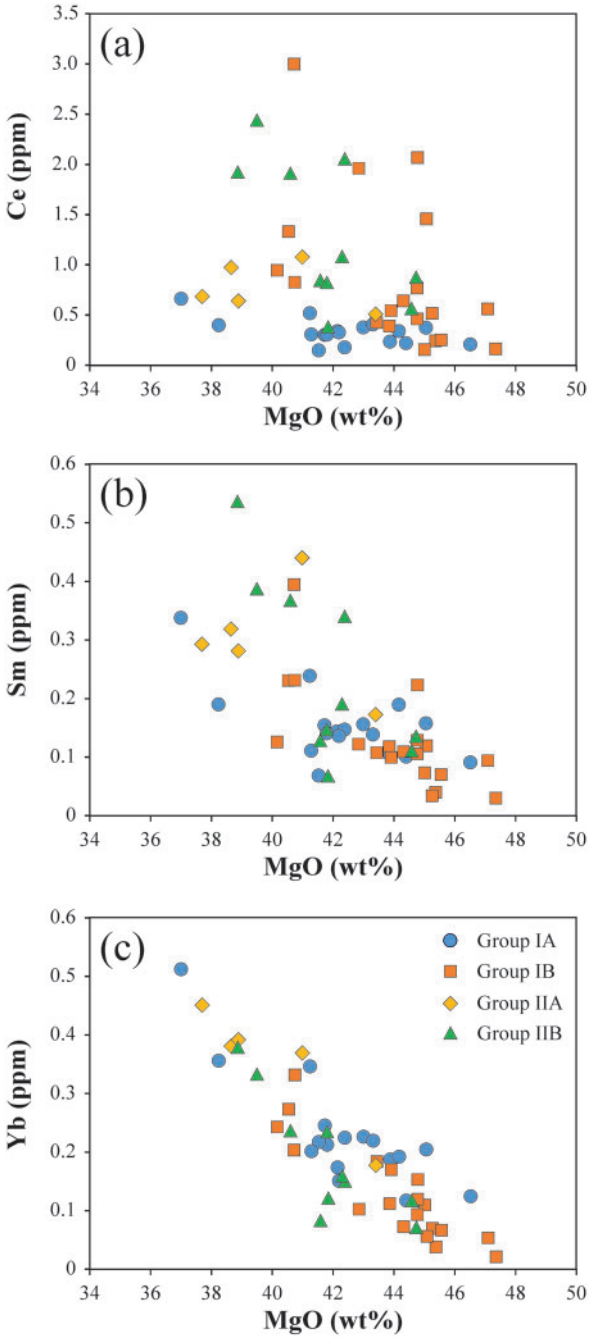

Fig. 15. Whole-rock MgO vs Ce (a), Sm (b) and Yb (c) for the NGVF xenoliths. Whole-rock MgO was calculated via mass balance from modal and analyzed major element compositions. Whole-rock REE were calculated by mass balance, using analyzed data for pyroxenes and concentrations for olivine and spinel calculated using mineral/melt partition coefficients from Hart & Dunn (1993) and Ionov *et al.* (2002). Calculated whole-rock concentrations are reported in Table 4.

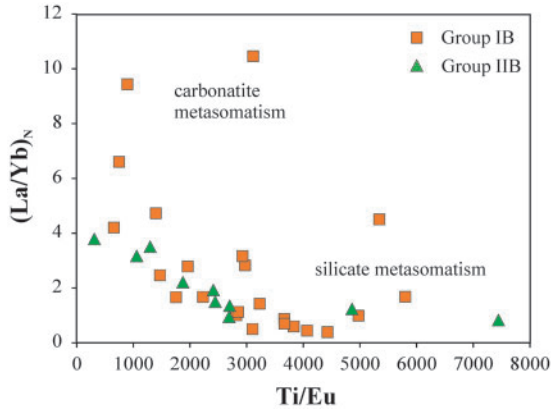

Fig. 16. $(La/Yb)_N$ vs Ti/Eu in clinopyroxenes of Group IB and IIB xenoliths, which show imprints of cryptic metasomatism. Areas of silicate and carbonatite metasomatism are from Coltorti *et al.* (1999).

900°C are slightly below the values previously reported from the CPR (i.e. Bali *et al.*, 2002). Therefore, equilibration temperatures calculated with thermometers based on major element exchange probably should be considered as minimum values.

REE distribution in pyroxenes can provide further insights. For the continental upper lithospheric mantle, which is thermally well equilibrated and did not undergo variations in temperature before sampling by the host magma, major element and REE thermometers are expected to be in agreement. However, the diffusion rate of the trivalent REE is slower than that of the divalent cations in mantle silicates (van Orman *et al.*, 2001; Cherniak & Liang, 2007), and for a high cooling rate, the closure temperature for REE will be higher than for the major elements. Therefore the REE-based thermometer will give sub-solidus temperatures, whereas major element-based thermometers provide the temperature of the latest thermal equilibration (Liang *et al.*, 2013). A discrepancy between the two values is characteristic of abyssal peridotites (e.g. Marchesi *et al.*, 2016), as cooling rates in the lower oceanic crust are around 10^{-1}–10^{-5}°C a^{-1} (Coogan *et al.*, 2002; VanTongeren *et al.*, 2008), in contrast to xenoliths from the continental mantle, which are assumed to have equilibrated over long periods of geological time.

In the NGVF xenoliths, there is an average difference of ~50–100°C between temperature values (Table 1) calculated with REE and major element-based thermometers. This suggests that major thermal changes have affected the upper mantle prior to the entrainment of the xenoliths in the host basalt. REE distributions in pyroxenes record a higher-temperature environment, followed by cooling and late-stage re-equilibration, indicated by the major element thermometers. This cooling event beneath the CPR is supported by studies on mantle xenoliths from LHPVF, BBHVF and PMVF (Fig. 1a). Embey-Isztin *et al.* (2001) and Falus *et al.* (2008) detected a cooling defined by compositional differences between the cores and rims of porphyroclasts, and Falus *et al.* (2007) reported temperature differences based on exsolution lamellae in pyroxenes. The estimated extent of cooling is ~40–50°C in the PMVF (Falus *et al.*, 2008) and ~100–150°C in the LHPVF (Falus *et al.*, 2007). These rates are consistent with the temperature gap detected in the NGVF xenoliths, and thus support the record of thermal evolution in the CPR.

Downloaded from https://academic.oup.com/petrology/article/58/6/1107/4001466 by ETH Zurich user on 30 June 2022

In the NGVF, higher temperatures could also have induced the melting of amphibole, which has a solidus of ~1050–1100°C, depending on the composition and H_2O content of the peridotite (Green *et al.*, 2010), over a wide range of pressures (equivalent to ~30–90 km; Niida & Green, 1999). Amphibole breakdown could explain the melt pockets, which appear most frequently in xenoliths from the southern part (Table 1). This is also consistent with earlier observations on the modal abundance of amphibole from the southern part (Szabó & Taylor, 1994), despite its absence in the present sample set. Furthermore, heating induced by extension and asthenosphere upwelling in the Pannonian Basin (Horváth, 1993; Csontos, 1995) could have affected the southern part more than the northern and central parts because it is closer to the center of the extensional basin (Fig. 1). In xenoliths from the central part (except for the Fil'akovo-Kerčik locality), the rarity of amphibole may relate to lower initial abundance, or an additional heating factor, such as melts ascending from greater depths.

Partial melting

Partial melting can be traced in the NGVF xenoliths as either (or both) a change in major element compositions, such as an increase in the Cr-number of spinel (Arai, 1994), and/or LREE depletion. These attributes have been described in peridotite massifs (e.g. Bodinier *et al.*, 1988) and alkali basalt-hosted mantle xenoliths (e.g. Frey & Green, 1974; Downes *et al.*, 1992), and are interpreted as reflecting partial melting of an originally fertile mantle by extraction of basaltic melt (e.g. Frey & Prinz, 1978). However, LREE-poor compositions can also be a result of metasomatic reaction with a large fraction of basaltic melt (e.g. Van der Wal & Bodinier, 1996; Bedini *et al.*, 1997; Le Roux *et al.*, 2007).

A common trend towards moderate depletion can be observed in some NGVF xenoliths in Fig. 4a, and the estimated degree of partial melting is around 20%. To achieve more precise values of the degree of melting, several melting models can be used based on whole-rock major element contents (Walter, 2003; Herzberg, 2004), HREE (Niu, 2004) or Cr-number of spinel in equilibrium with clinopyroxene (Hellebrand *et al.*, 2001). The HREE display a wide range in clinopyroxenes (e.g. Yb = 0·31–2·58 ppm; Table 3) and in bulk-rock as well (Yb = 0·02–0·51 ppm; Table 4), and there is some variability in each of the four xenolith groups. The degree of partial melting compared with a PM source (Sun & McDonough, 1989) has been estimated using the melting curves of Niu (2004) for bulk-rock fractional modelling. Model parameters and distribution coefficients for this model have been summarized by Niu & Hékinian (1997). Because of the sensitivity of the LREE to metasomatic events, only HREE were used to determine the amounts of melt extraction. The xenoliths generally display a wide range of HREE contents (Fig. 12a–d). Group IA and IIA show partial melting degrees of ~5–20% (except for NPY1314, which has a PM composition) and <5–15%, respectively (Fig. 12a and c). Group IB and IIB, however, display a wider range of partial melting (~5–30% and 5–25%, respectively; Fig. 12b and d). The high variability in melting degree in all groups suggests that partial melting has affected the mantle volumes represented by the xenoliths independently of their classification or locality, and therefore is likely to have occurred before any metasomatic overprint. Xenoliths of Group IIA show the lowest amount of melt extraction (<5%), and therefore they represent the most fertile upper mantle domain in the NGVF (Fig. 4a–d). These geochemical features are characteristic of only Podrečany and Jelšovec in the northern part, as Group IIA xenoliths appear only here, and they make up the majority of xenoliths from these two locations (Fig. 1b).

To constrain further the amount of melt extraction, the relationships of major elements in whole-rock compositions, as well as in individual phases, were examined. The bulk compositions of the NGVF xenoliths were plotted on the fractional melting and pressure grids of Herzberg (2004) (Fig. 13a and b). The source material for this melting model was a fertile peridotite described by Walter (1998), which was obtained by extracting 1% mid-ocean ridge basalt (MORB) melt from the PM (McDonough & Sun, 1995). The FeO content of the NGVF xenoliths spreads over a wide range and because of their high FeO concentrations (8·74–13·27 wt %; Table 1) Group II xenoliths are not plotted in Fig. 13a. Group IA and IB xenoliths show no correlation between MgO and FeO, and higher FeO often accompanies higher MgO, so that the Mg# of these xenoliths does not fall below 'average' values (89–90). This feature is characteristic of the mantle of the NGVF. However, most of the samples falling on the grid plot around or on the dashed lines representing 0·1–0·2 (0·3) melt extraction fractions, and the initial melting pressures (bold lines) tend to be higher than the final pressures (fine lines). Group II xenoliths are plotted on the grids based on MgO vs Al_2O_3 (Fig. 13b). Group IIB xenoliths fall consistently towards lower MgO contents compared with Group I xenoliths (as also shown on Fig. 8a), as a result of enrichment of Fe at the expense of Mg (as shown by Mg# values; Fig. 4a–c, Table 2). Group IA and IB plot consistently between 0·1 and 0·3 melt extraction fraction, with initial melting pressures of 2–3 GPa on average and final melting pressures usually at or below 2 GPa. Several xenoliths plot above the grids (Fig. 13c) because of high (>45 wt %) bulk SiO_2 contents. This can be explained by a high pyroxene mode; for example, large orthopyroxene porphyroclasts in a small xenolith, which is true for several NGVF samples (Table 1). The highest degree of partial melting is recorded in Group IB xenoliths, consistent with the model of Niu (2004), where the lowest HREE contents occur in Group IB and indicate up to 30% partial melting (Fig. 12b). However, such high degrees of melt extraction are not consistent with the Mg-numbers and the relatively high amount of clinopyroxene in the xenoliths, as clinopyroxene would

Downloaded from https://academic.oup.com/petrology/article/58/6/1107/4001466 by ETH Zurich user on 30 June 2022

be no longer present under these conditions (marked by the grey field in Fig. 13a and b). To avoid possible errors caused by uncertainties in the modal composition, empirical melting curves based on the major element contents of orthopyroxene (Upton *et al.*, 2011; Faccini *et al.*, 2013) were also applied. MgO vs Al_2O_3 in orthopyroxene (Fig. 13c) shows a good correlation for Group I xenoliths, with melting degrees ranging between ~9–20% for Group IA and ~11–26% for Group IB. Group II xenoliths shift towards lower MgO values with increased FeO contents (as discussed above), but the difference in the degree of melt extraction is well defined (~7–12% for Group IIA and ~8–20% for IIB). The distinct groups generally show similar ranges in the plot of Al_2O_3 in orthopyroxene vs spinel (Fig. 13d); Group IA shows a slightly narrower range (~8–14%) and the Group IIB maximum rises to ~23%. The xenoliths with the highest degrees of melting (NMS1302A, NFL1315A, NFL1316, NTB0306, NFK1115, NFR1109) correspond to those with the highest spinel Cr# in Fig. 4a.

In summary, whereas the degrees of melting calculated with methods based on REE and major elements are generally in agreement, the methods using calculated bulk-rock compositions have slightly higher uncertainty. Therefore we prefer the partial melting degrees based on the analyzed compositions of mineral phases, which suggest a maximum of ~23–25% of melt extraction, and a minimum of ~7–10% for the most fertile xenoliths. This implies that subsequent metasomatic events, on which the group classification is based, affected an already heterogeneously depleted mantle domain under the NGVF.

Imprints of metasomatic processes

Presence and absence of amphibole

The most common, but not exclusive, products of modal metasomatism are volatile-bearing phases such as amphibole and phlogopite. Pargasitic amphibole occurs widely in upper mantle peridotites, and is an important reservoir for volatiles and incompatible trace elements such as Rb, Ba and Nb (Ta). Experimental studies reveal that amphibole is stable up to 2·5–3·0 GPa at subsolidus conditions, and to temperatures of 950–1000°C at water-saturated and to 1025–1150°C at water-undersaturated conditions, depending on peridotite composition (e.g. Green, 1973; Mengel & Green, 1989; Wallace & Green, 1991; Niida & Green, 1999). NGVF xenoliths contain amphibole in several samples from the northern part and one location in the central part, and amphibole has been reported from the southern part by Szabó & Taylor (1994). They found the amphiboles to be homogeneously pargasitic in composition, regardless of sampling locality; this was verified by re-calculation using the spreadsheet of Locock (2014). Amphiboles analyzed in this study, however, were found to be mostly magnesio-hastingsitic in composition, using the same calculation method. As the main difference between these two sets of amphibole compositions is based on the ratio and distribution of

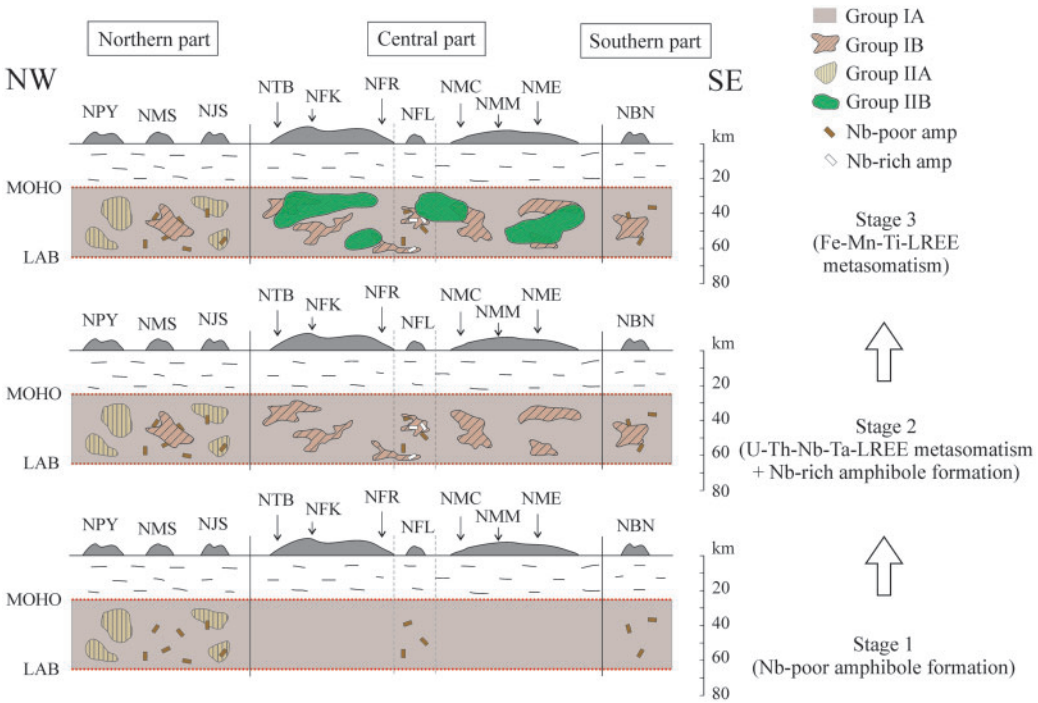

Fig. 17. Schematic illustration depicting the reconstruction of metasomatic events in the upper mantle of the NGVF. Stage 1, formation of Nb-poor amphibole via reaction with a subduction-related, volatile-rich melt; Stage 2, U–Th–LREE enrichment in clinopyroxenes and formation of Nb-rich amphiboles in the Fil'akovo-Kerčik locality; Stage 3, Fe–Mn–Ti–LREE enrichment in selective domains beneath the central part. Depth of Moho and LAB (lithosphere–asthenosphere boundary) in the NGVF are taken from Klébesz *et al.* (2015). (For abbreviations of the sampling sites see Fig. 1b.)

Downloaded from https://academic.oup.com/petrology/article/58/6/1107/4001466 by ETH Zurich user on 30 June 2022

Fe^{2+} and Fe^{3+}, which cannot be determined by microprobe analyses only, the calculation for the cations in each position heavily depends on the concentrations of other major elements in the amphibole. There are differences in SiO_2, Al_2O_3 and total abundances between this study and that of Szabó & Taylor (1994), where these values are higher by 1–2% on average. Thus, it is likely that the discrepancy in the classification is due to analytical differences.

Szabó & Taylor (1994) suggested that volatile-bearing minerals (amphibole and traces of phlogopite) are products of a reaction with a K_2O-rich, H_2O- (and possibly F-) bearing subduction-related silicate melt. The presence of such melts is supported by a study on melt inclusions in NGVF xenoliths by Szabó *et al.* (1996). However, amphibole can be precipitated from melts of different origins (Coltorti *et al.*, 2007*a*). Coltorti *et al.* reported compositional differences in HFSE such as Nb, Zr and Ti between amphiboles in suprasubduction and intraplate environments, which can be used to discriminate between amphiboles of different metasomatic origin. These compositional differences are based on the ratio of Nb to other HFSE, as Nb can be retained in the subducting slab and thus is in low concentrations in subduction-related melts (Foley *et al.*, 2000; Schmidt *et al.*, 2004); it can then reappear in intraplate magmas that may contain contributions from older subducted slabs (McDonough, 1991; Fitton, 1995; Rudnick *et al.*, 2000). Amphiboles in the NGVF xenoliths show a wide range of Nb contents (Table 3). The relationship between Nb and Zr (Fig. 14a) and ratios of Ti/Nb and Zr/Nb (Fig. 14b) were used to constrain the crystallization environment of the amphiboles in the studied xenoliths, along with unpublished data of Szabó & Zajacz from the NGVF (Mašková, Fil'akovo-Kerčik and Bárna). Group IA and IIA amphiboles (and NMS1304 of Group IB) have lower Nb contents and thus plot in the suprasubduction field, whereas most Group IB and IIB amphiboles plot in or next to the intraplate field because of their higher Nb contents. Because Group IA and IIA xenoliths are LREE-depleted, they are considered to have been unaffected by the metasomatic events that enriched LREE in Group IB and IIB. This suggests that amphiboles of the former group were independent of the LREE-enriching metasomatism, and they were originally formed via volatile-rich fluids or melts related to a subducting slab. Based on the REE patterns of Group IA and IIA amphiboles (Fig. 7b), this slab-related fluid or melt must have been depleted in LREE to be able to produce LREE-depleted amphibole. Such depleted amphiboles have been reported from the CPR previously, at the Kapfenstein locality in the Styrian Basin; however, there is clear petrographic evidence that these amphiboles grew at the expense of primary (LREE-enriched) clinopyroxene and spinel (Coltorti *et al.*, 2007*b*), or crystallized from the metasomatizing agent itself (Vaselli *et al.*, 1996).

As for amphiboles in Group IB and IIB xenoliths, their probable intraplate origin suggests the impact of melts generated later, during or after the formation of the Pannonian Basin. These amphiboles, including the two unpublished analyses, are all exclusively from the Fil'akovo-Kerčik locality (Fig. 1a; Table 1). They either were formed by intraplate, LREE-enriched melts that reacted with the rest of the rock-forming minerals, or formed originally in a suprasubduction environment, but were later metasomatized by intraplate melts. The latter is less likely because of the lack of any textural evidence of subsequent alteration, such as melting at the rims of the amphiboles. Therefore, it is proposed that amphiboles in Group IB and IIB were formed during reaction with a silicate melt of intraplate origin, and this mechanism was dominant at Fil'akovo-Kerčik, a locality slightly older than and spatially separated from the plateaux of the central part. The strong similarity in the REE patterns of clinopyroxene and amphibole suggests that this melt probably also caused cryptic metasomatism in the pyroxenes. In addition to the LREE, enrichment of Rb, Nb and Ta is also characteristic of intraplate amphiboles, as well as of Group IB and IIB clinopyroxenes (compared with Group IA and IIA; see Fig. 5 and Table 3), which suggests that the metasomatizing agent was also enriched in these elements.

In the studied sample set, amphibole is completely absent from localities on the two large basalt plateaux of the central part (Fig. 1b); although it has been reported previously by Szabó & Taylor (1994), but in low abundance compared with the northern and southern part. A possible explanation for this phenomenon is that amphibole has been completely reacted out by heating during asthenosphere upwelling, or by the infiltrating metasomatizing melts. In this case, the low abundance of melt pockets in the central part would suggest that amphibole was originally not as common in the central part. These observations, along with the small size of the xenoliths, substantially decrease the chance of finding modal amphibole.

Implications of REE concentrations

Variations in the distribution of REE contents in the studied xenoliths (Fig. 6a–h) show that the upper mantle beneath the NGVF has undergone metasomatic transformation by a basaltic silicate melt to various extents. The character and degree of metasomatism is different for the distinct groups. Groups IA and IIA have REE patterns (Fig. 6a and c) characteristic of depleted MORB mantle observed in 'unmetasomatized' orogenic peridotites (e.g. Bodinier & Godard, 2003). Therefore, they are assumed to represent the original geochemical composition of the mantle beneath the NGVF, which was later overprinted by LREE-enriching metasomatism, the effects of which appear in the xenoliths of Group IB. The variations in representative LREE to HREE (Ce, Sm and Yb in Fig. 15a–c, respectively) as functions of bulk-rock MgO content are associated with the extent of depletion. The correlation is very poor for highly incompatible LREE (i.e. Ce, Fig. 15a), but is stronger for the less incompatible HREE (i.e. Yb, Fig. 15c).

Downloaded from https://academic.oup.com/petrology/article/58/6/1107/4001466 by ETH Zurich user on 30 June 2022

Thus it can be concluded that metasomatic processes mostly affected the LREE, whereas HREE were left generally unchanged, implying that the melt reacting with the wall-rock was LREE-enriched. Several other incompatible elements also are enriched in Group IB clinopyroxenes, such as U and Th, with ranges of 0·01–1·06 ppm and 0·03–3·5 ppm, respectively (Table 3), compared with concentrations in Group IA, which are lower by roughly an order of magnitude (0·005–0·21 ppm and 0·01–0·29 ppm for U and Th, respectively). Group IIA has U–Th contents in a similar range, whereas Group IIB is only slightly more enriched (0·01–0·14 ppm and 0·04–0·50 ppm, respectively). Similar patterns can be observed for Nb and Ta: Group IB has wide concentration ranges and maxima as high as 1·1 ppm Nb and 0·26 ppm Ta, an order of magnitude higher than concentrations in the other groups. This suggests that Group IB xenoliths were affected by a melt rich in U–Th–Nb–Ta–LREE, which had no significant effect on major elements. Enrichment of Nb and Ta is characteristic for amphiboles of intraplate origin, and therefore it was assumed that these elements were present in high concentrations in the amphibole-forming metasomatizing melt. Consequently, the metasomatism of Group IB xenoliths was probably related to this intraplate mafic melt, although extensive amphibole formation occurred only at the Fil'akovo-Kerčik locality in the central part (Fig. 1b; Table 1). In contrast, Group IIB xenoliths have a different geochemical character, specifically the enrichment of several basaltic major elements (Fe, Mn, Ti) as well as LREE, indicating a different metasomatic agent. Xenoliths of this group are also present only in the central part (Fig. 1b), which suggests a metasomatic process different in chemistry and effect, as discussed further below.

Group IB xenoliths are present in almost all NGVF locations (Table 1). This group is variably enriched in LREE, which is attributed to reaction with a small melt fraction (or the late stage of a percolating large melt fraction) leading to more fractionated REE patterns (Van der Wal & Bodinier, 1996). It is assumed that metasomatic processes affected the upper mantle to different degrees, even on a centimeter-scale (Bodinier *et al.*, 1990; O'Reilly & Griffin, 2013). Based on the REE patterns of Group IB clinopyroxenes (Fig. 6b) and the presence of mafic melts in the mantle under the NGVF, such as the host basalt, a mafic melt is assumed to have been the metasomatic agent. However, some Group IB xenoliths have very high LREE/HREE ($La_N/Lu_N > 5$; Table 3) along with low Ti/Eu (Fig. 16), suggesting the effect of carbonatitic melts (Coltorti *et al.*, 1999). A carbonatitic component is further supported by slightly elevated Na contents (Coltorti *et al.*, 1999) in clinopyroxene in some Group IB (and IIB) xenoliths (Fig. 4d), as well as by the presence of CO_2 inclusions in NGVF xenoliths (Konečná, 1990; Szabó & Bodnar, 1996). However, other geochemical features such as the lack of significant depletion in HFSE compared with REE indicate that metasomatism cannot be explained only by carbonatitic melt. High LREE/HREE ratios can be a result of geochemical fractionation of metasomatizing silicate melt percolating through the wall-rock (e.g. Bodinier *et al.*, 1990; Rivalenti *et al.*, 2004), and thus xenoliths with such REE contents can be the products of reaction with a highly evolved melt. Furthermore, as several studies (e.g. Zanetti *et al.*, 1999; Bodinier *et al.*, 2004) have pointed out, fractionation of a hydrous silicate melt during reactive porous flow can result in a carbonatitic residual melt, which leaves carbonatitic imprints in the metasomatized wall-rock. For Group IB xenoliths, it is therefore assumed that the dominant metasomatizing agent was a silicate melt, possibly with a small amount of a carbonatite component, which can account for enrichment of LREE without affecting major elements (Mg, Ca) or modal compositions significantly (Rudnick *et al.*, 1993).

The heterogeneous distribution of metasomatic patterns in the studied xenoliths indicates that melt migration occurred selectively, leaving volumes of the mantle domain partially or completely unaltered (e.g. Wilshire *et al.*, 1980). Such localized melt percolation can be achieved if the lithosphere beneath the NGVF contains a dense network of ductile shear zones that channelize melt percolation and reaction with the peridotite wall-rock (Irving, 1980; Wilshire *et al.*, 1980). Alternatively, dunitic lithologies, which also occur as xenoliths in the NGVF (Szabó & Taylor, 1994; Konečný *et al.*, 1995, 1999; this study), may also act as porous conduits for percolating melts (Kelemen *et al.*, 1997; Liang *et al.*, 2010). It is clear that sampling by the host basalt must have been less selective, as segments depleted in LREE, and thus presumably not affected by this metasomatic event, were also sampled (i.e. Groups IA and IIA).

Formation of Group II xenoliths

Group II xenoliths are characterized by increased Fe contents, and thus have low Mg# (Fig. 4a–c). However, subgroups IIA and IIB differ in both major and trace element distribution (see Figs 4–6 and Table 2). The Fe-rich nature of Group IIA is accompanied by high concentrations of other 'basaltic' elements, such as Al, Na (Fig. 4d), Ca (Fig. 8c) and Ti (Fig. 8b), and they plot on the low-Cr# end of the OSMA field (Fig. 4a). Furthermore, they have relatively high HREE concentrations (Fig. 6c). These attributes suggest that Group IIA xenoliths represent a generally more fertile mantle segment than the other groups, as a result of a lesser extent of partial melting (most of the xenoliths show ~5% melt extraction; Fig. 12c). This fertile mantle is present only beneath the northern part, as all Group IIA xenoliths are from either Podrečany or Jelšovec (Fig. 1b; Table 1).

Group IIB xenoliths, however, show no significant increase in Na, Al or Ca (Figs 4d, 8a and 8c, respectively). Furthermore, they show a continuous increase in both LREE and HREE, and have distribution patterns very

Downloaded from https://academic.oup.com/petrology/article/58/6/1107/4001466 by ETH Zurich user on 30 June 2022

similar to each other (Fig. 6d), which suggests that their REE contents were produced by the same process, alongside Fe–Mn and Ti enrichment. Reactions of peridotite wall-rock with a percolating mafic silicate melt resulting in such geochemical signatures have been observed widely in both orogenic peridotites and mantle xenoliths (e.g. Bodinier *et al.*, 1990; Peslier *et al.*, 2002; Ionov *et al.*, 2005; Raffone *et al.*, 2009; Kourim *et al.*, 2014). It is likely that this metasomatism overprinted the effects of any previous melting or metasomatism. The geochemical characteristics would suggest the host alkali basalt as a possible candidate for the reacting melt (Dobosi *et al.*, 1995). However, the metasomatism is assumed to have happened prior to entrainment and ascent of the xenoliths, for several reasons. First, alkali basalts in the NGVF had a very rapid ascent (Szabó & Bodnar, 1996). Second, geochemical evidence of reaction between the xenoliths and the host basalt has not been found, as major and trace element compositions are homogeneous within single samples (i.e. there is no change from the centre towards the contact with the host basalt). Third, clinopyroxene-rich cumulate xenoliths, which are also present in the NGVF, have been interpreted as having crystallized from basaltic melts percolating through the upper mantle and being trapped near the Moho (Kovács *et al.*, 2004; Zajacz *et al.*, 2007), supporting the presence of basaltic melts in the upper mantle before eruption of the host basalt.

The key to the formation of this group may be a group of wehrlitic xenoliths, found only in the central part of the NGVF (Patkó *et al.*, 2013). These xenoliths show similar geochemical characteristics to Group IIB: low Mg#, moderate Fe–Mn and LREE enrichment in clinopyroxenes and slight Ti enrichment in spinel. The wehrlitic group differs petrographically from the lherzolites as they contain aggregates of secondary olivine, clinopyroxene and spinel, and no modal orthopyroxene. Patkó *et al.* (2013) suggested that these xenoliths are the products of reaction between basaltic melt and wall-rock, which formed clinopyroxene at the expense of orthopyroxene. Such a process, resulting in modal enrichment in a metasomatic phase that was already present in the assemblage, has been termed 'stealth metasomatism' by O'Reilly & Griffin (2013). We propose that Group IIB xenoliths are also associated with this process, although the modal change in pyroxenes was incomplete. The modal ratio of ortho- to clinopyroxene ranges from zero to 3·4 with only three xenoliths at or above 1·5 (Table 1), which suggests that some clinopyroxenes are the product of stealth metasomatism, even though this is not obvious in their petrography. Furthermore, Group IIB xenoliths appear only in the central part (Table 1) together with the wehrlite xenoliths. No wehrlitic signature was found in samples of the northern and southern parts of the NGVF, suggesting that this process was localized in the central part and was independent of the metasomatism that affected Group IB xenoliths.

Reconstruction of geochemical evolution and tectonic implications

Based on the geochemical data presented here, a relative order of geochemical events and a mantle evolution scenario can be proposed in relation to the tectonic situation and history of the NGVF. Metasomatic events overprint the effects of partial melting, interpreted as the earliest traceable event in the history of the upper mantle of the studied area. The oldest metasomatic products in the NGVF xenoliths are inferred to be the Nb-poor amphiboles of Group IA (present in all three sub-areas) and IIA xenoliths (northern part), which show characteristics suggesting a suprasubduction origin (depleted HFSE, especially Nb). However, the origin of the metasomatizing fluid is difficult to determine in the current tectonic environment of the CPR. Geophysical studies (e.g. Szafián & Horváth, 2006; Tašárová *et al.*, 2009) have found that subduction of the European plate under the ALCAPA microplate either was not developed beneath the entire Western Carpathians or was later overprinted by collision tectonics between the two blocks. As Kovács & Szabó (2008) proposed, the most fitting explanation for a subduction environment near the mantle domain of the NGVF is outside the CPR, in the Alpine collision zone, before the extrusion of the ALCAPA microplate and the formation of the Pannonian Basin. This explanation implies that the lithospheric mantle was involved in the extrusion and subsequent movement of the microplate, as suggested by studies of deformed xenoliths from the CPR (Falus, 2004; Hidas *et al.*, 2007). We therefore suggest that the upper mantle of the ALCAPA microplate inherited its geochemical characteristics from a former subduction environment. Subduction-related geochemical imprints (positive anomalies of Ba and Sr, and U-shaped REE patterns) have been reported in xenoliths from other locations of the ALCAPA microplate, such as the Styrian Basin (Coltorti *et al.*, 2007*b*) and the Bakony–Balaton Highland (e.g. Downes *et al.*, 1992; Bali *et al.*, 2007). Although these characteristics have not been found in the xenoliths of this study, volatile-rich melt inclusions reported previously from the NGVF have been interpreted as remnants of a subduction-related silicate melt (Szabó *et al.*, 1996). This, along with the presence of amphibole, suggests that at some point a volatile-bearing melt or fluid affected the upper mantle beneath the whole region (Stage 1 in Fig. 17).

The formation of Nb-poor amphiboles in Group IA and IIA xenoliths was followed by extensive metasomatism causing varying enrichment in U–Th–LREE and local amphibole formation in the mantle beneath the whole area, represented by Group IB xenoliths. Nb–Ta enrichment in these amphiboles and clinopyroxenes suggests that this metasomatic agent was an intraplate basaltic melt (Coltorti *et al.*, 2007*a*). Such basaltic magmas could have been generated by decompression melting during the Miocene extension and asthenosphere upwelling throughout the CPR (Embey-Isztin

Downloaded from https://academic.oup.com/petrology/article/58/6/1107/4001466 by ETH Zurich user on 30 June 2022

et al., 1993), following the juxtaposition of the ALCAPA and Tisza–Dacia blocks (Csontos, 1995). Although the alkali basaltic volcanism followed the period of extension, generation of these melts probably occurred during the extension; part of them did not reach the surface, but interacted with mantle peridotites. As Group IB xenoliths are found in all sub-areas of the NGVF, this metasomatic event had to occur before the oldest eruptions of xenolith-bearing basalts in the northern part (7 Ma; Hurai *et al.*, 2013), but presumably after the onset of the extension (~20–17 Ma; Konecný *et al.*, 2002; Horváth *et al.*, 2006). As discussed above, equilibration REE-based temperatures of the studied xenoliths are considerably higher than those obtained by major element-based methods (Table 1); this discrepancy was interpreted as a record of heating by the asthenospheric upwelling. As this temperature difference is recognized in Group IB xenoliths, which were influenced by U–Th–(Nb–Ta)–LREE metasomatism, this second metasomatism is likely to have occurred before cooling to the closure temperature for diffusion of the major cations used in the two-pyroxene and Ca-in-opx thermometers. These xenoliths are found in all three sub-areas of the NGVF (Stage 2 in Fig. 17), but Nb-rich amphiboles formed during this phase are present in only one locality (Fil'akovo-Kerčik; see Fig. 1b).

The youngest geochemical process is the third metasomatism, probably caused by another basaltic melt of a composition close to that of the host basalts, causing enrichment of Fe–Mn–Ti and LREE observed in Group IIB xenoliths. This event affected the mantle domain of only the central part of the NGVF, and overprinted any previous geochemical characteristics (Stage 3 in Fig. 17). Based on the major and trace element compositions of minerals, this process was probably linked to the formation of the wehrlitic xenolith series.

SUMMARY

Petrographic and geochemical analyses of a large set of lherzolitic xenoliths from the NGVF reveal the imprints of multiple metasomatic events in the lithospheric mantle beneath the area. The xenoliths show a wide range of olivine Mg-numbers (85–91), and were divided into Group I (Mg# $\geq$ 89) and Group II (Mg# $<$ 89). Further division was made based on the LREE depletion ('A' subgroups) or enrichment ('B' subgroups) relative to HREE. Based on the geochemical signatures of these groups, three distinct metasomatic events can be reconstructed in the mantle of the NGVF before the eruption of the host basalts.

Xenoliths of Group IA and IIA, which have clinopyroxene LREE/HREE $<$ 1, are interpreted to represent mantle volumes of different fertility, which were affected by partial melting to various extents (~7–25%), as well as an old metasomatic event resulting in the formation of Nb-poor amphiboles, presumably by a subduction-related, volatile-rich, silicate melt. The second metasomatic process resulted in cryptic metasomatism in Group IB xenoliths, causing U–Th–(Nb–Ta) and LREE enrichment, and the generation of Nb-rich amphiboles. The youngest event prior to host basalt eruption was an enrichment of Fe and Mn in olivine and pyroxenes, LREE in pyroxenes and Ti in spinel, which produced the Group IIB xenoliths. This event was restricted to the central part of the field, and is inferred to be linked to the formation of the wehrlitic xenolith series.

We propose that the second and third metasomatic events represent melt–peridotite wall-rock reactions, with melts of similar origin to that of the alkali basalts hosting the xenoliths. These melts are likely to have been generated during the Miocene extension of the Pannonian Basin. Different ranges in equilibration temperatures, obtained by different thermometers, are considered to record the heating accompanying the Miocene extension and subsequent cooling of the lithospheric mantle beneath the NGVF.

ACKNOWLEDGEMENTS

The authors would like to thank the many people who supported the completion of this work. We are grateful to Anna Maria Fioretti and Raul Carampin for their help with EMPA analyses in Padua, Italy, and also to Orlando Vaselli and Bernardo Cesare for facilitation. David Adams and Will Powell are thanked for helping with geochemical analyses at CCFS, Macquarie University. We acknowledge László Aradi for his help with fieldwork and petrographic consultations. Hilary Downes and Constanza Bonadiman, as well as two anonymous reviewers, are thanked for their constructive comments and thorough structural shaping of the paper. We are also grateful to Executive Editor Marjorie Wilson for her helpful suggestions. This is the 73rd publication of the Lithosphere Fluid Research Lab (LRG), contribution 1004 from the ARC Centre of Excellence for Core to Crust Fluid Systems (www.ccfs.mq.edu.au) and 1176 from the GEMOC Key Centre (www.gemoc.mq.edu.au).

FUNDING

This work was partially supported by the Bolyai Postdoctoral Fellowship Program, a Marie Curie International Reintegration Grant (grant number NAMS-230937) and a postdoctoral grant (grant number PD101683) of the Hungarian Scientific Research Fund (OTKA) to I.J.K., as well as a grant of the Hungarian Scientific Research Fund (grant number 78425) to C.Sz., and a Juan de la Cierva postdoctoral grant (grant number FPDI-2013-16253) to K.H. Further support was received for LA-ICP-MS analyses from Synthesys Project (GB-TAF-3033) to L.P. N.L. received support from Macquarie University international PhD scholarship, project and travel funding from ARC Centre of Excellence for Core to Crust Fluid Systems (CCFS). Instruments used at Macquarie University are funded by DEST Systemic Infrastructure Grants, ARC LIEF, NCRIS/AuScope, industry partners and Macquarie University.

Downloaded from https://academic.oup.com/petrology/article/58/6/1107/4001466 by ETH Zurich user on 30 June 2022

SUPPLEMENTARY DATA

Supplementary data for this paper are available at *Journal of Petrology* online.

REFERENCES

Arai, S. (1987). An estimation of the least depleted spinel peridotite on the basis of olivine-spinel mantle array. *Neues Jahrbuch für Mineralogie* **1987**, 347–354.

Arai, S. (1994). Characterization of spinel peridotites by olivine–spinel compositional relationships: Review and interpretation. *Chemical Geology* **113**, 191–204.

Bali, E., Szabó, C., Vaselli, O. & Török, K. (2002). Significance of silicate melt pockets in upper mantle xenoliths from the Bakony–Balaton Highland Volcanic Field, Western Hungary. *Lithos* **61**, 79–102.

Bali, E., Falus, G., Szabó, C., Peate, D. W., Hidas, K., Török, K. & Ntaflos, T. (2007). Remnants of boninitic melts in the upper mantle beneath the central Pannonian Basin? *Mineralogy and Petrology* **90**, 51–72.

Bali, E., Zanetti, A., Szabó, C., Peate, D. & Waight, T. (2008). A micro-scale investigation of melt production and extraction in the upper mantle based on silicate melt pockets in ultramafic xenoliths from the Bakony–Balaton Highland Volcanic Field (Western Hungary). *Contributions to Mineralogy and Petrology* **155**, 165–179.

Balogh, K., Mihaliková, A. & Vass, D. (1981). Radiometric dating of basalts in southern and central Slovakia. *Zapadne Karpaty, Seria Geologia* **7**, 113–126.

Bedini, R., Bodinier, J.-L., Dautria, J.-M. & Morten, L. (1997). Evolution of LILE-enriched small melt fractions in the lithospheric mantle: a case study from the East African Rift. *Earth and Planetary Science Letters* **153**, 67–83.

Berkesi, M., Guzmics, T., Szabó, C., Dubessy, J., Bodnar, R. J., Hidas, K. & Ratter, K. (2012). The role of CO_2-rich fluids in trace element transport and metasomatism in the lithospheric mantle beneath the Central Pannonian Basin, Hungary, based on fluid inclusions in mantle xenoliths. *Earth and Planetary Science Letters* **331**, 8–20.

Bodinier, J.-L. & Godard, M. (2003). Orogenic, ophiolitic, and abyssal peridotites. In: Turekian, K. K. & Holland, H. D. (eds) *Treatise on Geochemistry*. Elsevier, Amsterdam **2**, 103–170.

Bodinier, J., Dupuy, C. & Dostal, J. (1988). Geochemistry and petrogenesis of Eastern Pyrenean peridotites. *Geochimica et Cosmochimica Acta* **52**, 2893–2907.

Bodinier, J., Vasseur, G., Vernières, J., Dupuy, C. & Fabries, J. (1990). Mechanisms of mantle metasomatism: geochemical evidence from the Lherz orogenic peridotite. *Journal of Petrology* **31**, 597–628.

Bodinier, J.-L., Menzies, M. A., Shimizu, N., Frey, F. A. & McPherson, E. (2004). Silicate, hydrous and carbonate metasomatism at Lherz, France: contemporaneous derivatives of silicate melt–harzburgite reaction. *Journal of Petrology* **45**, 299–320.

Brey, G. P. & Köhler, T. (1990). Geothermobarometry in four-phase lherzolites II. New thermobarometers, and practical assessment of existing thermobarometers. *Journal of Petrology* **31**, 1353–1378.

Cherniak, D. J. & Liang, Y. (2007). Rare earth element diffusion in natural enstatite. *Geochimica et Cosmochimica Acta* **71**, 1324–1340.

Coltorti, M., Bonadiman, C., Hinton, R., Siena, F. & Upton, B. (1999). Carbonatite metasomatism of the oceanic upper mantle: evidence from clinopyroxenes and glasses in ultramafic xenoliths of Grande Comore, Indian Ocean. *Journal of Petrology* **40**, 133–165.

Coltorti, M., Bonadiman, C., Faccini, B., Grégoire, M., O'Reilly, S. Y. & Powell, W. (2007a). Amphiboles from suprasubduction and intraplate lithospheric mantle. *Lithos* **99**, 68–84.

Coltorti, M., Bonadiman, C., Faccini, B., Ntaflos, T. & Siena, F. (2007b). Slab melt and intraplate metasomatism in Kapfenstein mantle xenoliths (Styrian Basin, Austria). *Lithos* **94**, 66–89.

Coogan, L. A., Jenkin, G. R. & Wilson, R. N. (2002). Constraining the cooling rate of the lower oceanic crust: a new approach applied to the Oman ophiolite. *Earth and Planetary Science Letters* **199**, 127–146.

Csontos, L. (1995). Tertiary tectonic evolution of the Intra-Carpathian area. *Acta Vulcanologica* **7**, 1–14.

Dobosi, G., Fodor, R. V. & Goldberg, S. A. (1995). Late-Cenozoic alkali basalt magmatism in Northern Hungary and Slovakia: petrology, source compositions and relationship to tectonics. In: Downes, H. & Vaselli, O. (eds) *Neogene and Related Magmatism in the Carpatho-Pannonian Region. Acta Vulcanologica Special Issue* **7**, 199–207.

Dobosi, G., Jenner, G., Embey-Isztin, A. & Downes, H. (2010). Cryptic metasomatism in clino- and orthopyroxene in the upper mantle beneath the Pannonian region. In: Coltorti, M., Downes, H., Grégoire, M. & O'Reilly, S. Y. (ed.) *Petrological Evolution of the European Lithospheric Mantle. Geological Society, London, Special Publications* **337**, 177–194.

Downes, H. (1997). Shallow continental lithospheric mantle heterogeneity—petrological constraints. In: Fuchs, K. (ed.) *Upper Mantle Heterogeneities from Active and Passive Seismology*. Springer, pp. 295–308.

Downes, H., Embey-Isztin, A. & Thirlwall, M. F. (1992). Petrology and geochemistry of spinel peridotite xenoliths from the western Pannonian Basin (Hungary): evidence for an association between enrichment and texture in the upper mantle. *Contributions to Mineralogy and Petrology* **109**, 340–354.

Embey-Isztin, A. (1978). On the petrology of spinel lherzolite nodules in basaltic rocks from Hungary and Auvergne, France. *Annales Historico-naturales Musei Nationalis Hungarica* **70**, 27–44.

Embey-Isztin, A., Scharbert, H. G., Dietrich, H. & Poultidis, H. (1989). Petrology and geochemistry of peridotite xenoliths in alkali basalts from the Transdanubian Volcanic Region, West Hungary. *Journal of Petrology* **30**, 79–105.

Embey-Isztin, A., Downes, H., James, D. E., Upton, B. G. J., Dobosi, G., Ingram, G. A., Harmon, R. S. & Scharbert, H. G. (1993). The petrogenesis of Pliocene alkaline volcanic rocks from the Pannonian Basin, Eastern Central Europe. *Journal of Petrology* **34**, 317–343.

Embey-Isztin, A., Dobosi, G., Altherr, R. & Meyer, H. P. (2001). Thermal evolution of the lithosphere beneath the western Pannonian Basin: evidence from deep-seated xenoliths. *Tectonophysics* **331**, 285–306.

Embey-Isztin, A., Dobosi, G., Bodinier, J.-L., Bosch, D., Jenner, G., Pourtales, S. & Bruguier, O. (2014). Origin and significance of poikilitic and mosaic peridotite xenoliths in the western Pannonian Basin: geochemical and petrological evidences. *Contributions to Mineralogy and Petrology* **168**, 1–16.

Faccini, B., Bonadiman, C., Coltorti, M., Grégoire, M. & Siena, F. (2013). Oceanic material recycled within the sub-Patagonian lithospheric mantle (Cerro del Fraile, Argentina). *Journal of Petrology* **54**, 1211–1258.

Falus, G. (2004). Microstructural analysis of upper mantle peridotites: their application in understanding mantle processes during the formation of the Intra-Carpathian Basin System. PhD thesis, Eötvös Loránd University, Budapest, 163 pp.

Falus, G., Drury, M. R., van Roermund, H. L. & Szabó, C. (2004). Magmatism-related localized deformation in the mantle: a

Downloaded from https://academic.oup.com/petrology/article/58/6/1107/4001466 by ETH Zurich user on 30 June 2022

case study. *Contributions to Mineralogy and Petrology* **146**, 493–505.

Falus, G., Szabó, C., Kovács, I., Zajacz, Z. & Halter, W. (2007). Symplectite in spinel lherzolite xenoliths from the Little Hungarian Plain, Western Hungary: A key for understanding the complex history of the upper mantle of the Pannonian Basin. *Lithos* **94**, 230–247.

Falus, G., Tommasi, A., Ingrin, J. & Szabó, C. (2008). Deformation and seismic anisotropy of the lithospheric mantle in the southeastern Carpathians inferred from the study of mantle xenoliths. *Earth and Planetary Science Letters* **272**, 50–64.

Falus, G., Tommasi, A. & Soustelle, V. (2011). The effect of dynamic recrystallization on olivine crystal preferred orientations in mantle xenoliths deformed under varied stress conditions. *Journal of Structural Geology* **33**, 1528–1540.

Fitton, J. G. (1995). Coupled molybdenum and niobium depletion in continental basalts. *Earth and Planetary Science Letters* **136**, 715–721.

Foley, S. F., Barth, M. G. & Jenner, G. A. (2000). Rutile/melt partition coefficients for trace elements and an assessment of the influence of rutile on the trace element characteristics of subduction zone magmas. *Geochimica et Cosmochimica Acta* **64**, 933–938.

Frey, F. A. & Green, D. H. (1974). The mineralogy, geochemistry and origin of lherzolite inclusions in Victorian basanites. *Geochimica et Cosmochimica Acta* **38**, 1023–1059.

Frey, F. A. & Prinz, M. (1978). Ultramafic inclusions from San Carlos, Arizona: petrologic and geochemical data bearing on their petrogenesis. *Earth and Planetary Science Letters* **38**, 129–176.

Green, D. (1973). Experimental melting studies on a model upper mantle composition at high pressure under water-saturated and water-undersaturated conditions. *Earth and Planetary Science Letters* **19**, 37–53.

Green, D. H., Hibberson, W. O., Kovács, I. & Rosenthal, A. (2010). Water and its influence on the lithosphere–asthenosphere boundary. *Nature* **467**, 448–451.

Griffin, W., Powell, W., Pearson, N. & O'Reilly, S. (2008). GLITTER: data reduction software for laser ablation ICP-MS. In: Sylvester, P. (ed.) *Laser Ablation-ICP-MS in the Earth Sciences. Mineralogical Association of Canada, Short Course Series* **40**, 204–207.

Guillong, M., Meier, D., Allan, M., Heinrich, C. & Yardley, B. (2008). SILLS: a MATLAB-based program for the reduction of laser ablation ICP-MS data of homogeneous materials and inclusions. In: Sylvester, P. (ed.) *Laser Ablation-ICP-MS in the Earth Sciences. Mineralogical Association of Canada, Short Course Series* **40**, 328–333.

Harangi, S. (2001). Neogene to Quaternary volcanism of the Carpathian–Pannonian Region—A review. *Acta Geologica Hungarica* **44**, 223–258.

Harangi, S. & Lenkey, L. (2007). Genesis of the Neogene to Quaternary volcanism in the Carpathian–Pannonian region: Role of subduction, extension, and mantle plume. In: Beccaluva, L., Bianchini, G. & Wilson, M. (eds) *Cenozoic Volcanism in the Mediterranean Area. Geological Society of America, Special Papers* **418**, 67–92.

Hart, S. R. & Dunn, T. (1993). Experimental cpx/melt partitioning of 24 trace elements. *Contributions to Mineralogy and Petrology* **113**, 1–8.

Hellebrand, E., Snow, J. E., Dick, H. J. & Hofmann, A. W. (2001). Coupled major and trace elements as indicators of the extent of melting in mid-ocean-ridge peridotites. *Nature* **410**, 677–681.

Herzberg, C. (2004). Geodynamic information in peridotite petrology. *Journal of Petrology* **45**, 2507–2530.

Hidas, K., Falus, G., Szabó, C., Szabó, P. J., Kovács, I. & Földes, T. (2007). Geodynamic implications of flattened tabular equigranular textured peridotites from the Bakony–Balaton Highland Volcanic Field (Western Hungary). *Journal of Geodynamics* **43**, 484–503.

Hidas, K., Guzmics, T., Szabó, C., Kovács, I., Bodnar, R. J., Zajacz, Z., Nedli, Z., Vaccari, L. & Perucchi, A. (2010). Coexisting silicate melt inclusions and H_2O-bearing, CO_2-rich fluid inclusions in mantle peridotite xenoliths from the Carpathian–Pannonian region (central Hungary). *Chemical Geology* **274**, 1–18.

Horváth, F. (1993). Towards a mechanical model for the formation of the Pannonian basin. *Tectonophysics* **226**, 333–357.

Horváth, F., Bada, G., Szafián, P., Tari, G., Ádám, A. & Cloetingh, S. (2006). Formation and deformation of the Pannonian Basin: constraints from observational data. In: Gee, D. G. & Stephenson, R. A. (eds) *European Lithosphere Dynamics. Geological Society, London, Memoirs* **32**, 191–206.

Huebner, J. & Turnock, A. (1980). The melting relations at 1 bar of pyroxenes composed largely of Ca-, Mg-, and Fe-bearing components. *American Mineralogist* **65**, 225–271.

Hurai, V., Danišík, M., Huraiová, M., Paquette, J.-L. & Ádám, A. (2013). Combined U/Pb and (U–Th)/He geochronometry of basalt maars in Western Carpathians: implications for age of intraplate volcanism and origin of zircon metasomatism. *Contributions to Mineralogy and Petrology* **166**, 1235–1251.

Ionov, D. A., Bodinier, J.-L., Mukasa, S. B. & Zanetti, A. (2002). Mechanisms and sources of mantle metasomatism: major and trace element compositions of peridotite xenoliths from Spitsbergen in the context of numerical modelling. *Journal of Petrology* **43**, 2219–2259.

Ionov, D. A., Chanefo, I. & Bodinier, J.-L. (2005). Origin of Fe-rich lherzolites and wehrlites from Tok, SE Siberia by reactive melt percolation in refractory mantle peridotites. *Contributions to Mineralogy and Petrology* **150**, 335–353.

Irving, A. J. (1980). Petrology and geochemistry of composite ultramafic xenoliths in alkalic basalts and implications for magmatic processes within the mantle. *American Journal of Science* **280**, 389–426.

Kázmér, M. & Kovács, S. (1985). Permian–Paleogene paleogeography along the eastern part of the Insubric–Periadriatic lineament system: evidence for continental escape of the Bakony–Drauzug Unit. *Acta Geologica Hungarica* **28**, 71–84.

Kelemen, P., Hirth, G., Shimizu, N., Spiegelman, M. & Dick, H. (1997). A review of melt migration processes in the adiabatically upwelling mantle beneath oceanic spreading ridges. *Philosophical Transactions of the Royal Society of London, Series A* **355**, 283–318.

Klébesz, R., Gráczer, Z., Szanyi, G., Liptai, N., Kovács, I., Patkó, L., Pintér, Z., Falus, G., Wesztergom, V. & Szabó, C. (2015). Constraints on the thickness and seismic properties of the lithosphere in an extensional setting (Nógrád–Gömör Volcanic Field, Northern Pannonian Basin). *Acta Geodaetica et Geophysica* **50**, 133–149.

Konečná, M. (1990). Fluidné inklúzie a termodynamické podmienky vzniku xenolitov pinelovych lherzolitov v alkalickych bazaltoch juioého Slovenska. *Mineralia Slovaca* **22**, 555–564.

Konečný, P., Konečný, V., Lexa, J. & Huraiová, M. (1995). Mantle xenoliths in alkali basalts of Southern Slovakia. *Acta Vulcanologica* **7**, 241–248.

Konečný, P., Huraiová, M. & Bielik, M. (1999). *P–T–X–f*O_2 conditions in upper mantle: evidence from lherzolitic xenoliths hosted by Plio-Pleistocene alkali basalts. *Geolines* **9**, 59–66.

Konecný, V., Kovác, M., Lexa, J. & Šefara, J. (2002). Neogene evolution of the Carpatho-Pannonian region: an interplay of

Downloaded from https://academic.oup.com/petrology/article/58/6/1107/4001466 by ETH Zurich user on 30 June 2022

subduction and back-arc diapiric uprise in the mantle. *EGU Stephan Mueller Special Publication Series* **1**, 105–123.

Kourim, F., Bodinier, J.-L., Alard, O., Bendaoud, A., Vauchez, A. & Dautria, J.-M. (2014). Nature and evolution of the lithospheric mantle beneath the Hoggar swell (Algeria): a record from mantle xenoliths. *Journal of Petrology* **55**, 2249–2280.

Kovács, I. & Szabó, C. (2005). Petrology and geochemistry of granulite xenoliths beneath the Nógrád–Gömör Volcanic Field, Carpathian–Pannonian Region (N Hungary/S Slovakia). *Mineralogy and Petrology* **85**, 269–290.

Kovács, I. & Szabó, C. (2008). Middle Miocene volcanism in the vicinity of the Middle Hungarian zone: Evidence for an inherited enriched mantle source. *Journal of Geodynamics* **45**, 1–17.

Kovács, I., Zajacz, Z. & Szabó, C. (2004). Type-II xenoliths and related metasomatism from the Nógrád–Gömör Volcanic Field, Carpathian–Pannonian region (northern Hungary–southern Slovakia). *Tectonophysics* **393**, 139–161.

Kovács, I., Falus, G., Stuart, G., Hidas, K., Szabó, C., Flower, M. J., Hegedűs, E., Posgay, K. & Zilahi-Sebess, L. (2012). Seismic anisotropy and deformation patterns in upper mantle xenoliths from the central Carpathian–Pannonian region: Asthenospheric flow as a driving force for Cenozoic extension and extrusion? *Tectonophysics* **514–517**, 168–179.

Lenkey, L. (1999). *Geothermics of the Pannonian basin and its bearing on the tectonics of basin evolution*. Ph.D. thesis, Vrije Universiteit, 214 pp.

Lenoir, X., Garrido, C., Bodinier, J. & Dautria, J. (2000). Contrasting lithospheric mantle domains beneath the Massif Central (France) revealed by geochemistry of peridotite xenoliths. *Earth and Planetary Science Letters* **181**, 359–375.

Le Roux, V., Bodinier, J.-L., Tommasi, A., Alard, O., Dautria, J.-M., Vauchez, A. & Riches, A. (2007). The Lherz spinel lherzolite: refertilized rather than pristine mantle. *Earth and Planetary Science Letters* **259**, 599–612.

Liang, Y., Schiemenz, A., Hesse, M. A., Parmentier, E. M. & Hesthaven, J. S. (2010). High-porosity channels for melt migration in the mantle: Top is the dunite and bottom is the harzburgite and lherzolite. *Geophysical Research Letters* **37**, doi:10.1029/2010GL044162.

Liang, Y., Sun, C. & Yao, L. (2013). A REE-in-two-pyroxene thermometer for mafic and ultramafic rocks. *Geochimica et Cosmochimica Acta* **102**, 246–260.

Locock, A. J. (2014). An Excel spreadsheet to classify chemical analyses of amphiboles following the IMA 2012 recommendations. *Computers and Geosciences* **62**, 1–11.

Marchesi, C., Garrido, C. J., Proenza, J. A., Hidas, K., Varas-Reus, M. I., Butjosa, L. & Lewis, J. F. (2016). Geochemical record of subduction initiation in the sub-arc mantle: Insights from the Loma Caribe peridotite (Dominican Republic). *Lithos* **252**, 1–15.

McDonough, W. (1991). Partial melting of subducted oceanic crust and isolation of its residual eclogitic lithology. *Philosophical Transactions of the Royal Society of London, Series A* **335**, 407–418.

McDonough, W. F. & Sun, S.-S. (1995). The composition of the Earth. *Chemical Geology* **120**, 223–253.

Mengel, K. & Green, D. (1989). Stability of amphibole and phlogopite in metasomatized peridotite under water-saturated and water-undersaturated conditions. In: Ross, J. (ed.) *Kimberlites and Related Rocks, Geological Society of Australia* **1**, 571–581.

Mercier, J. C. & Nicolas, A. (1975). Textures and fabrics of upper-mantle peridotites as illustrated by xenoliths from basalts. *Journal of Petrology* **16**, 454–487.

Niida, K. & Green, D. (1999). Stability and chemical composition of pargasitic amphibole in MORB pyrolite under upper mantle conditions. *Contributions to Mineralogy and Petrology* **135**, 18–40.

Nimis, P. & Grütter, H. (2010). Internally consistent geothermometers for garnet peridotites and pyroxenites. *Contributions to Mineralogy and Petrology* **159**, 411–427.

Niu, Y. (2004). Bulk-rock major and trace element compositions of abyssal peridotites: implications for mantle melting, melt extraction and post-melting processes beneath mid-ocean ridges. *Journal of Petrology* **45**, 2423–2458.

Niu, Y. & Hékinian, R. (1997). Basaltic liquids and harzburgitic residues in the Garrett Transform: a case study at fast-spreading ridges. *Earth and Planetary Science Letters* **146**, 243–258.

O'Reilly, S. Y. & Griffin, W. (2013). Mantle metasomatism. In: Harlov, D. E. & Austrheim, H. (eds) *Metasomatism and the Chemical Transformation of Rock*. Springer, pp. 471–533.

Patkó, L., Aradi, L. E., Liptai, N., Bodnar, R. J., Fedele, L., Kovács, Z., Cesare, B., Vaselli, O., Fioretti, A. M., Jeffries, T. & Szabó, C. (2013). Wehrlitization processes within the upper mantle beneath the Northern Pannonian Basin (Hungary). *Mineralogical Magazine* **77**, 1934.

Pearce, N. J., Perkins, W. T., Westgate, J. A., Gorton, M. P., Jackson, S. E., Neal, C. R. & Chenery, S. P. (1997). A compilation of new and published major and trace element data for NIST SRM 610 and NIST SRM 612 glass reference materials. *Geostandards Newsletter* **21**, 115–144.

Pécskay, Z., Lexa, J., Szakács, A., Balogh, K., Seghedi, I., Konečny, V., Kovács, M., Márton, E., Kaliciak, M., Széky-Fux, V., Póka, T., Gyarmati, P., Edelstein, O., Rosu, E. & Zec, B. (1995). Space and time distribution of Neogene–Quaternary volcanism in the Carpatho-Pannonian Region. *Acta Vulcanologica* **7**, 15–28.

Pécskay, Z., Lexa, J., Szakács, A., Seghedi, I., Balogh, K., Konečny, V., Zelenka, T., Kovács, M., Póka, T., Fülöp, A., Márton, E., Panaiotu, C., & Cvetković, V. (2006). Geochronology of Neogene magmatism in the Carpathian arc and intra-Carpathian area. *Geologica Carpathica* **57**, 511–530.

Peslier, A. H., Francis, D. & Ludden, J. (2002). The lithospheric mantle beneath continental margins: melting and melt–rock reaction in Canadian Cordillera xenoliths. *Journal of Petrology* **43**, 2013–2047.

Raffone, N., Chazot, G., Pin, C., Vannucci, R. & Zanetti, A. (2009). Metasomatism in the lithospheric mantle beneath Middle Atlas (Morocco) and the origin of Fe- and Mg-rich wehrlites. *Journal of Petrology* **50**, 197–249.

Rivalenti, G., Zanetti, A., Mazzucchelli, M., Vannucci, R. & Cingolani, C. A. (2004). Equivocal carbonatite markers in the mantle xenoliths of the Patagonia backarc: the Gobernador Gregores case (Santa Cruz Province, Argentina). *Contributions to Mineralogy and Petrology* **147**, 647–670.

Rudnick, R. L., McDonough, W. F. & Chappell, B. W. (1993). Carbonatite metasomatism in the northern Tanzanian mantle: petrographic and geochemical characteristics. *Earth and Planetary Science Letters* **114**, 463–475.

Rudnick, R. L., Barth, M., Horn, I. & McDonough, W. F. (2000). Rutile-bearing refractory eclogites: missing link between continents and depleted mantle. *Science* **287**, 278–281.

Schmidt, M., Dardon, A., Chazot, G. & Vannucci, R. (2004). The dependence of Nb and Ta rutile–melt partitioning on melt composition and Nb/Ta fractionation during subduction processes. *Earth and Planetary Science Letters* **226**, 415–432.

Seghedi, I. & Downes, H. (2011). Geochemistry and tectonic development of Cenozoic magmatism in the Carpathian–Pannonian region. *Gondwana Research* **20**, 655–672.

Downloaded from https://academic.oup.com/petrology/article/58/6/1107/4001466 by ETH Zurich user on 30 June 2022

Stegena, L., Géczy, B. & Horváth, F. (1975). Late Cenozoic evolution of the Pannonian basin. *Tectonophysics* **26**, 71–90.

Stosch, H.-G. & Seck, H. (1980). Geochemistry and mineralogy of two spinel peridotite suites from Dreiser Weiher, West Germany. *Geochimica et Cosmochimica Acta* **44**, 457–470.

Streckeisen, A. (1976). To each plutonic rock its proper name. *Earth-Science Reviews* **12**, 1–33.

Sun, S.-S. & McDonough, W. F. (1989). Chemical and isotopic systematics of oceanic basalts: implications for mantle composition and processes. In: Saunders, A. D. & Norry, M. J. (eds) *Magmatism in the Ocean Basins. Geological Society, London, Special Publications* **42**, 313–345.

Szabó, C. & Bodnar, R. (1996). Changing magma ascent rates in the Nógrád–Gömör Volcanic Field, northern Hungary/southern Slovakia: evidence from CO_2-rich fluid inclusions in metasomatized upper mantle xenoliths. *Petrology* **4**, 221–230.

Szabó, C. & Taylor, L. A. (1994). Mantle petrology and geochemistry beneath the Nógrád–Gömör Volcanic Field, Carpathian–Pannonian region. *International Geology Review* **36**, 328–358.

Szabó, C., Harangi, S. & Csontos, L. (1992). Review of Neogene and Quaternary volcanism of the Carpathian–Pannonian region. *Tectonophysics* **208**, 243–256.

Szabó, C., Vaselli, O., Vannucci, R., Bottazzi, P., Ottolini, L., Coradossi, N. & Kubovics, I. (1995). Ultramafic xenoliths from the Little Hungarian Plain (Western Hungary): a petrologic and geochemical study. *Acta Vulcanologica* **7**, 249–264.

Szabó, C., Bodnar, R. J. & Sobolev, A. V. (1996). Metasomatism associated with subduction-related, volatile-rich silicate melt in the upper mantle beneath the Nógrád–Gömör volcanic field, northern Hungary/southern Slovakia; evidence from silicate melt inclusions. *European Journal of Mineralogy* **8**, 881–899.

Szabó, C., Falus, G., Zajacz, Z., Kovács, I. & Bali, E. (2004). Composition and evolution of lithosphere beneath the Carpathian–Pannonian Region: a review. *Tectonophysics* **393**, 119–137.

Szafián, P. & Horváth, F. (2006). Crustal structure in the Carpatho-Pannonian region: insights from three-dimensional gravity modelling and their geodynamic significance. *International Journal of Earth Sciences* **95**, 50–67.

Tašárová, A., Afonso, J.-C., Bielik, M., Götze, J.-M. & Hók, J. (2009). The lithospheric structure of the Western Carpathian–Pannonian Basin region based on the CELEBRATION 2000 seismic experiment and gravity modelling. *Tectonophysics* **475**, 454–469.

Taylor, W. (1998). An experimental test of some geothermometer and geobarometer formulations for upper mantle peridotites with application to the thermobarometry of fertile lherzolite and garnet websterite. *Neues Jahrbuch für Mineralogie, Abhandlungen* **172**, 381–408.

Upton, B. G. J., Downes, H., Kirstein, L. A., Bonadiman, C., Hill, P. G. & Ntaflos, T. (2011). The lithospheric mantle and lower crust–mantle relationships under Scotland: a xenolithic perspective. *Journal of the Geological Society, London* **168**, 873–885.

Van der Wal, D. & Bodinier, J.-L. (1996). Origin of the recrystallisation front in the Ronda peridotite by km-scale pervasive porous melt flow. *Contributions to Mineralogy and Petrology* **122**, 387–405.

Van Orman, J. A., Grove, T. L. & Shimizu, N. (2001). Rare earth element diffusion in diopside: influence of temperature, pressure, and ionic radius, and an elastic model for diffusion in silicates. *Contributions to Mineralogy and Petrology* **141**, 687–703.

VanTongeren, J. A., Kelemen, P. B. & Hanghøj, K. (2008). Cooling rates in the lower crust of the Oman ophiolite: Ca in olivine, revisited. *Earth and Planetary Science Letters* **267**, 69–82.

Vaselli, O., Downes, H., Thirlwall, M., Dobosi, G., Coradossi, N., Seghedi, I., Szakacs, A. & Vannucci, R. (1995). Ultramafic xenoliths in Plio-Pleistocene alkali basalts from the Eastern Transylvanian Basin: Depleted mantle enriched by vein metasomatism. *Journal of Petrology* **36**, 23–53.

Vaselli, O., Downes, H., Thirlwall, M. F., Vannucci, R. & Coradossi, N. (1996). Spinel-peridotite xenoliths from Kapfenstein (Graz Basin, Eastern Austria): a geochemical and petrological study. *Mineralogy and Petrology* **57**, 23–50.

Wallace, M. & Green, D. (1991). The effect of bulk rock composition on the stability of amphibole in the upper mantle: implications for solidus positions and mantle metasomatism. *Mineralogy and Petrology* **44**, 1–19.

Walter, M. (2003). Melt extraction and compositional variability in mantle lithosphere. In: Turekian, K. K., Holland, H. D. (eds) *Treatise on Geochemistry*. Elsevier, Amsterdam **2**, 363–394.

Walter, M. J. (1998). Melting of garnet peridotite and the origin of komatiite and depleted lithosphere. *Journal of Petrology* **39**, 29–60.

Wilshire, H., Pike, J. N., Meyer, C. & Schwarzman, E. (1980). Amphibole-rich veins in lherzolite xenoliths, Dish Hill and Deadman Lake, California. *American Journal of Science, A* **280**, 576–593.

Witt, G. & Seck, H. (1987). Temperature history of sheared mantle xenoliths from the West Eifel, West Germany: evidence for mantle diapirism beneath the Rhenish Massif. *Journal of Petrology* **28**, 475–493.

Zajacz, Z., Kovács, I., Szabó, C., Halter, W. & Pettke, T. (2007). Evolution of mafic alkaline melts crystallized in the uppermost lithospheric mantle: a melt inclusion study of olivine-clinopyroxenite xenoliths, northern Hungary. *Journal of Petrology* **48**, 853–883.

Zanetti, A., Mazzucchelli, M., Rivalenti, G. & Vannucci, R. (1999). The Finero phlogopite-peridotite massif: an example of subduction-related metasomatism. *Contributions to Mineralogy and Petrology* **134**, 107–122.

Downloaded from https://academic.oup.com/petrology/article/58/6/1107/4001466 by ETH Zurich user on 30 June 2022